UNIVERSITÄT PADERBORN
Die Universität der Informationsgesellschaft

Numerical Studies on Coherent Control of Semiconductor Quantum Dots based on k.p-calculations in Envelope Function Approximation

vorgelegt von M.Sc.
Peter Kölling

Fakultät für Naturwissenschaften
Department Physik

Dissertation zur Erlangung des akademischen Doktorgrades Dr. rer. nat.

Promotionskomission:
Vorsitzender: Prof. Dr. Artur Zrenner
Erstgutachter: Prof. Dr. Stefan Schumacher
Zweitgutachter: Prof. Dr. Jens Förstner

Dissertation vorgelegt am:

Contents

List of Figures

Zusammenfassung

Die vorliegende Arbeit befasst sich mit der numerischen Untersuchung der kohärenten Kontrolle von Halbleiter Quantenpunkten. Die Arbeit gliedert sich dabei in zwei Teile. Der erste Teil befasst sich mit der theoretischen Untersuchung verschiedener Quantenpunktsystem im Rahmen der $\boldsymbol{k} \cdot \boldsymbol{p}$ -Theorie. Der Schwerpunkt liegt dabei auf der Abhängigkeit von Dipol- und Coulombmatrixelementen von grundlegenden Parametern wie Form und Materialkomposition der Quantenpunkte. In diesem Abschnitt wird gezeigt, dass Gitterverspannungen, die bei gängigen Herstellungsmethoden unumgänglich sind, einen signifikanten Einfluss auf die betrachteten Systeme haben.

Im zweiten Teil der Arbeit werden zwei Experimente zur kohärenten Kontrolle von Halbleiter Quantenpunkten durch externe elektrische Felder modelliert. Das erste der beiden Experimente demonstriert die kohärente Phasenkontrolle an einem Exziton Zweiniveausystem. Das zweite Experiment befasst sich mit der robusten Populationsinversion, ebenfalls in einem Exziton Zweiniveausystem, durch eine sogenannte schnelle adiabatische Passage. Die Ergebnisse zeigen, dass Phasenkontrolle und kontrollierte Populationsinversion auf Pikosekundenzeitskala möglich sind.

Abstract

The present work covers numerical studies on the coherent control of semiconductor quantum dots. The work is divided into two parts. The first of which covers theoretical studies of different quantum dot systems within $\boldsymbol{k} \cdot \boldsymbol{p}$ theory. Focus of this part lies on investigation of the dependence of dipole and Coulomb matrix elements on system parameters as shape and material composition of the quantum dots. Within this part it is shown that lattice strain, which is unavoidable in common growth techniques, has a significant impact on the treated systems.

The second part of this work covers the theoretical treatment of two experiments aiming at the coherent control of semiconductor quantum dots by means of external electric fields. The first experiment shows coherent phase control on an exciton two level system while the second experiment treats robust population inversion of such a two level systems by so called rapid adiabatic passage. The results show that phase control and robust population inversion are possible at picosecond time scales.

1. Introduction

Semiconductor quantum dots, as treated within this work, are nano-scale islands of semiconductor material embedded in a matrix of host material. Due to their unique properties which render them promising systems for various fields of application, quantum dots have drawn a lot of attention within the last decades. Among possible applications, quantum dots have been discussed as qubits or photon sources for quantum information processing [1, 2, 3, 4, 5, 6], single-photon sources [7, 8, 9, 10, 11, 12], and sources of entangled photon pairs [13, 14, 15, 16, 17, 18]. Over the years of research, sophisticated growth techniques have been developed, which allow a reasonable amount of control over the size of the quantum dots, utilizing self-assembly of the quantum dots under controlled environmental conditions.

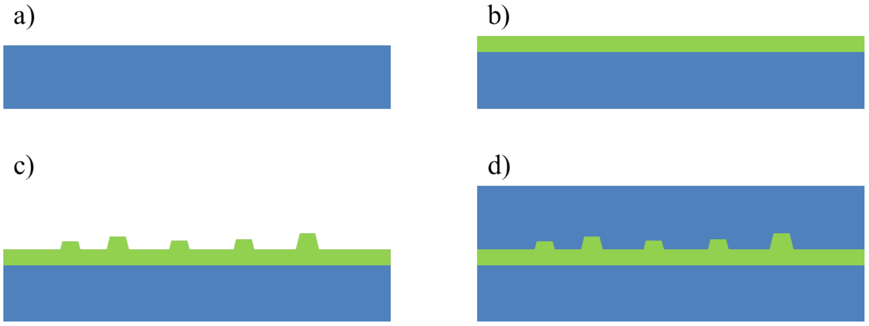

Figure 1.1.: Schematic representation of quantum dot self-assembly by Stranski-Krastanov growth. a) Starting from an unstrained layer of the host material one starts depositing the quantum dot material b). At a critical thickness depending on the lattice mismatch between the dot material and the material of the host matrix, system strain relaxes by spontaneous island formation c). The quantum dots are then usually capped by another layer of the host material d).

Nowadays, self-assembled semiconductor quantum dots are typically grown by molecular beam epitaxy in Stranski-Krastanov growth mode, as depicted in figure 1.1. This technique allows embedding of the quantum dot into electrically active structures such as Schottky diodes. Controlled preparation of high quality samples with tailored properties is an art of its own and a complete description of the topic is outside the scope of this work. However, in order to stress the importance of strain terms in realistic simulations, at least a brief description of the fundamental mechanism of Stranski-Krastanov

growth will be given.
Starting from a reasonable thick layer of the matrix material, such that the top layers of the matrix material may be considered unstrained, one starts layer deposition of the quantum dot material which exhibits a lattice mismatch with respect to the matrix material. Depending on the exact lattice mismatch, at some critical layer thickness the accumulated elastic energy will relax by spontaneous island formation. For the considered InAs quantum dots in a GaAs matrix the critical thickness is ~ 1.7 mono layers of InAs. This process, however, just minimizes the elastic energy, i.e. there is still strain in the system. Depositing more quantum dot material, the islands grow larger laterally and in growth direction which gives a decent degree of control over the quantum confinement. Special control over the height of the resulting quantum dots may be gained using the so-called flush-capping technique. Here, the quantum dots are only partially overgrown. Then the substrate temperature is increased beyond a critical value at which part of the uncovered quantum dot material may desorp from the sample [19, 20]. As a last step, the quantum dots are covered with matrix material. The actual steps taken during the overgrow process may still influence the shape and material composition of the assembled quantum dots and the wetting layer [20, 21].
Considering applications for quantum information processing it is highly desirable to grow single quantum dots or single quantum dot molecules which are composed of two vertically stacked single quantum dots. The growth of low density quantum dot samples by metal-organic chemical vapour deposition has been demonstrated by Hsieh *et al.* [22]. In the same year Chang *et al.* demonstrated an efficient single-photon source based on low-density InGaAs quantum dot samples and photonic-crystal nanocavities [23]. Liang *et al.* demonstrated low-density sample growth by a combination of droplet epitaxy and molecular beam epitaxy [24]. In 2016 low-density samples of quantum dot molecules have been grown by Sharma [25] using a modified gradient approach in molecular beam epitaxy.

1.1. Structure of the thesis

This work divided into three main parts. The first part focuses on determination of the electronic structure of semiconductor heterostructures within $\boldsymbol{k}\cdot\boldsymbol{p}$ theory. In the course of this part, quantum dots of different geometries will be considered and their electronic structures will be compared to each other, working from a rather unphysical model of a spherical quantum dot to a model which has been considered realistic on basis of experimental results by Scheibner *et al.* [26]. On basis of the last model the general influence of strain, presence of the wetting layer and inhomogeneous material compositions inside the quantum dot will be discussed. In addition, as a step towards more complex systems, a quantum dot molecule consisting of two vertically stacked quantum dots will be discussed. After discussion of the general electronic structure of the considered systems, the calculation for various parameters entering into the density matrix formalism on basis of the $\boldsymbol{k} \cdot \boldsymbol{p}$ results will be explained and compared for the considered systems.

The second part of this thesis focuses on the theoretical description of two experiments aiming at coherent control of an exciton TLS by means of external electric fields at picosecond time scales. The first of which is a Ramsey type experiment [27] to demonstrate coherent phase control at time scales shorter than the decoherence time of the exciton TLS. The second experiment deals with rapid adiabatic passage (RAP) aiming at a robust, on demand population inversion of the quantum dot which is highly desirable for both applications and lab research. The theoretical calculations in this part of the thesis have been carried out in close collaboration with Alex Widhalm and Dr. Amlan Mukherjee from the experimental group of Prof. Dr. Artur Zrenner at Paderborn University and parts of the results for the Ramsey type experiment have been published in [28]. A second publication for the RAP experiment is in preparation.

2. Semiconductor Heterostructures

In order to properly describe the dynamics of any quantum system under the influence of external electromagnetic fields, one needs to know the electronic structure, i.e. the eigenstates and the eigenenergies[1] of this system. The theoretical toolbox for calculating the electronic structure of bulk materials is quite versatile. On the *abinitio* side of the spectrum density functional theory and derived methods are sophisticated techniques relying on almost no experimental input. Despite the fact that many of these methods fail to reproduce the exact band gaps observed in experiment, most of them deliver reasonable estimates of the electronic structure of a semiconductor in its ground state. A major strength of such methods is that at least in principle the problem formulation in terms of exchange and correlation potentials is exact. The first approximation is performed inserting parameterized forms of the exchange and correlation potentials often determined from quantum Monte Carlo simulations. However, this is not the point which renders these methods inappropriate for simulation of semiconductor heterostructures.

The major drawback resides in their atomistic nature, i.e. they take into account individual atoms. As the number of atoms grows so does the number of electrons which have to be treated explicitly. Using so-called pseudo-potential methods it is possible to just treat the valence electrons of the atoms replacing the core electrons by an effective potential [29, 30, 31]. Using sufficiently large super cells and periodic boundary conditions, the given methods can still be used to simulate layered structures such as semiconductor quantum wells. When it comes to quantum dots or other 3D structures, however, the number of atoms grows rapidly and so does the computational effort. Although, given enough resources, it would still be possible to solve such a problem, the time required to do so is no longer acceptable.

On the other side of the spectrum of tools on finds fully empirical methods such as plain effective-mass approximation to calculate the electronic structure of bulk materials. The method was developed in the 1930s, when it was realized that the influence of a periodic crystal potential could be modeled by an effective mass tensor [32]. In plain effective-mass approximation one assumes a parabolic dispersion of the individual bands

$$E_{n\boldsymbol{k}} = E_{n\boldsymbol{k}_0} + \frac{\hbar^2 k^2}{2m^*} \tag{2.1}$$

---

[1] Strictly speaking, one does not need to know the exact eigenenergies since only energy differences enter the respective equations of motion.

where $E_{n\boldsymbol{k}_0}$ is the energy extremum of the band, usually evaluated at some high-symmetry point of the Brillouin zone, and m^* is the phenomenological effective mass determining the curvature of the band dispersion. Both parameters have to be fitted on a per-band basis to be able to properly describe bulk semiconductors at least in the vicinity of the high-symmetry points of the Brillouin zone. Further apart from these high-symmetry points, however, many semiconductors exhibit a significantly non-parabolic dispersion which cannot be captured within this simple model. Due to its simplicity this model can be used to simulate mesoscopic and macroscopic systems at least on a qualitative basis given sufficiently accurate parameters of the involved materials. On the other hand, also due to its simplicity, one should not expect this model to quantitatively reproduce experimental data.

A method somewhat in between these two extremes is provided by a theory commonly known as $\boldsymbol{k}\cdot\boldsymbol{p}$ theory which can be thought of as a more elaborate extension of effective-mass theory. To be precise, the term $\boldsymbol{k}\cdot\boldsymbol{p}$ theory nowadays describes a combination of at least two methods. The first of which can be thought of as *pure* $\boldsymbol{k}\cdot\boldsymbol{p}$ theory. This method has proven itself to be quite useful in calculations for bulk semiconductors, but is of limited to no use for heterostructures. The second of which is the $\boldsymbol{k}\cdot\boldsymbol{p}$ theory with additional application of Envelope Function Approximation (EFA).

The electronic structure calculations within this work have been performed using the nextnano++ software package [33] solving an eigenvalue problem arising from $\boldsymbol{k}\cdot\boldsymbol{p}$ equations with applied EFA. The following sections present the basic considerations for the theoretical treatment of semiconductor heterostructures within $\boldsymbol{k}\cdot\boldsymbol{p}$ theory with applied EFA as it is implemented in nextnano.

2.1. General $\boldsymbol{k}\cdot\boldsymbol{p}$ theory

In the following, a brief derivation of the fundamental Hamiltonian matrix from which the widely used 6x6$\boldsymbol{k}\cdot\boldsymbol{p}$ and 8x8$\boldsymbol{k}\cdot\boldsymbol{p}$ Hamiltonians emerge will be given. In doing so, the focus will lie on the central results. More details on the derivation of the Hamiltonian matrices used within the nextnano software package can be found in [34, 35, 36, 37] since these publications are directly related to the development of nextnano. A more step-wise derivation of the 6x6$\boldsymbol{k}\cdot\boldsymbol{p}$ Hamiltonian can be found in [38].

Starting point for the derivation is the stationary relativistic Pauli-Schrödinger equation

$$\left(\frac{\hat{p}^2}{2m} + \frac{1}{4m^2c^2}\left(\boldsymbol{\sigma}\times\nabla V(\boldsymbol{r})\right)\hat{\boldsymbol{p}} + V(\boldsymbol{r}) + \frac{\mu_B g_0}{2}\boldsymbol{\sigma}\cdot\boldsymbol{B}\right)\Psi(\boldsymbol{r}) = E\Psi(\boldsymbol{r}). \tag{2.2}$$

which is, apart from the additional spin-orbit coupling and Zeeman splitting term, identical to the stationary single particle Schrödinger equation. For the moment, the

Zeeman term will be dropped since it only lifts degeneracy of spin degenerate states. The first step of the derivation is the transformation of the given Hamiltonian into the so called Luttinger-Kohn basis [39] which is closely related to the Bloch basis. Given a periodic potential $V(\boldsymbol{r})$, according to the Bloch theorem the fundamental solutions of (2.2) may be written as

$$\Psi_{n\boldsymbol{k}}(\boldsymbol{r}) = u_{n\boldsymbol{k}}(\boldsymbol{r})e^{i\boldsymbol{k}\cdot\boldsymbol{r}} \tag{2.3}$$

where $u_{n\boldsymbol{k}}(\boldsymbol{r})$ are cell-periodic functions with respect to the underlying crystal lattice. These functions build up an orthonormal basis for all values of $\boldsymbol{k}$. Luttinger and Kohn [39] proposed a different basis

$$\chi_{n\boldsymbol{k}}(\boldsymbol{r}) = u_{n\boldsymbol{k}_0}(\boldsymbol{r})e^{i\boldsymbol{k}\cdot\boldsymbol{r}} \tag{2.4}$$

where $\boldsymbol{k}$ is now relative to $\boldsymbol{k}_0$. For this basis it was shown, that it builds up an orthonormal system as well.

As in the case for the conventional Bloch basis the m-th solution $\Psi_m(\boldsymbol{r})$ in (2.2) is expanded with respect to the new basis yielding the the following linear system for the expansion coefficients

$$\sum_{n'} H_{nn'}(\boldsymbol{k})c_{mn'}(\boldsymbol{k}) = E_m(\boldsymbol{k})c_{mn}(\boldsymbol{k}) \tag{2.5}$$

where

$$H_{nn'}(\boldsymbol{k}) = \left(E_{n'}(\boldsymbol{k}_0) + \frac{\hbar^2 k^2}{2m}\right)\delta_{nn'} + \frac{\hbar}{m}\boldsymbol{k}\cdot\boldsymbol{\pi}_{nn'} \tag{2.6}$$

$$\boldsymbol{\pi}_{nn'} = \int_\Omega U_n^*(\boldsymbol{r})\left(\hat{\boldsymbol{p}} + \frac{1}{4m^2c^2}\boldsymbol{\sigma}\times\nabla V(\boldsymbol{r})\right)U_{n'}(\boldsymbol{r})d^3r \tag{2.7}$$

$$U_n(\boldsymbol{r}) = u_{n\boldsymbol{k}_0}(\boldsymbol{r}) \tag{2.8}$$

showing the parabolic band dispersion well known from effective mass theory.

In order to keep the number of bands which have to be treated at a reasonably low number, one somehow has to eliminate the bands in which one is not interested. The procedure to achieve this decoupling is usually referred to as Löwdin perturbation, but differs significantly from the method published by Löwdin [40]. The general procedure is the following

1. divide the bands into two classes A and B, where class B contains only bands which are not of primary interest.

2. divide the Hamiltonian into a part which couples class A and class B bands

3. apply a unitary transformation which eliminates the coupling to first order in $\boldsymbol{k}$, i.e. the resulting transformed Hamiltonian matrix $\bar{H}$ is $\mathcal{O}(k^2)$ correct.

The division into class A and class B states was also part of the method proposed by Löwdin, but instead of the given transformation, Löwdin derived formal expressions for the expansion coefficients by simply reordering the linear system. These expressions, however, contain the yet unknown eigenvalue of the solution and have to be solved iteratively. The decoupling by unitary transformation has been used by Luttinger and Kohn [39] to decouple the top most valence band states from the conduction band states.

Following the derivations in [37], the decomposition of the Hamiltonian matrix using Einstein summation convention is given as

$$
\begin{aligned}
H &= H_0 + H_1 + H_2 && (2.9)\\
H_0 &= \left(E_n(\boldsymbol{k}_0) + \frac{\hbar^2 k^2}{2m}\right)\delta_{nn'} && (2.10)\\
H_1 &= \frac{\hbar}{m} k_i \pi^i_{nn'} \theta_{n,n'} && (2.11)\\
H_2 &= \frac{\hbar}{m} k_i \pi^i_{nn'} (1-\theta_{n,n'}) && (2.12)\\
\theta_{n,n'} &= \begin{cases} 0 & n \text{ and } n' \text{ belong to the same class} \\ 1 & else \end{cases} && (2.13)
\end{aligned}
$$

where $\pi^i_{nn'}$ corresponds to the i-th component of $\boldsymbol{\pi}_{nn'}$. It is easily seen that H_1 describes the coupling among the different classes of bands. Having found a suitable transformation, the Hamiltonian matrix is given by

$$
\begin{aligned}
\bar{H}_{nn'} \approx& H_{0,nn'} + \frac{\hbar}{m} k_i \pi^i_{nn'} \left(1-\theta_{nn'}\right) \\
&+ \frac{1}{2}\sum_m \frac{\hbar^2}{m^2}\left(\frac{k_i \pi^i_{nm}\pi^j_{mn'}k_j}{E_n - E_m} + \frac{k_j \pi^j_{nm}\pi^i_{mn'}k_i}{E_{n'} - E_m}\right)\theta_{nm}\theta_{mn'}
\end{aligned}
\tag{2.14}
$$

Restricting this matrix to the class A bands which are of interest then yields

$$
\begin{aligned}
\bar{H}_{nn'} =& H_{0,nn'} + \frac{\hbar}{m} k_i \pi^i_{nn'} \\
&+ \frac{\hbar^2}{2m^2}\sum_{m\in B} k_i \pi^i_{nm}\left(\frac{1}{E_n - E_m} + \frac{1}{E_{n'} - E_m}\right)\pi^j_{mn'}k_j \quad n, n' \in A
\end{aligned}
\tag{2.15}
$$

A noteworthy point is that the influence of the class B bands is now isolated in the summation term and purely defined in terms of matrix elements of the kinetic momentum operator. These could in principle be determined from abinitio calculations on the respective material system allowing for systematic truncation of the summation. However, the approach commonly used in literature is to first determine which matrix

elements of the momentum operator are allowed by symmetry of the crystal lattice. The remaining summation is then usually collected into a single parameter which is then in turn fitted to experimental data. For example Vurgaftmann *et al.* provide $\boldsymbol{k}\cdot\boldsymbol{p}$ parameter sets for a wide variety of III-V semiconductor compounds [41].
It is usually stressed that, due to boundary conditions at material interfaces, the k vector components do not commute for heterostructures and the exact ordering becomes crucial. In its current form the Hamiltonian matrix is only useful for bulk calculations. In order to find the eigenstates of heterostructures one may apply the EFA, which has been used by Luttinger and Kohn [39] to describe impurity states in bulk semiconductors. First one introduces a position dependent expansion of the desired state into the Luttinger-Kohn basis functions

$$\Psi(\boldsymbol{r}) = \sum_n F_n(\boldsymbol{r})\chi_{n\boldsymbol{k}}(\boldsymbol{r}) \tag{2.16}$$

Inserting this expansion into the underlying Schrödinger equation yields a similar equation for the so-called spinor components $F_n(\boldsymbol{r})$.

$$\sum_{n'} \hat{H}_{nn'}(\boldsymbol{r})F_{n'}(\boldsymbol{r}) = EF_n(\boldsymbol{r}) \tag{2.17}$$

where $\hat{H}_{nn'}(\boldsymbol{r})$ corresponds to the, now position dependent, $\boldsymbol{k}\cdot\boldsymbol{p}$ Hamiltonian with any occurrence of $\boldsymbol{k}$ replaced by its real space representation, i.e. $\boldsymbol{k} \to -i\nabla$. In case of an additional external potential one would add the term $V_{ext}(\boldsymbol{r})\delta_{nn'}$ to the matrix operator. In principle, this approach introduces a new problem. When dealing with heterostructures, one is faced with abrupt changes of the basis functions used for the expansions since the Luttinger-Kohn basis is constructed from a local bulk Hamiltonian. This problem has already been addressed in literature, and e.g. Burt [42] has justified the application of EFA to heterostructures.

Summarizing this section one finds

- for bulk semiconductors, the decoupled Hamiltonian for the class A bands of interest is given by (2.15)
- the influence of class B bands is parameterized in terms of the matrix elements of the kinetic momentum operator
- Exploiting symmetries, the influence of the class B bands can be captured by a few parameters determined by direct calculation from atomistic models or by fitting experimental data
- heterostructures can be treated using the same Hamiltonian as in the bulk case, just replacing $\boldsymbol{k}$ by its real space representation.

2.2. Multi-band $\boldsymbol{k}\cdot\boldsymbol{p}$ in nextnano

According to the documentation the Hamiltonian matrix, as implemented in nextnano++, is divided as follows

$$\hat{H}_{nn'} = \hat{H}_{nn',0} + H_{nn',S} + \hat{H}_{nn',SO} + \hat{H}_{nn',ZS} \tag{2.18}$$

with $\hat{H}_{nn',0}$ as the bulk $\boldsymbol{k}\cdot\boldsymbol{p}$ Hamiltonian matrix without spin-orbit coupling or strain effects, the strain Hamiltonian $\hat{H}_{nn',S}$, the spin-orbit coupling Hamiltonian $\hat{H}_{nn',SO}$, and the Zeeman splitting Hamiltonian $\hat{H}_{nn',ZS}$. The bulk 8x8 $\boldsymbol{k}\cdot\boldsymbol{p}$ Hamiltonian in momentum space without spin-orbit coupling is given by [36][2]

$$\hat{H}_0 = \begin{pmatrix} H_{cc} & 0 & H_{cv}^{sx} & H_{cv}^{sy} & H_{cv}^{sz} & 0 & 0 & 0 \\ 0 & H_{cc} & 0 & 0 & 0 & H_{cv}^{sx} & H_{cv}^{sy} & H_{cv}^{sx} \\ H_{cv}^{xs} & 0 & H_{vv}^{xx} & H_{vv}^{xy} & H_{vv}^{xz} & 0 & 0 & 0 \\ H_{cv}^{ys} & 0 & H_{vv}^{yx} & H_{vv}^{yy} & H_{vv}^{yz} & 0 & 0 & 0 \\ H_{cv}^{zs} & 0 & H_{vv}^{zx} & H_{vv}^{zy} & H_{vv}^{zz} & 0 & 0 & 0 \\ 0 & H_{cv}^{xs} & 0 & 0 & 0 & H_{vv}^{xx} & H_{vv}^{xy} & H_{vv}^{xz} \\ 0 & H_{cv}^{ys} & 0 & 0 & 0 & H_{vv}^{yx} & H_{vv}^{yy} & H_{vv}^{yz} \\ 0 & H_{cv}^{zs} & 0 & 0 & 0 & H_{vv}^{zx} & H_{vv}^{zy} & H_{vv}^{zz} \end{pmatrix} \tag{2.19}$$

where the individual rows/columns correspond to the $|S+\rangle$, $|S-\rangle$, $|X+\rangle$, $|Y+\rangle$, $|Z+\rangle$, $|X-\rangle$, $|Y-\rangle$, and $|Z-\rangle$-spinors respectively. The exact expressions for the $H_{vv}^{\nu\mu}$ and $H_{cv}^{\nu\mu}$ depend on the crystal structure of the system of interest. For zinc-blende crystals one finds

$$H_{cc} = E_c + \frac{\hbar^2}{2m_0} S\mathbf{k}^2 \tag{2.20}$$

$$H_{cv}^{sx} = k_y B k_z + iPk_x \tag{2.21}$$

$$H_{cv}^{sy} = k_z B k_x + iPk_y \tag{2.22}$$

$$H_{cv}^{sz} = k_x B k_y + iPk_z \tag{2.23}$$

$$H_{cv}^{xs} = k_z B k_y - ik_x P \tag{2.24}$$

$$H_{cv}^{ys} = k_x B k_z - ik_y P \tag{2.25}$$

$$H_{cv}^{zs} = k_y B k_x - ik_z P \tag{2.26}$$

---

[2] In [36] it is pointed out that the particular ordering of the matrix elements allows efficient implementation of 6x6 $\boldsymbol{k}\cdot\boldsymbol{p}$ and 8x8 $\boldsymbol{k}\cdot\boldsymbol{p}$ calculations at once. For 6x6 $\boldsymbol{k}\cdot\boldsymbol{p}$ calculations one only has to drop the first two rows and columns of the given Hamiltonian and adjust some model parameters.

as well as

$$H_{vv}^{xx} = E_{v,av} + \frac{\hbar^2}{2m_0} + k_x L' k_x + k_y M' k_y + k_z M' k_z \tag{2.27}$$

$$H_{vv}^{xy} = k_x N^{+\prime} k_y + k_y N^{-\prime} k_x \tag{2.28}$$

$$H_{vv}^{xz} = k_x N^{+\prime} k_z + k_z N^{-\prime} k_x \tag{2.29}$$

$$H_{vv}^{yx} = k_y N^{+\prime} k_x + k_x N^{-\prime} k_y \tag{2.30}$$

$$H_{vv}^{yy} = E_{v,av} + \frac{\hbar^2}{2m_0} + k_x M' k_x + k_y L' k_y + k_z M' k_z \tag{2.31}$$

$$H_{vv}^{yz} = k_y N^{+\prime} k_z + k_z N^{-\prime} k_y \tag{2.32}$$

$$H_{vv}^{zx} = k_z N^{+\prime} k_x + k_x N^{-\prime} k_z \tag{2.33}$$

$$H_{vv}^{zy} = k_z N^{+\prime} k_y + k_y N^{-\prime} k_z \tag{2.34}$$

$$H_{vv}^{zz} = E_{v,av} + \frac{\hbar^2}{2m_0} + k_x M' k_x + k_y M' k_y + k_z L' k_z. \tag{2.35}$$

Where $E_{v,av}$ is the average of the three conduction band edges. The $N^{+\prime}$,$N^{-\prime}$,L', and M' are the so called modified Dresselhaus-Kip-Kittel (DKK) parameters. The original parameters N^{+},N^{-},L, and M have been defined for 6x6 $\boldsymbol{k}\cdot\boldsymbol{p}$ calculations where the first conduction bands are treated in a perturbative manner [43]. Compared to the original parameter set the modified DKK-parameters contain correction terms which take into account that the first conduction bands are treated explicitly. According to [36] one finds

$$L' = L + \frac{\hbar^2}{2m_0}\frac{E_P}{E_g} = L + \frac{P^2}{E_g} \tag{2.36}$$

$$M' = M' \tag{2.37}$$

$$N^{+\prime} = N^{+} + \frac{P^2}{E_g} \tag{2.38}$$

$$N^{-\prime} = N^{-} \tag{2.39}$$

$$N' = N + \frac{P^2}{E_g} \tag{2.40}$$

with the band gap E_g and E_P defined in terms of Kane's momentum element P [44] as $E_P = 2mP^2/\hbar^2$. The spin-orbit coupling Hamiltonian is given by

$$\hat{H}_{SO} = \frac{\Delta_{SO}}{3}\begin{pmatrix} 0 & 0 & 0 & 0 & 0 & 0 & 0 & 0 \\ 0 & 0 & 0 & 0 & 0 & 0 & 0 & 0 \\ 0 & 0 & 0 & -i & 0 & 0 & 0 & 1 \\ 0 & 0 & i & 0 & 0 & 0 & 0 & -i \\ 0 & 0 & 0 & 0 & 0 & -1 & i & 0 \\ 0 & 0 & 0 & 0 & -1 & 0 & i & 0 \\ 0 & 0 & 0 & 0 & -i & -i & 0 & 0 \\ 0 & 0 & 1 & i & 0 & 0 & 0 & 0 \end{pmatrix} \tag{2.41}$$

with the spin-orbit coupling parameter defined as

$$\Delta_{SO} = \frac{-3i\hbar^2}{4m^2c^2}\left\langle X\middle|(\nabla V \times \boldsymbol{p}))_y\middle|Z\right\rangle \tag{2.42}$$

It is easily seen that this part of the Hamiltonian acts only on the valence band states. In the bulk case it provides the splitting between the spin split off band and the heavy and light hole bands.

2.3. Modeling strained structures

Considering semiconductors with a zinc blende crystal structure strain affects a given system in two ways. First of all, if a crystal is put under strain, the periodicity of the lattice is changed. The changed periodicity will result in renormalization of the band edges and in consequence in a renormalization of the band gap. Van de Walle addressed this in his model-solid theory for a plane interface between different semiconductor materials [45].

As can be seen in figure 2.1, the band offsets at a semiconductor heterojunction are significantly changed if strain is taken into account. This is especially important when dealing with quantum wells or quantum dots. The second effect is generation of piezo electric charge densities due to displacement of the center of masses for positive and negative charge carriers within a unit cell. These charge densities induce an additional electrostatic potential on top of the periodic potential provided by the bare crystal atoms. In turn this will result in modified profiles for the band edges. The presence of this effect, however, depends on the growth conditions. Figure 2.2 compares the calculated band profiles for two different GaAs-InAs heterojunctions, each calculated both considering and neglecting piezo-electric charge densities. It is easily seen, that in case of a simple planar interface only the heterojunction grown onto the (111) plane is affected by piezo-electric charges.

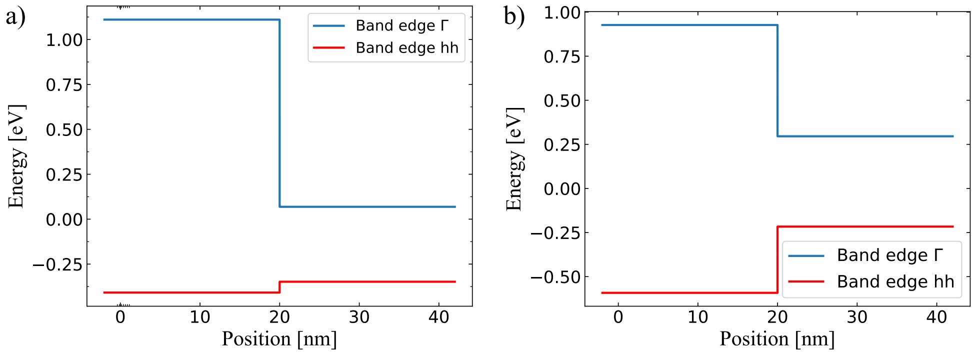

Figure 2.1.: Calculated band edges across the interface between two half-spaces with different semiconductor materials. a) $\boldsymbol{k} \cdot \boldsymbol{p}$ calculations without strain. b) $\boldsymbol{k} \cdot \boldsymbol{p}$ calculations including strain.

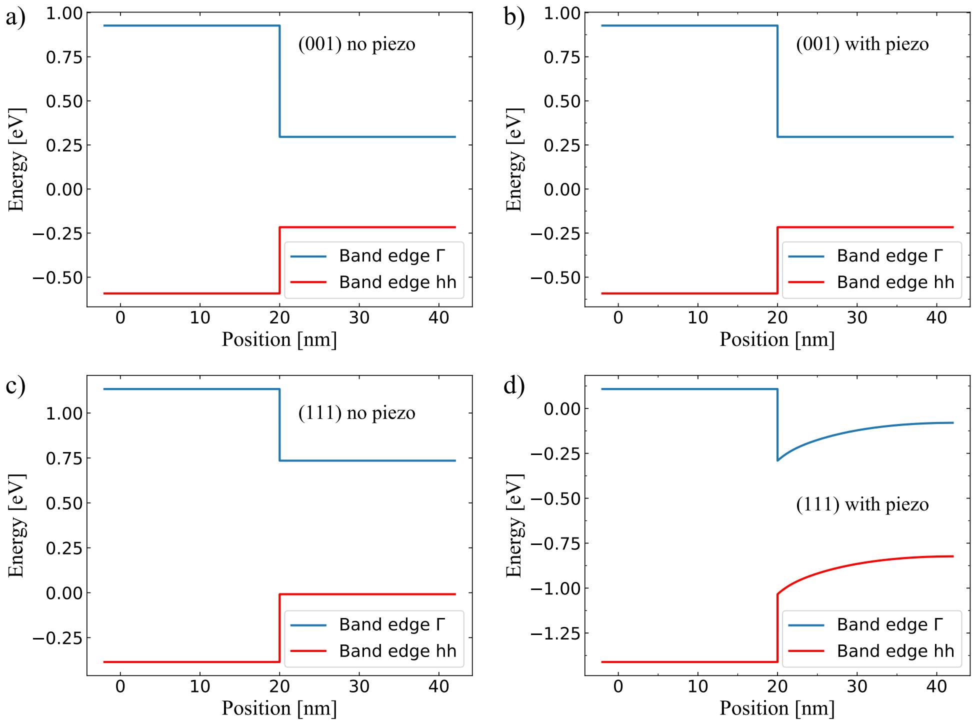

Figure 2.2.: Calculated bandedges for a,b) a GaAs-InAs heterojunction grown onto the (001) plane of GaAs a) neglecting and b) considering piezoelectric charge densities. c,d) the same calculations as for a) and b), but for a heterojunction grown onto the (111) plane of GaAs. The band profile for the heterojunction on the (001) plane remains unaffected while the band profile for the heterojunction on the (111) plane is significantly changed.

Within nextnano++ strain is considered on basis of a continuum model. By minimizing the free elastic energy of the system [37]

$$F[\boldsymbol{\epsilon}] = \frac{1}{2} \sum_{i,j} \int_V \epsilon_i(\boldsymbol{r}) C_{ij} \epsilon_j(\boldsymbol{r}) d^3 r \tag{2.43}$$

where C_{ij} is the elastic tensor and

$$\boldsymbol{\epsilon} = \begin{pmatrix} \epsilon_{xx} \\ \epsilon_{yy} \\ \epsilon_{zz} \\ 2\epsilon_{yz} \\ 2\epsilon_{zx} \\ 2\epsilon_{xy} \end{pmatrix} = \begin{pmatrix} \frac{\partial}{\partial x} u_x(\boldsymbol{r}) \\ \frac{\partial}{\partial y} u_y(\boldsymbol{r}) \\ \frac{\partial}{\partial z} u_z(\boldsymbol{r}) \\ \frac{\partial}{\partial y} u_z(\boldsymbol{r}) + \frac{\partial}{\partial z} u_y(\boldsymbol{r}) \\ \frac{\partial}{\partial z} u_x(\boldsymbol{r}) + \frac{\partial}{\partial x} u_z(\boldsymbol{r}) \\ \frac{\partial}{\partial x} u_y(\boldsymbol{r}) + \frac{\partial}{\partial y} u_x(\boldsymbol{r}) \end{pmatrix} \tag{2.44}$$

with the position dependent displacement vector $\boldsymbol{u}(\boldsymbol{r}) = (u_x(\boldsymbol{r}), u_y(\boldsymbol{r}), u_z(\boldsymbol{r}))^T$. Once the strain components have been determined from the functional derivative

$$\frac{\delta F[\boldsymbol{\epsilon}]}{\delta u_i} = 0 \qquad \forall i \in \{x, y, z\} \tag{2.45}$$

the piezoelectric polarization in zinc blende structures is calculated from

$$\boldsymbol{P}_{piezo}(\boldsymbol{r}) = \begin{pmatrix} 0 & 0 & 0 & e_{14}(\boldsymbol{r}) & 0 & 0 \\ 0 & 0 & 0 & 0 & e_{14}(\boldsymbol{r}) & 0 \\ 0 & 0 & 0 & 0 & 0 & e_{14}(\boldsymbol{r}) \end{pmatrix} \boldsymbol{\epsilon}(\boldsymbol{r}). \tag{2.46}$$

Here e_{14} is the piezo electric material constant. The polarization charges may then be calculated from

$$\rho_{piezo}(\boldsymbol{r}) = -\nabla \cdot \boldsymbol{P}_{piezo}(\boldsymbol{r}) \tag{2.47}$$

if they are desired. If only the additional potential is needed, one can directly solve

$$-\nabla \varepsilon_0 \varepsilon_r(\boldsymbol{r}) \nabla \Phi_{piezo}(\boldsymbol{r}) = -\nabla \cdot \boldsymbol{P}_{piezo}(\boldsymbol{r}) \tag{2.48}$$

To this end, the part of the Hamiltonian matrix describing piezo electric charges can be stated as

$$H_{nn',S} = q \Phi_{piezo}(\boldsymbol{r}) \delta_{nn'}. \tag{2.49}$$

A thorough derivation of a eight-band $\boldsymbol{k} \cdot \boldsymbol{p}$ Hamiltonian for strained zinc-blende crystals can be found in [46].

2.4. Determination of optical matrix elements

Given a set of orthonormal eigenfunctions of a given system the matrix elements describing optical transitions between these states can be determined in several ways. A very simple definition of the dipole matrix element in real space is given as

$$\langle \boldsymbol{\mu} \rangle_{ij} = e \langle \varphi_i | \boldsymbol{r} | \varphi_j \rangle . \tag{2.50}$$

When dealing with atomic eigenstates of a single atom located at the origin of the coordinate system, this definition might give reasonably good results. When it comes to semiconductor heterostructures, however, this approach has an obvious flaw, namely the result of (2.50) strongly depends on the choice of the coordinate system.
A more suitable approach is using the more fundamental relation between the dipole operator $\hat{\boldsymbol{\mu}}$ and the momentum operator $\hat{\boldsymbol{p}}$ [47, 48]

$$\langle \hat{\boldsymbol{\mu}} \rangle_{ij} = \frac{ie\hbar}{m_0 \left(\varepsilon_i - \varepsilon_j \right)} \langle \varphi_i | \hat{\boldsymbol{p}} | \varphi_j \rangle \tag{2.51}$$

Inserting the $\boldsymbol{k} \cdot \boldsymbol{p}$ expansion of the eigenstates yields

$$\langle \hat{\boldsymbol{\mu}} \rangle_{ij} = \frac{ie\hbar}{m_0 \left(\varepsilon_i - \varepsilon_j \right)} \sum_{lm} \int_\Omega u_{i,l} * (\boldsymbol{r}) F^*_{i,l}(\boldsymbol{r}) \hat{\boldsymbol{p}} u_{j,m}(\boldsymbol{r}) F_{j,m}(\boldsymbol{r}) d^3 r. \tag{2.52}$$

Keeping in mind that, apart from a constant prefactor, the real space representation of the momentum operator is given by the gradient and utilizing the fact that the envelope functions are assumed to be slowly varying over rather mesoscopic length scales, equation (2.52) may be rewritten as

$$\begin{aligned} \langle \hat{\boldsymbol{\mu}} \rangle_{ij} = \frac{ie\hbar}{m_0 \left(\varepsilon_i - \varepsilon_j \right)} \sum_{lm} \Bigg(& \langle u_{i,l} | \hat{\boldsymbol{p}} | u_{j,m} \rangle \int_\Omega F^*_{i,l}(\boldsymbol{r}) F_{j,m}(\boldsymbol{r}) d^3 r \\ & + \delta_{lm} \int_\Omega F^*_{i,l}(\boldsymbol{r}) \hat{\boldsymbol{p}} F_{j,m}(\boldsymbol{r}) d^3 r \Bigg) \end{aligned} \tag{2.53}$$

where the first term may be identified as the inter-band part and the second term as the intra-band part of the optical matrix element. Considering piece wise homogeneous material distributions, the given equation should give reasonable results. When inhomogeneous material distributions such as linearly increasing Indium content are considered, the above equation fails to give reasonable results since the prefactor of the integral in inter-band part is no longer constant. To this end the expectation value of the momentum operator is calculated in a different way within this work.

Within the validity range of $\boldsymbol{k}\cdot\boldsymbol{p}$ theory the expectation value of the momentum matrix may be approximated by a generalized version of the Hellman-Feynman theorem [49]

$$\boldsymbol{p}^{\alpha}_{\nu\nu'} \approx \frac{\partial H_{\nu\nu'}}{\partial k_\alpha} \tag{2.54}$$

Considering that the spin-orbit terms as well as the strain terms in the 8x8$\boldsymbol{k}\cdot\boldsymbol{p}$ Hamiltonian do no depend on k, it is sufficient to insert the Hamiltonian (2.19) into (2.54) to calculate the expectation value of the momentum operator. Since the momentum operator does not act on the spin variable, it is sufficient to calculate the single group representation of the momentum matrix elements. Considering a slight reordering of the basis functions one may write the momentum matrix elements with respect to the full 8x8 $\boldsymbol{k}\cdot\boldsymbol{p}$ basis set as follows

$$\frac{\hbar}{m_0}\mathbf{p}^{8\times8}_{\nu} = \left(\begin{array}{cc} \frac{\hbar}{m_0}\mathbf{p}^{4\times4}_{\nu} & \mathbf{0}^{4\times4} \\ & \\ \mathbf{0}^{4\times4} & \frac{\hbar}{m_0}\mathbf{p}^{4\times4}_{\nu} \end{array}\right) \tag{2.55}$$

where the first four rows/columns correspond to $|S+\rangle$, $|X+\rangle$, $|Y+\rangle$, and $|Z+\rangle$ and the last four rows/columns to the spinors with negative spin respectively. Considering the original ordering of the basis set as used for 2.19 the momentum matrix element reads

$$\frac{\hbar}{m_0}\boldsymbol{p}^{8\times8}_{\nu} = \frac{\hbar}{m_0}\begin{pmatrix} p^{ss}_\nu & 0 & p^{sx}_\nu & p^{sy}_\nu & p^{sz}_\nu & 0 & 0 & 0 \\ 0 & p_\nu & 0 & 0 & 0 & p^{sx}_\nu & p^{sy}_\nu & p^{sz}_\nu \\ p^{xs}_\nu & 0 & p^{xx}_\nu & p^{xy}_\nu & p^{xz}_\nu & 0 & 0 & 0 \\ p^{ys}_\nu & 0 & p^{yx}_\nu & p^{yy}_\nu & p^{yz}_\nu & 0 & 0 & 0 \\ p^{zs}_\nu & 0 & p^{zx}_\nu & p^{zy}_\nu & p^{zz}_\nu & 0 & 0 & 0 \\ 0 & p^{xs}_\nu & 0 & 0 & 0 & p^{xx}_\nu & p^{xy}_\nu & p^{xz}_\nu \\ 0 & p^{ys}_\nu & 0 & 0 & 0 & p^{yx}_\nu & p^{yy}_\nu & p^{yz}_\nu \\ 0 & p^{zs}_\nu & 0 & 0 & 0 & p^{zx}_\nu & p^{zy}_\nu & p^{zz}_\nu \end{pmatrix} \tag{2.56}$$

In the bulk case (2.56) can be directly used for calculation of the momentum matrix elements. Considering heterostructures one has to replace k_ν by it's real-space representation $-i\nabla_\nu$ for the structured directions [49].

Applying the Hellman-Feynman theorem to the Hamiltonian (2.19) yields the following equations for the momentum matrix elements.

$$\frac{\hbar}{m_0}\mathbf{p}_x^{4\times 4} \approx \begin{pmatrix} \frac{\hbar^2}{2m_0}\left(Sk_x + k_xS\right) & iP & k_zB & Bk_y \\ -iP & \frac{\hbar^2}{m_0}k_x + L'k_x + k_xL' & N^{+\prime}k_y + k_yN^{-\prime} & N^{+\prime}k_z + k_zN^{-\prime} \\ Bk_z & k_yN^{+\prime} + N^{-\prime}k_y & \frac{\hbar^2}{m_0}k_x + M'k_x + k_xM' & 0 \\ k_yB & k_zN^{+\prime} + N^{-\prime}k_z & 0 & \frac{\hbar^2}{m_0}k_x + M'k_x + k_xM' \end{pmatrix} \tag{2.57}$$

$$\frac{\hbar}{m_0}\mathbf{p}_y^{4\times 4} \approx \begin{pmatrix} \frac{\hbar^2}{2m_0}\left(Sk_y + k_yS\right) & Bk_z & iP & k_xB \\ k_zB & \frac{\hbar^2}{m_0}k_y + M'k_y + k_yM' & k_xN^{+\prime} + N^{-\prime}k_x & 0 \\ -iP & N^{+\prime}k_x + k_xN^{-\prime} & \frac{\hbar^2}{m_0}k_y + L'k_y + k_yL' & N^{+\prime}k_z + k_zN^{-\prime} \\ Bk_x & 0 & N^{+\prime}k_y + k_yN^{-\prime} & \frac{\hbar^2}{m_0}k_y + M'k_y + k_yM' \end{pmatrix} \tag{2.58}$$

$$\frac{\hbar}{m_0}\mathbf{p}_z^{4\times 4} \approx \begin{pmatrix} \frac{\hbar^2}{2m_0}\left(Sk_z + k_zS\right) & k_yB & Bk_x & iP \\ Bk_y & \frac{\hbar^2}{m_0}k_z + M'k_z + k_zM' & 0 & k_xN^{+\prime} + N^{-\prime}k_x \\ k_xB & 0 & \frac{\hbar^2}{m_0}k_z + M'k_z + k_zM' & k_yN^{+\prime} + N^{-\prime}k_y \\ -iP & N^{+\prime}k_x + k_xN^{-\prime} & N^{+\prime}k_y + k_yN^{-\prime} & \frac{\hbar^2}{m_0}k_z + L'k_z + k_zL' \end{pmatrix} \tag{2.59}$$

For the case of a bulk semiconductor at the Γ-point (2.57)-(2.59) reduce to

$$\frac{\hbar}{m_0}\boldsymbol{p}_x^{4\times4} \approx \begin{pmatrix} 0 & iP & 0 & 0 \\ -iP & 0 & 0 & 0 \\ 0 & 0 & 0 & 0 \\ 0 & 0 & 0 & 0 \end{pmatrix} \tag{2.60}$$

$$\frac{\hbar}{m_0}\boldsymbol{p}_y^{4\times4} \approx \begin{pmatrix} 0 & 0 & iP & 0 \\ 0 & 0 & 0 & 0 \\ -iP & 0 & 0 & 0 \\ 0 & 0 & 0 & 0 \end{pmatrix} \tag{2.61}$$

$$\frac{\hbar}{m_0}\boldsymbol{p}_z^{4\times4} \approx \begin{pmatrix} 0 & 0 & 0 & iP \\ 0 & 0 & 0 & 0 \\ 0 & 0 & 0 & 0 \\ -iP & 0 & 0 & 0 \end{pmatrix} \tag{2.62}$$

If one is interested in the optical matrix elements for a given polarization of the exciting light field one has to use proper linear combination of these. Considering for example the optical matrix elements for left-circularly polarized light one has to calculate $\boldsymbol{\epsilon}_{\sigma+} \cdot \boldsymbol{p}$ where $\boldsymbol{\epsilon}_{\sigma+} = \frac{1}{\sqrt{2}}\left(\vec{e}_x + i\vec{e}_y\right)$.
Inserting (2.60) and (2.61) one finds

$$\boldsymbol{\epsilon}_{\sigma+} \cdot \boldsymbol{p} = \frac{m_0}{\hbar} \begin{pmatrix} 0 & iP & -P & 0 \\ -iP & 0 & 0 & 0 \\ P & 0 & 0 & 0 \\ 0 & 0 & 0 & 0 \end{pmatrix}. \tag{2.63}$$

The bulk eigenstates are the eigenstates of the total angular momentum operator, namely:

$$\left|S, \frac{1}{2}\right\rangle_c = |S+\rangle \tag{2.64}$$

$$\left|S, -\frac{1}{2}\right\rangle_c = |S-\rangle \tag{2.65}$$

$$\left|\frac{3}{2}, \frac{3}{2}\right\rangle_v = -\frac{1}{\sqrt{2}}\left(|X+\rangle + i\,|Y+\rangle\right) \tag{2.66}$$

$$\left|\frac{3}{2}, \frac{1}{2}\right\rangle_v = -\frac{1}{\sqrt{6}}\left(|X-\rangle + i\,|Y-\rangle\right) + \sqrt{\frac{2}{3}}\,|Z+\rangle \tag{2.67}$$

$$\left|\frac{3}{2}, -\frac{1}{2}\right\rangle_v = \frac{1}{\sqrt{6}}\left(|X+\rangle + i\,|Y+\rangle\right) + \sqrt{\frac{2}{3}}\,|Z-\rangle \tag{2.68}$$

$$\left|\frac{1}{2},\frac{1}{2}\right\rangle_v = \frac{1}{\sqrt{3}}\left(|X-\rangle + i\,|Y-\rangle\right) + \frac{1}{\sqrt{3}}\,|Z+\rangle \tag{2.69}$$

$$\left|\frac{1}{2},-\frac{1}{2}\right\rangle_v = \frac{1}{\sqrt{3}}\left(|X+\rangle + i\,|Y+\rangle\right) - \frac{1}{\sqrt{3}}\,|Z-\rangle \tag{2.70}$$

As has been shown by Eissfeller [49] the optical dipole selection rules for circularly polarized light hold

Transition	$\boldsymbol{\sigma+}$	$\boldsymbol{\sigma-}$
$\left\|\frac{3}{2},\frac{3}{2}\right\rangle \to \left\|S,\frac{1}{2}\right\rangle$	forbidden	ok
$\left\|\frac{3}{2},\frac{1}{2}\right\rangle \to \left\|S,-\frac{1}{2}\right\rangle$	forbidden	ok
$\left\|\frac{1}{2},\frac{1}{2}\right\rangle \to \left\|S,-\frac{1}{2}\right\rangle$	forbidden	ok
$\left\|\frac{1}{2},-\frac{1}{2}\right\rangle \to \left\|S,\frac{1}{2}\right\rangle$	ok	forbidden
$\left\|\frac{3}{2},-\frac{1}{2}\right\rangle \to \left\|S,\frac{1}{2}\right\rangle$	ok	forbidden
$\left\|\frac{3}{2},-\frac{3}{2}\right\rangle \to \left\|S,-\frac{1}{2}\right\rangle$	ok	forbidden
all other transitions	forbidden	forbidden

Table 2.1.: Optical selection rules for bulk semiconductors at the Γ-point, taken from [49]

2.5. Calculation of Coulomb matrix elements

In the most general form the Coulomb matrix elements are given by

$$V_{ijkl} = V_0 \iint \Psi_i^*(\boldsymbol{r}_1)\Psi_j^*(\boldsymbol{r_2})\frac{1}{|\boldsymbol{r}_1 - \boldsymbol{r_2}|}\Psi_k(\boldsymbol{r}_2)\Psi_l(\boldsymbol{r_1})d^3r_1d^3r_2 \tag{2.71}$$

To calculate the Coulomb matrix elements in the context of $\boldsymbol{k}\cdot\boldsymbol{p}$ theory one has to plug the proper wave function definitions into equation (2.71). As already pointed out the spinor expansion of a given wave function reads

$$\Psi_n(\boldsymbol{r}) = \sum_{j=1}^{8} F_{n,j}(\boldsymbol{r})U_j(\boldsymbol{r})$$

As Garcia pointed out [50] it is way more efficient to use the momentum space representation of equation (2.71) to calculate the Coulomb matrix elements. Using a symmetrized version of the Fourier transform (2.71) can be rewritten as

$$V_{ijkl} = \frac{1}{\sqrt{2\pi}^3}\int C_{il}(\boldsymbol{q})D_{jk}(\boldsymbol{q})V(\boldsymbol{q})d^3q \tag{2.72}$$

with

$$C_{ij}(\boldsymbol{q}) = \int \Psi_i^*(\boldsymbol{r})\Psi_j(\boldsymbol{r})e^{-i\boldsymbol{q}\cdot\boldsymbol{r}}d^3r \tag{2.73}$$

$$D_{ij}(\boldsymbol{q}) = \int \Psi_i^*(\boldsymbol{r})\Psi_j(\boldsymbol{r})e^{i\boldsymbol{q}\cdot\boldsymbol{r}}d^3r. \tag{2.74}$$

Inserting the spinor expansion into (2.73) yields

$$\begin{aligned} C_{ij}(\boldsymbol{q}) &= \sum_{n,m=1}^{8} \int F_{i,n}^*(\boldsymbol{r})U_n^*(\boldsymbol{r})F_{j,m}(\boldsymbol{r})U_m(\vec{r})e^{-i\boldsymbol{q}\cdot\boldsymbol{r}}d^3r \\ &= \sum_{n,m=1}^{8} \int F_{i,n}^*(\boldsymbol{r})F_{j,m}(\boldsymbol{r})e^{-i\boldsymbol{q}\cdot\boldsymbol{r}}U_n^*(\boldsymbol{r})U_m(\boldsymbol{r})d^3r \end{aligned} \tag{2.75}$$

Remembering that the $U_n(\boldsymbol{r})$ are rapidly oscillating over mesoscopic length scales one can consider the $F_{i,n}(\boldsymbol{r})$ as well as the phase term $\exp(-i\boldsymbol{q}\cdot\boldsymbol{r})$ as nearly constant within a unit cell of the crystal and decompose last integral into a product of two integrals

$$\begin{aligned} C_{ij}(\boldsymbol{q}) &\approx \sum_{n,m=1}^{8} \int F_{i,n}^*(\boldsymbol{r})F_{j,m}(\boldsymbol{r})e^{-i\boldsymbol{q}\cdot\boldsymbol{r}}d^3r \underbrace{\int_{UC} U_n^*(\boldsymbol{r})U_m(\boldsymbol{r})d^3r}_{=\delta_{n,m}} \\ &= \sum_{n}^{8} \int F_{i,n}^*(\boldsymbol{r})F_{j,n}(\boldsymbol{r})e^{-i\boldsymbol{q}\cdot\boldsymbol{r}}d^3r. \end{aligned} \tag{2.76}$$

In a similar manner one finds

$$D_{ij}(\boldsymbol{q}) = \sum_{n}^{8} \int F_{i,n}^*(\boldsymbol{r})F_{j,n}(\boldsymbol{r})e^{i\boldsymbol{q}\cdot\boldsymbol{r}}d^3r. \tag{2.77}$$

Once the individual spinor components of the considered wave functions are known the Coulomb matrix elements can be calculated quite efficiently by performing two Fast Fourier transforms (FFTs) and approximating (2.72) by a finite Riemann summation. Since $V(\boldsymbol{q})$ contains a $1/q^2$ singularity, the voxel at $q = 0$ has to be treated in a special way to get meaningful numerical results. Furthermore the FFT implicitly assumes periodic boundary conditions such that one needs to add a lot of empty space around the structure of interest to suppress artifacts from unphysical interactions with neighboring unit cells. An additional major drawback of this method is that it is only applicable in a homogeneous medium.
Another approach for efficient calculation of the Coulomb matrix elements in real space is the so called Poisson Green's function (PGF) method proposed by Zimmermann *et*

al. [51]. Equation (2.71) can be rewritten in the form

$$V_{ijkl} = \iint \rho_{il}(\boldsymbol{r}_1) G(\boldsymbol{r}_1, \boldsymbol{r}_2) \rho_{jk}(\boldsymbol{r}_2) d^3 r_1 d^3 r_2 \tag{2.78}$$

where

$$\rho_{il}(\boldsymbol{r}) = e\Psi_m^*(\boldsymbol{r})\Psi_p(\boldsymbol{r}) \tag{2.79}$$

$$\rho_{jk}(\boldsymbol{r}) = e\Psi_n^*(\boldsymbol{r}')\Psi_o(\boldsymbol{r}') \tag{2.80}$$

are generalized, potentially complex valued charge densities and $G(\boldsymbol{r}, \boldsymbol{r}')$ is a generalized Coulomb Green's function satisfying

$$\nabla_r \left(\varepsilon_r(\boldsymbol{r}) \nabla_r G(\boldsymbol{r}, \boldsymbol{r}')\right) = -\frac{1}{\varepsilon_0} \delta(\boldsymbol{r} - \boldsymbol{r}') \tag{2.81}$$

In case of a constant relative permittivity (2.81) reduces to the defining equation for the free space Coulomb Green's function. At this point it is advantageous to slightly rewrite equation (2.78) to the following form

$$V_{ijkl} = \int \rho_{jk}(\boldsymbol{r}_2) \int G(\boldsymbol{r}_1, \boldsymbol{r}_2) \rho_{il}(\boldsymbol{r}_1) d^3 r_1 d^3 r_2. \tag{2.82}$$

The rightmost integral in the last equation can be identified as the Green's function representation of a generalized electrostatic potential satisfying Poisson's equation in a spatially inhomogeneous medium

$$\nabla_r \left(\varepsilon_r(\boldsymbol{r}) \nabla_r \Phi(\boldsymbol{r})\right) = -\frac{\rho(\boldsymbol{r})}{\varepsilon_0} \tag{2.83}$$

which allows a last reformulation of the Coulomb matrix elements

$$V_{ijkl} = \int \rho_{jk}(\boldsymbol{r}_2) \Phi_{il}(\boldsymbol{r}_2) d^3 r_2. \tag{2.84}$$

In contrast to the original definition (2.71) this expression requires a single spatial integral instead of a double integral which drastically reduces the computational costs for evaluation of the Coulomb matrix elements numerically. However, now one needs efficient ways to solve (2.83) in the first place as the determination of the generalized electrostatic potential is now the most time consuming part in the evaluation of (2.84). A semi efficient procedure to calculate the Coulomb matrix elements may look as follows:

1. Pick a particular index pair (i, l)
2. Calculate the generalized electrostatic potential $\Phi_{il}(\boldsymbol{r})$ from (2.83)

3. For all appearing pairs (j,k) calculate V_{ijkl} from (2.84)
4. Repeat for all other pairs (i,l)

Looking at the original definition (2.71) of the Coulomb matrix elements one can easily verify the following symmetry relations:

$$V_{ijkl} = V_{jilk} = V^*_{klij} = V^*_{lkji}$$

Using these symmetry relations one may come up with a more effective way to calculate the Coulomb matrix elements for a given basis set of eigenstates.

```
Data: The $N$ envelope wave functions of the basis states
Result: The $N^4$ Coulomb matrix elements $V_{ijkl}$
Set up a dictionary $D$ for all index tuples $(i,j,k,l)$ initializing the mapped
  value to true;
for $i = 1$ to $N$ and $l = m$ to $N$ do
    Calculate $\rho_{jk}(\boldsymbol{r})$;
    Calculate $\Phi_{il}(\boldsymbol{r})$ from (2.83);
    for $j = i$ to $N$ and $k = i$ to $N$ do
        if $D[(i,j,k,l)]$ is set to true then
            Calculate $\rho_{jk}(\boldsymbol{r})$;
            Calculate $V_{ijkl}$ from (2.84);
            Set the values of $V_{jilk}$, $V_{klij}$, and $V_{lkji}$ as well;
            Set $D[(i,j,k,l)]$, $D[(j,i,l,k)]$, $D[(k,l,i,j)]$, and $D[(l,k,j,i)]$ to
              false;
        else
            Pick the next index
        end
    end
end
```

Algorithm 1: Calculation of the Coulomb matrix elements

Considering a basis set of 16 eigenstates one can compute the $16^4 = 65536$ matrix elements with just 136 calculations of an electrostatic potential.

2.5.1. Approximating open boundary conditions

The implemented algorithm for calculation of the generalized electrostatic potential uses a finite difference approximation of the Laplacian operator, mapping the differential equation (2.83) onto a sparse linear system. This system is solved using an algebraic multigrid solver [52].

As shown in the last section, the calculation of the Coulomb matrix elements - as performed within this work - is a two-stage process involving the determination of a generalized electrostatic potential. The proper choice of boundary conditions is quite crucial since they implicitly define the solution of the electrostatic problem. In the given situation the problem is to find boundary conditions for the electrostatic potential at a finite distance from a given charge distribution while maintaining compatibility with an open space solution where the usual boundary condition is imposed in the form

$$\varphi(\boldsymbol{r}) \underset{r\to\infty}{\to} 0. \tag{2.85}$$

However, in practical calculation one is naturally confronted with a finite computational domain. In this situation forcing the electrostatic potential to zero would be equivalent to introducing image charges outside the computational domain, which ultimately falsifies the resulting potential inside the computational domain. A systematic way to suppress this error would be to add enough space around the given charge density such that the potential is already close to zero on the boundary of the computational domain. Considering one-dimensional or two-dimensional problems this is a reasonable way. In three dimensions, however, this approach is not feasible any more since the computational effort and the required memory to solve the problem grow rapidly to unpractical scales.

A variety of methods to mimic open boundary conditions have been developed for algorithms using finite element methods. A feature common to most of these methods is a partition of open space into an interior region, i.e. the actual computational domain and an exterior region, see figure 2.3.

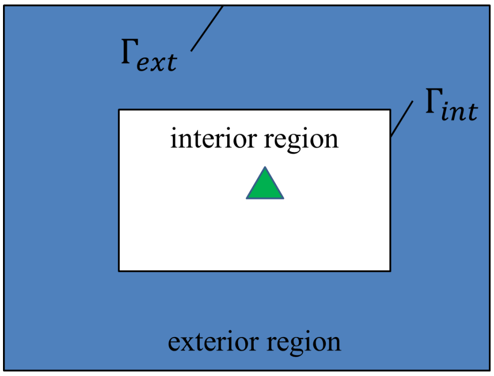

Figure 2.3.: Schematic partition of the unbounded open space into an interior and an exterior region. Left: The interior region is the actual computational domain whereas the treatment of the exterior region depends on the applied method. The boundary Γ_{ext} of the exterior region is understood in the limit $r \to \infty$.

The first mentioned truncation approach means setting $\varphi(\boldsymbol{r}) = 0$ for $\boldsymbol{r} \in \Gamma_{int}$. A simple improvement over this method has been introduced by Saito *et al.* [53]. They determine two potential solutions, one of them using homogeneous Dirichlet boundary conditions and one using homogeneous Neumann boundary conditions. The final potential is then calculated averaging the two individual solutions.

Other methods rely on so called infinite elements which mimic the infinite extent of the exterior domain by introduction of suitable decay functions to the finite elements [54] or by singular mappings of the infinite space to a finite one [55].

Another interesting approach is application of so called asymptotic boundary conditions, see for example [56, 57] or [58]. This makes use of the already mentioned partition of the open space into two regions. In addition this approach utilizes the assumption that the exterior region of the problem is source free, i.e. the electrostatic potential satisfies the simple Laplace equation $\Delta\varphi(\boldsymbol{r}) = 0$. Making use of that assumption, the potential in the exterior region is expressed via a multipole expansion in spherical coordinates. Then special boundary operators which exactly cancel the first few multipoles, mostly up to second order with a remainder term $\mathcal{O}(r^{-5})$, are introduced and used to generate equations for the potential on Γ_{int}. Meeker [58] goes one step further by introducing several artificial layers around the structure of interest damping the potential more slowly towards zero. The drawback of this approach is that it relies on spherical coordinates which makes the application to systems without spherical symmetry somewhat hard.

A lot more approaches to approximate an infinite open space have been taken. A review article by Chen *et al.* [59] lists 158 publications on that topic, two of which are review articles by themselves listing even more publications. However, as it seems, only the so called measured equation of invariance [60] would be applicable to a finite differencing approach for solution of Poisson's equation. However, this method relies on the choice of suitable measuring functions.

In this work an approach similar to the asymptotic boundary conditions in finite elements is chosen. The infinite open space is partitioned into an exterior and an interior region, see figure 2.4. It is assumed that the unknown boundary values of the potential on Γ_{int} can be described reasonably well by a finite generalized multipole expansion. Here, however, the multipole boundary conditions are not implemented by a special set of boundary operators. Instead, the following procedure is used. The generalized charge density defined only inside the interior region is used to calculate generalized monopole, dipole, and quadrupole moments. From these generalized multipole moments the potential sufficiently far away from the generalized charge density can be approximated as

$$\varphi(\boldsymbol{r}) \approx \varphi_m(\boldsymbol{r}) + \varphi_d(\boldsymbol{r}) + \varphi_q(\boldsymbol{r}) \tag{2.86}$$

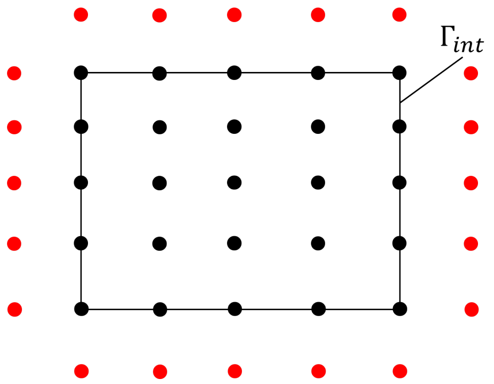

Figure 2.4.: Schematic illustrating the application of multipole Dirichlet Boundary conditions. The black dots indicate regular grid points discretizing the interior region of the problem. The red dots indicate grid points outside the region of interest to which the multipole boundary conditions are applied.

with

$$\varphi_m(\boldsymbol{r}) = \frac{Q}{4\pi\varepsilon r} \tag{2.87}$$

$$\varphi_d(\boldsymbol{r}) = \frac{1}{4\pi\varepsilon}\frac{\boldsymbol{p}\cdot\boldsymbol{r}}{r^3} \tag{2.88}$$

$$\varphi_q(\boldsymbol{r}) = \frac{1}{4\pi\varepsilon}\frac{\boldsymbol{r}^T\cdot\boldsymbol{Q}\cdot\boldsymbol{r}}{2r^5} \tag{2.89}$$

where Q is a generalized potentially complex valued charge, $\boldsymbol{p}$ is the generalized dipole moment and $\boldsymbol{Q}$ is the generalized quadrupole tensor.
Discretizing the region of interest by a rectilinear grid with N_x, N_y, and N_z grid points in x-, y-, and z-direction respectively, each point inside the region of interest is uniquely defined by three indices i, j, and k where $i \in [0; N_x - 1]$, $j \in [0; N_y - 1]$, and $k \in [0; N_z - 1]$. This results in a finite set of sampled potential values $\varphi(\boldsymbol{r}_{ijk}) =: \varphi_{ijk}$. Using a second order accurate finite difference stencil, the discretized version of Poisson's equation is given as

$$\begin{aligned} -\frac{\rho(\boldsymbol{r}_{ijk})}{\varepsilon} =& \frac{\varphi_{i+1jk}+\varphi_{i-1jk}}{\Delta x^2} + \frac{\varphi_{ij+1k}+\varphi_{ij-1k}}{\Delta y^2} + \frac{\varphi_{ijk+1}+\varphi_{ijk-1}}{\Delta z^2} \\ &- 2\left(\frac{1}{\Delta x^2}+\frac{1}{\Delta y^2}+\frac{1}{\Delta z^2}\right)\varphi_{ijk} \end{aligned} \tag{2.90}$$

Considering figure 2.4 as a cut plane through the interior region at a fixed value of k, it becomes obvious that, in order to solve (2.90), one needs the potential values at coordinates $i = -1$, $i = N_x$, $j = -1$, and $j = N_y$. However, using the known mapping $(ijk) \rightarrow \boldsymbol{r}_{ijk}$, equations (2.86)-(2.89) can be used to calculate the needed potential values. The respective terms are then brought to the left hand side of (2.90), i.e. the boundary conditions are incorporated by correcting the generalized charge density. Repeating this procedure for all boundary points yields a closed linear set of $N_x \cdot N_y \cdot N_z$ equations for the unknown potential values inside the interior region. As already mentioned, within this work an algebraic multigrid solver [52] is used to solve the respective system[3]. Algebraic multigrid methods [61] are similar to geometric multigrid methods [62] in the sense that the iterative solution of a given system is accelerated by interpolation between finer (more equations) and coarser (fewer equations) systems. Algebraic multigrid methods, however, have the clear advantage that they do not rely on any geometrical information and perform the coarsening and interpolation purely based on the structure of the coefficient matrix which easily allows application of algebraic multigrid methods to problems involving unstructured meshes. Geometric multigrid methods on the other hand usually set up a grid hierarchy by incrementally doubling the step size of a given grid in each dimension. This restricts the applicability of geometric multigrid methods to problems defined on rectilinear grids. To make the maximum number of coarsenings possible, the number of grid points in each direction has to be of the form $N_\nu = 2^n + 1$ for some $n > 1$. Otherwise the grid hierarchy has to be truncated after ~3 levels to keep the boundary points.

As benchmark problems, systems with a known analytical solution have been investigated. Namely a homogeneously charged sphere, a Gaussian charge distribution, a physical dipole as well as a physical quadrupole consisting of homogeneously charged spheres.

Figure 2.5 shows an overview for the benchmark system consisting of a homogeneously charged sphere centered at the origin of the computational domain. The radius of the sphere has been chosen to be 5 a.u. where the total simulation domain is a cube with a side length of 40 a.u. with the origin of the coordinate system centered at the center of the cube. The charge density and the analytical known potential are given by

$$\rho_{sph}(\boldsymbol{r}) = \frac{Q}{V} \begin{cases} 1 & r \leq R \\ 0 & r > R \end{cases} \tag{2.91}$$

$$\varphi_{sph}(\boldsymbol{r}) = \frac{Q}{4\pi\varepsilon_0} \begin{cases} \frac{1}{r} & r > R \\ \frac{1}{R}\left(\frac{3}{2} - \frac{r^2}{2R^2}\right) & r \leq R \end{cases} \tag{2.92}$$

where R is the radius and V is the volume of the sphere. The charge density is chosen such that the integrate charge equals one[4].

---

[3] To be precise, the AMGCL library uses the multigrid iteration as a preconditioner for other iterative methods

[4] The actual units of lengths and charge provide just an internal scaling of the obtained solution such that they do not play an important role for the current benchmarking purposes.

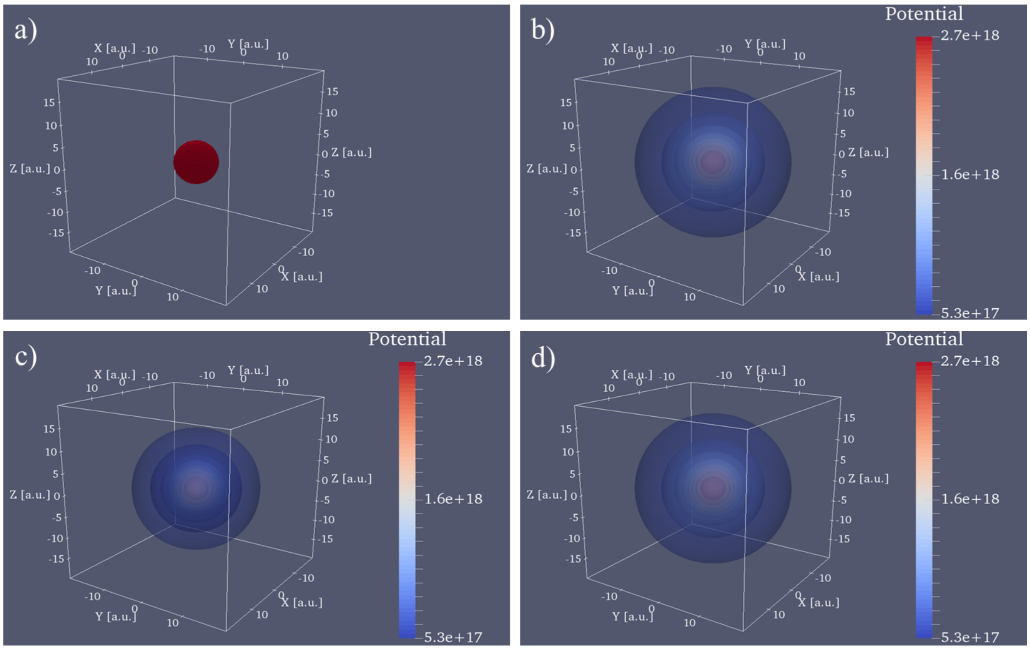

Figure 2.5.: Benchmark of the multipole Dirichlet boundary conditions for a homogeneously charged sphere. a) Discretized charge density, b) the analytically known potential, c) numerical solution using homogeneous Dirichlet boundary conditions, and d) numerical solution using multipole boundary conditions.

Looking at the isosurface plots, one easily observes significant deviations of the numerical potential obtained using homogeneous Dirichlet boundary conditions (figure 2.5 c)) from the analytically known solution (figure 2.5 b)). Although not quite visible in figure 2.5, due to the homogeneous boundary conditions on all given boundaries the obtained potential does not show the spherical symmetry one would expect given the spherically symmetric charge density. The more obvious deviation is the fast decrease of the numerical solution when approaching one of the boundaries.

In contrast, the solution using multipole boundary conditions (figure 2.5 d)) shows almost no deviations from the analytically known solution.

An overview of the benchmark system of a Gaussian charge distribution is given in figure 2.6. The system consists of a single Gaussian charge distribution centered at the origin of the computational domain. The charge distribution and the analytically known potential are given by

$$\rho_G(\boldsymbol{r}) = \frac{Q}{\sigma^3\sqrt{2\pi}^3} e^{-\frac{r^2}{2\sigma^2}} \tag{2.93}$$

$$\varphi_g(\boldsymbol{r}) = \frac{Q}{4\pi\varepsilon_0 r} \operatorname{erf}\left(\frac{r}{\sqrt{2}\sigma}\right) \tag{2.94}$$

where σ is the decay length of the Gaussian function.

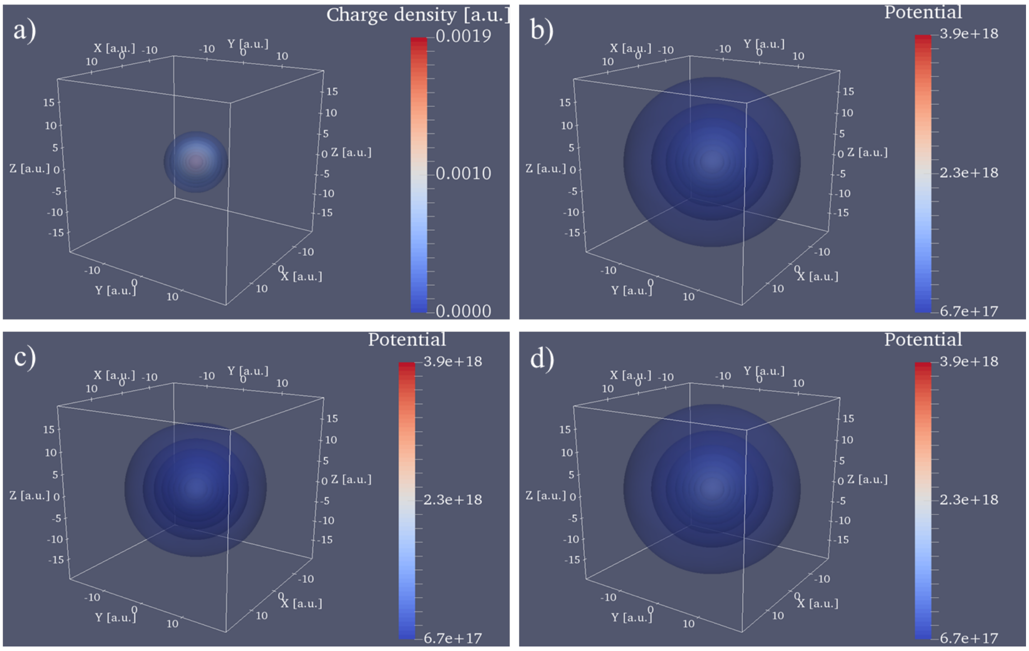

Figure 2.6.: Benchmark of the multipole Dirichlet boundary conditions for a Gaussian charge distribution. a) Discretized charge density, b) the analytically known potential, c) numerical solution using homogeneous Dirichlet boundary conditions, and d) numerical solution using multipole boundary conditions.

As in the case of the homogeneously charged sphere, the charge density has been normalized such that the integrated charge equals one. Again, the computational domain is a cube of side length 40 a.u. with the origin of the coordinate system centered at the center of the computational domain. The decay length for the Gaussian has been chosen isotropic for all three coordinates such that one side of the computational domain spans over six decay lengths. As could be expected, the results obtained in this case are quite similar to those obtained for the homogeneously charged sphere. In case of homogeneous Dirichlet boundary conditions, the numerical solution of Poisson's equation drops off too fast. Again, not quite visible in 2.6 c), the numerical solution does not show the spherical symmetry expectable from the spherical symmetry of the charge distribution.

As for the homogeneously charged sphere, the numerical solution obtained using multipole boundary conditions shows almost no deviations from the analytical solution.

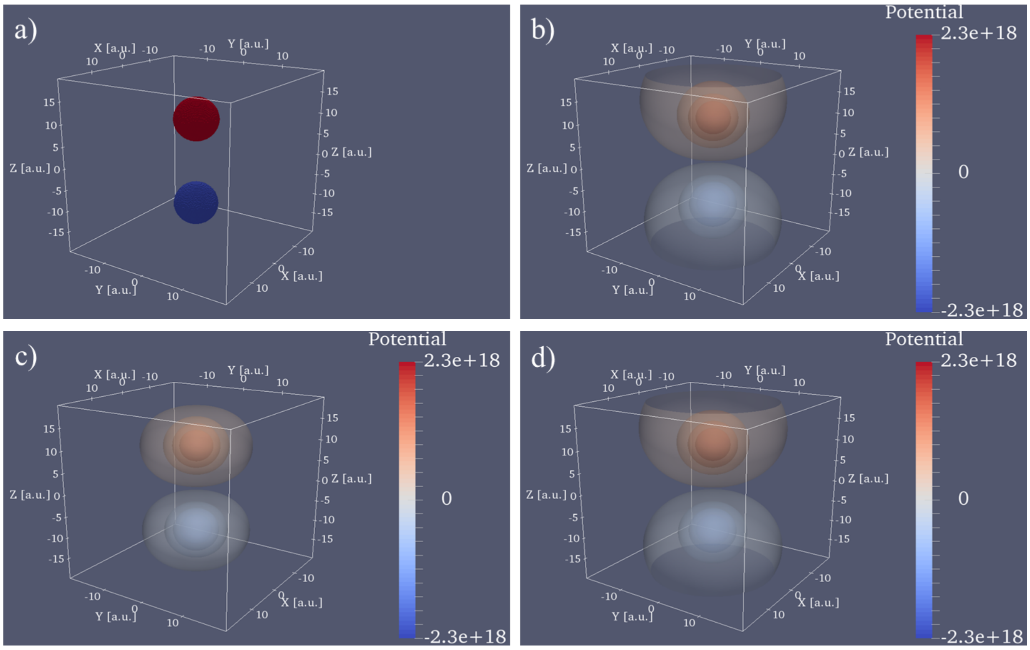

Figure 2.7.: Benchmark of the multipole Dirichlet boundary conditions for a physical dipole consisting of two homogeneously charged spheres. a) Discretized charge density, b) the analytically known potential, c) numerical solution using homogeneous Dirichlet boundary conditions, and d) numerical solution using multipole boundary conditions.

Figure 2.7 and 2.8 give an overview over the physical dipole and quadrupole respectively. Both systems have been chosen to consist of several homogeneously charged spheres. To this end, the charge density and the analytically known potential may be written in terms of the charge density and potential of a homogeneously charged sphere.

$$\rho(\boldsymbol{r}) = \sum_i \rho_{sph}(\boldsymbol{r} - \boldsymbol{r}_i) \tag{2.95}$$

$$\varphi(\boldsymbol{r}) = \sum_i \varphi_{sph}(\boldsymbol{r} - \boldsymbol{r}_i) \tag{2.96}$$

In case of the physical dipole the system consists of one homogeneously charged sphere of integrated charge equal to one at $\boldsymbol{r} = (0, 0, 10)^T$ (the red sphere in figure 2.7 a)) and another homogeneously charged sphere of integrated charge equal to minus one at $\boldsymbol{r}(0, 0, -10)^T$ (the blue sphere in figure 2.7 a)). Similarly the physical quadrupole is given by two homogeneously charged spheres each of integrated charge equal to one at $\boldsymbol{r} = (0, 0, 10)^T$ and $\boldsymbol{r} = (0, 0, -10)^T$ (the red spheres in figure 2.8 a)) and two other homogeneously charged spheres each of integrated charge equal to minus one at $\boldsymbol{r} = (10, 0, 0)^T$ and $\boldsymbol{r} = (-10, 0, 0)^T$ (the blue spheres in figure 2.8 a)).

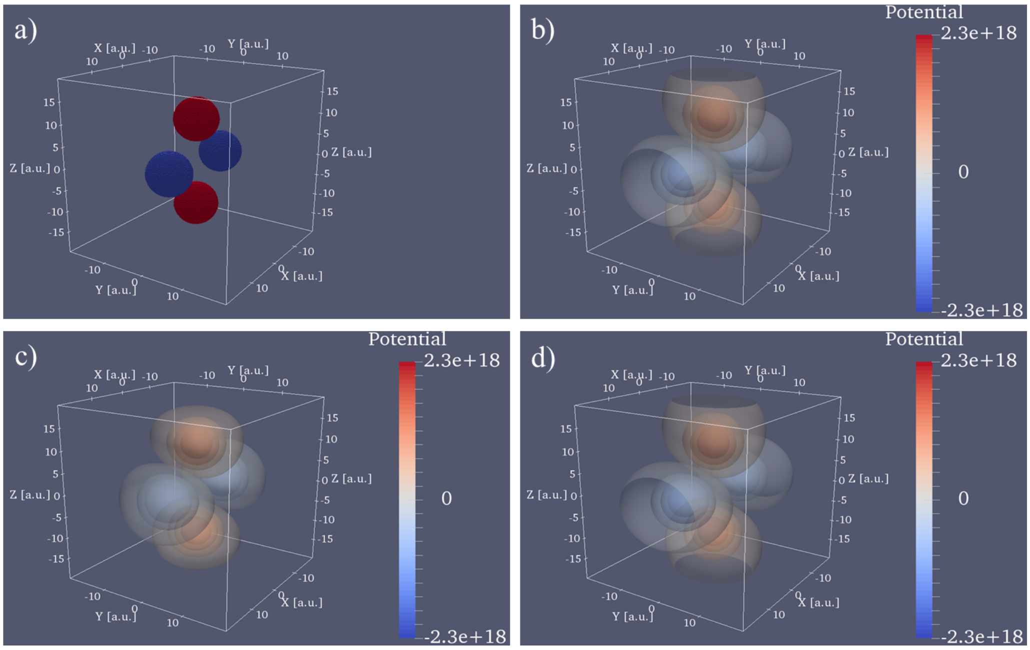

Figure 2.8.: Benchmark of the multipole Dirichlet boundary conditions for a physical quadrupole consisting of four homogeneously charged spheres. a) Discretized charge density, b) the analytically known potential, c) numerical solution using homogeneous Dirichlet boundary conditions, and d) numerical solution using multipole boundary conditions.

So far only a qualitative comparison of the two boundary conditions has been given. In order to give a quantitative comparison, the potential calculations have been performed on a series of grids with decreasing grid spacing while keeping the total extent of the computational domain fixed. The number of grid points per direction ranged from 51 to 201 giving grid spacings in the range from about 0.2 to about 0.8 arbitrary units. Figures 2.9-2.12 show the benchmark results for the individual systems. The shown error measure ε_{rel} is given as

$$\varepsilon_{rel} = \frac{\|\varphi_{ref} - \varphi_{num}\|}{\|\varphi_{ref}\|} \tag{2.97}$$

with the norm defined as

$$\|\varphi\| = \sqrt{\sum_{ijk} \varphi^*_{ijk}\varphi_{ijk}} \tag{2.98}$$

For each grid spacing special care has been taken to maintain the aforementioned normalizations of the individual charge distributions in order to keep a fair comparison to the analytical solution. Figures 2.9-2.12 show the benchmark results of the individual systems.

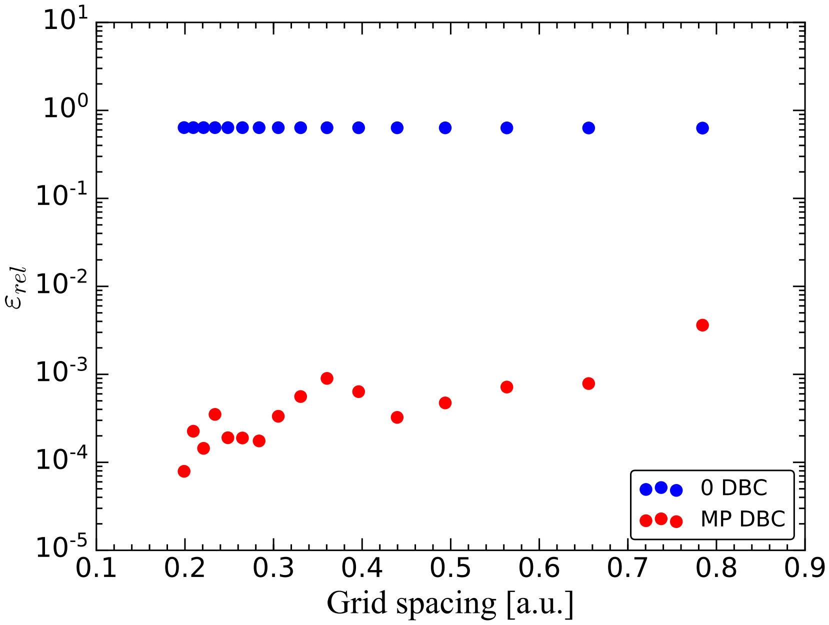

Figure 2.9.: Grid study for performance of the multipole Dirichlet boundary conditions for a homogeneously charged sphere.

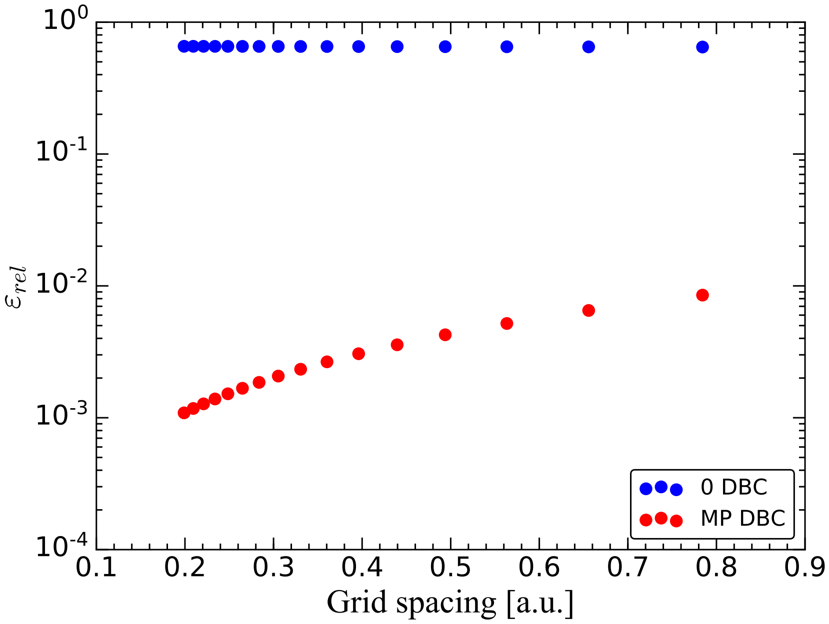

Figure 2.10.: Grid study for performance of the multipole Dirichlet boundary conditions for a Gaussian charge distribution.

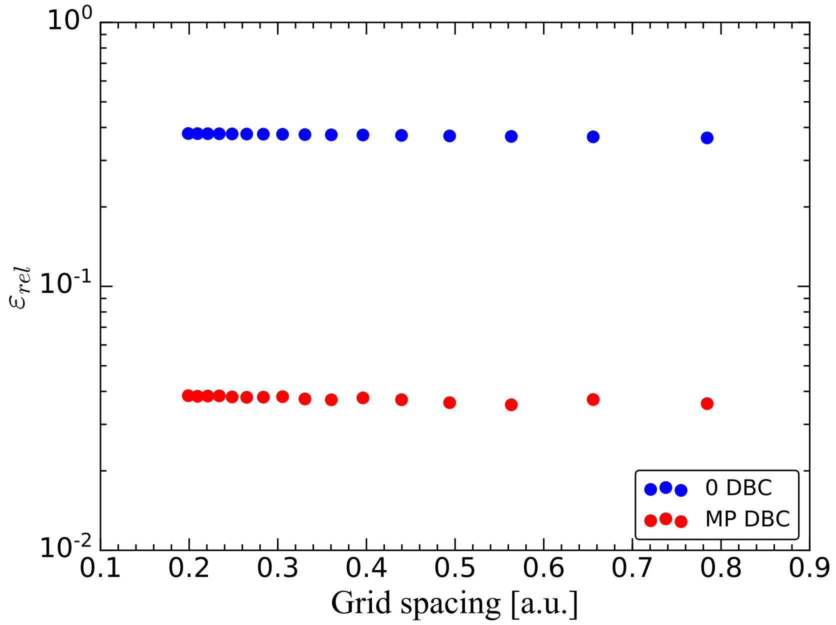

Figure 2.11.: Grid study for performance of the multipole Dirichlet boundary conditions for a physical dipole consisting of two homogeneously charged spheres.

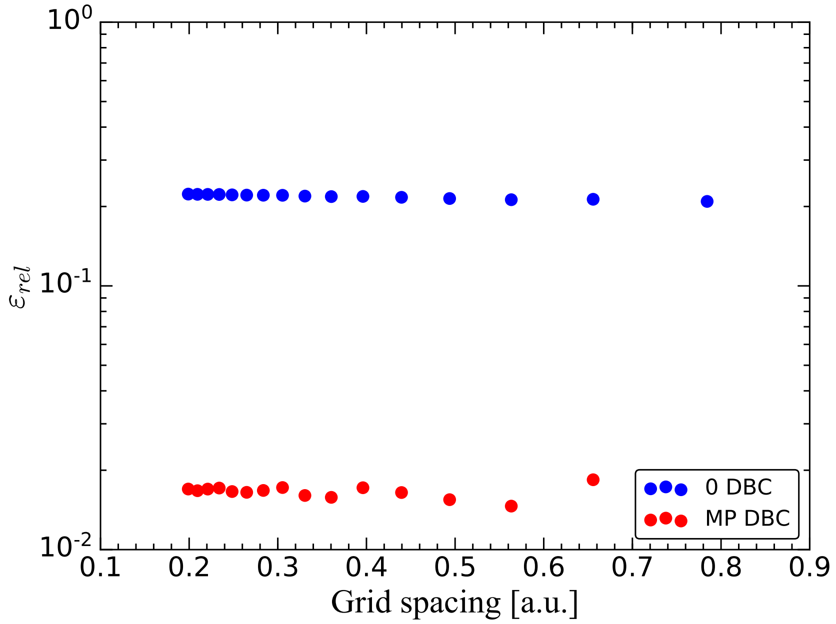

Figure 2.12.: Grid study for performance of the multipole Dirichlet boundary conditions for a physical quadrupole consisting of four homogeneously charged spheres.

Figures 2.13 and 2.14 summarize the grid studies for the individual systems.

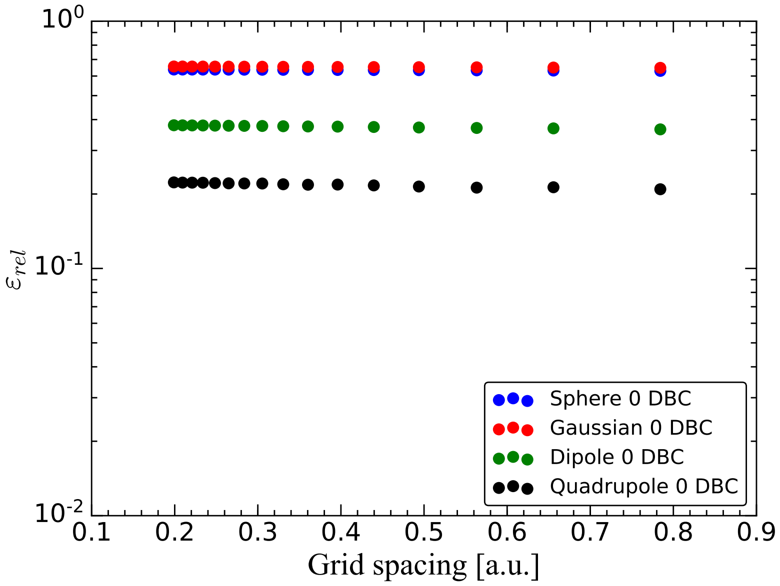

Figure 2.13.: Overview of the grid studies for the considered benchmark systems using homogeneous Dirichlet boundary conditions.

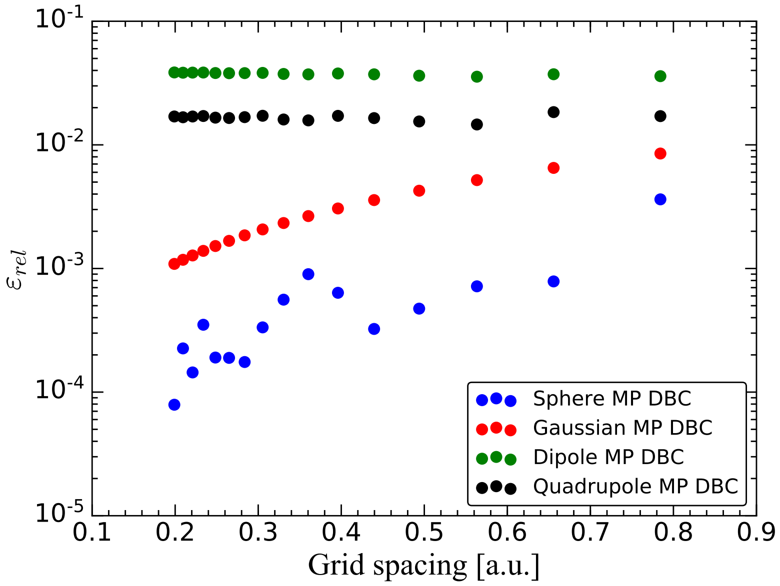

Figure 2.14.: Overview of the grid studies for the considered benchmark systems using multipole Dirichlet boundary conditions.

As can be seen, the integrated relative error for the charge distributions exhibiting a finite monopole moment is reduced by almost three orders of magnitude without substantially increasing the computational burden. At first glance one would expect the error to decrease in both cases with decreasing grid spacing. However, as the absolute size of the computational domain is kept fixed, decreasing the grid spacing means introducing new cells with erroneous potential values. Looking back at the definition of the used norm, the grid spacing does not enter the norm such that one observes an increasing error with decreasing grid spacing in case of homogeneous Dirichlet boundary conditions.

Considering the seemingly poor performance of the multipole boundary conditions in case of the physical dipole and quadrupole, one has to remember that the estimated boundary values for the potential are calculated from the potentials of pure dipoles and quadrupoles respectively. Given that, in the current setup, the boundaries of the computational domain are quite close to the considered charge distributions, significant deviations were to be expected. Figure 2.15 shows the benchmark results for a more compact physical quadrupole with longer distance to the boundaries of the computational domain.

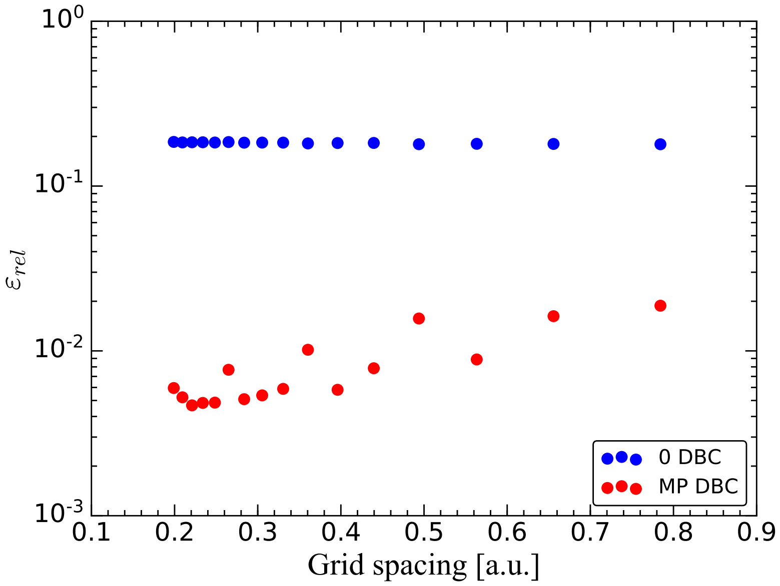

Figure 2.15.: Overview of the grid studies for the considered benchmark systems using multipole Dirichlet boundary conditions.

The error now shows the desired behavior for decreasing grid spacings in case of multipole Dirichlet boundary conditions. As the monopole is the leading term in the multipole expansion, this term is expected to contribute the most to the global error

of the solution. Keeping in mind fabrication tolerances in the experiment, the current implementation with a relative error on the order of 10^{-4} for the monopole term should deliver results with reasonable accuracy.
A noteworthy point is that, strictly speaking, the multipole expansion works only for homogeneous problems. If material inhomogeneities extend into the boundary region, the estimated boundary values of the potential may differ significantly from the true ones. In the current implementation the potential is calculated from a homogeneous Poisson equation where the position dependent permittivity in (2.83) is replaced by a volume averaged static permittivity.

2.5.2. Symmetry considerations on the optical and Coulomb matrix elements

As has been shown in the last two sections, both, optical and Coulomb matrix elements are determined by the shape of the single particle wave functions which of the involved eigenstates. Since the shape of these wave functions is determined by the symmetry of the underlying crystal lattice and, in case of heterostructures, the symmetry of the given heterostructure, one may try to predict the matrix elements based on symmetry considerations. Bester *et al.* have studied the influence of lattice symmetry on the symmetry of heterostructures by taking examples of InAs quantum dots of different shapes embedded in a GaAs host matrix. A first key point that is pointed out is, that quantum dots usually have a lower symmetry than is suggested by the shape of the material distribution. Considering the lens shaped semiconductor quantum dots discussed later in this work, the material distribution itself gives a so called $C_{\infty v}$ symmetry [65]. This means that one may rotate the structure by an arbitrary angle about the vertical growth direction without changing it. As Bester *et al.* point out [65], the overall symmetry is reduced to C_{2v} due to the zinc-blende symmetry of the underlying crystal lattice. The so called character table of the C_{2v} symmetry group is shown in table 2.2. Where E denotes the neutral or unit element, C_2 denotes a two-fold rotation about the z-axis, σ_x a reflection about the xz-plane and σ_y a reflection about the yz-plane respectively. The symbols in the first column denote the so called irreducible representations whereas the second column gives basis functions which are invariant

C_{2v}	Basis	E	C_2	σ_x	σ_y
A_1	z, x^2, y^2, z^2	1	1	1	1
A_2	xy	1	1	-1	-1
B_1	x, xz	1	-1	1	-1
B_2	y, yz	1	-1	-1	1

Table 2.2.: Character table of the C_{2v} symmetry group, see e.g. [63, 64]

(up to a constant factor) under the symmetry transformations of the group. When considering selection rules, one is interested in expectation values of the form

$$\left\langle \phi_l^{(\gamma)} \middle| T^{(\alpha)} \middle| \phi_m^{(\beta)} \right\rangle \tag{2.99}$$

where the actual value is of secondary importance. At first, one is interested whether the respective integral evaluates to zero or a finite value. If the integral evaluates to a finite value, it describes an allowed transition. On the other hand, if the integral evaluates to zero, the transition is forbidden. Following the reasoning in [63, 64] it is sufficient to consider basis functions $\phi_m^{(\beta)}$ for a particular irreducible representation $D^{(\beta)}$ and basis functions $\phi_l^{(\gamma)}$ corresponding to a irreducible representation $D^{(\gamma)}$. If the operator $T^{(\alpha)}$ transforms according to a irreducible representation $D^{(\alpha)}$, then the transformed functions $T^{(\alpha)}\phi_m^{(\beta)}$ will transform according to the product representation $[D^{(\alpha)} \times D^{(\beta)}]$ which may be reduced to a new representation $D^{(\alpha\times\beta)}$. According to [63] the expectation value (2.99), due to a fundamental orthogonality relationship for basis functions of irreducible representations of a given group $\mathcal{G}$, is only symmetry allowed if the basis $\phi_l^{(\gamma)}$ is contained in $D^{(\alpha\times\beta)}$.

For lens shaped Nitride quantum dots grown on a Wurzite substrate, Baer [66] has shown that 1S-1S and 1P-1P optical transitions may not take place due to the reduced C_{3v} symmetry of the system. Similar results were found by Heitz *et al.* [67] for pyramidal shaped InAs quantum dots which exhibit a C_{4v} symmetry. In case of C_{2v} symmetry the aforementioned transitions are allowed. For the Coulomb matrix elements Baer has shown, that additional matrix elements arise for the reduced symmetry compared to the $C_{\infty v}$ symmetry of the material distribution.

For lens shaped InAs/GaAs quantum dots Narvaez and Zunger predicted the presence of optical transitions which would not be expected from effective mass models. However, the authors do not attribute this nominally forbidden transitions to a reduced symmetry, but to finite band offsets and many body effects.

2.6. Properties of selected Quantum Dot Systems

This section presents the results of electronic structure calculations for different semiconductor quantum dot systems. The presented systems consider InAs quantum dots embedded in a GaAs host matrix, starting from the most simple model of a spherical quantum dot, over an ellipsoidal quantum dot, to a model considered most realistic based on the findings of Scheibner *et al.* [26]. The simpler models serve to show the general shape dependence and consider pure binary materials, i.e. the quantum dot regions contain pure InAs. The calculations for these models take all strain effects into account. For the model of a lens shaped quantum dot the influence of strain and inhomogeneous material distributions inside the quantum dots will be treated in further detail. Later on, the system of a quantum dot molecule consisting of two vertically stacked quantum dots will be treated. Within the respective subsections, results of the electronic structure calculations obtained from the nextnano++ software package as well as the optical and Coulomb matrix elements calculated from the nextnano++ output will be presented. If not explicitly stated otherwise, calculations have been performed considering each eight hole and electron states closest to the fundamental energy gap between the electron and hole states. For each considered system, a table containing the projections of the calculated eigenstates onto the bulk eigenstates is given in appendix B. Although these numbers lack phase information, they can give a first hint about changed optical selection rules due to state mixing.

A note on naming conventions for the forthcoming sections is in order to avoid misunderstandings or confusion of concepts. The term band gap is used for the energy gap between the hole eigenstate with the highest energy and the electron eigenstate with the lowest energy for the respective quantum dot system, not for the fundamental energy gap between conduction band states and valence band states of the bulk materials. Similarly, the term bandedge refers to the lowest lying electron or highest lying hole eigenvalue respectively, not to the actual bandedge of the underlying bulk materials.

In order to give a proper picture of the upcoming results, a side note of the boundary conditions has to be given. The system of the given spherical quantum dot has been calculated taking into account all strain effects using a 'safety-distance' of 30 nm to the actual end of the computational domain. The shown pictures only show the region treated quantum-mechanically. As can be seen in the projection tables in the appendix, the hole eigenstates show a significant state mixing. To this end one should not expect the hole eigenfunctions to resemble atomic functions. The substrate condition (0-displacement) has been imposed on the lower boundary of the total computational domain. Accordingly one should observe effects due to the broken symmetry.

2.6.1. Spherical Quantum Dot

The general model considered for spherical quantum dot is depicted in figure 2.16. Here a spherical quantum dot of pure InAs embedded in a GaAs host matrix is assumed. The diameter of the quantum dot is chosen as $d = 14.6$nm which is already relatively large. However, this model is not supposed to reproduce any experimental data. For the moment one can assume that the size of the quantum dot just affects the confinement energies and such the energy gap between the electron and the hole states. Due to the spherical symmetry, the calculated eigenstates should look quite similar to atomic s- and p-orbitals. However, this model is not supposed to reproduce any experimental data. For the moment one can assume that the size of the quantum dot just affects the confinement energies and such the energy gap between the electron and the hole states.

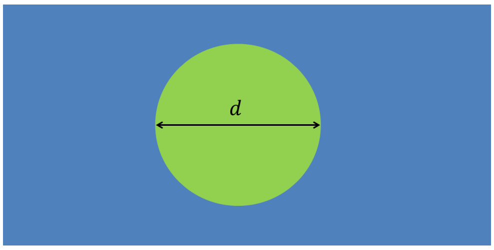

Figure 2.16.: Model of a simple spherical quantum dot. For a spherical quantum dot the only parameter is its diameter, denoted as d The blue region corresponds to the GaAs host matrix whereas the green region is filled with InAs.

The calculated spectrum for the electron eigenstates (indices 9 and higher) in figure 2.17 looks quite similar to an atomic system.

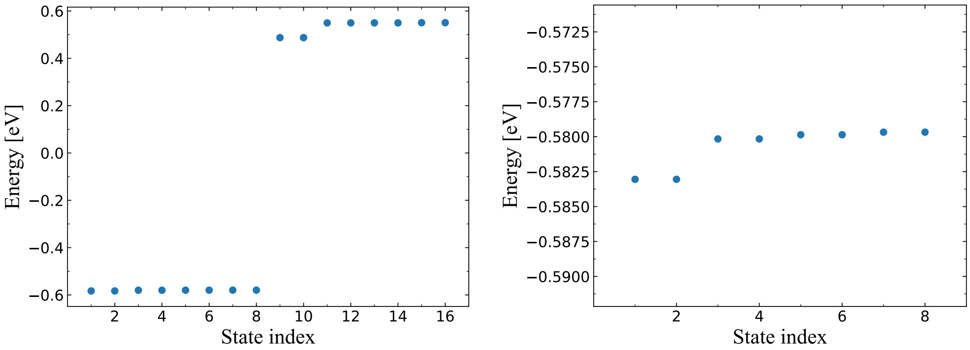

Figure 2.17.: Eigenvalue spectrum of a spherical quantum dot. Left: Eigenvalues for all considered electron and hole states. Right: Eigenvalues of the considered hole states.

It consists of two degenerate eigenvalues directly at the band edge and a series of six degenerate eigenvalues at a slightly higher energy. For the hole eigenstates (state indices 1–8), the situation is quite different from what could be expected from simple symmetry considerations, as can be seen on the right in figure 2.17. The considered group of hole states can be divided into four pairs of degenerate eigenvalues. This is a clear indication, that the symmetry breaking due to strain affects the hole eigenstates much stronger than the electron states. Although this can only give a hint, a look at the projections of the eigenstates onto the eigenstates of the total angular momentum operator in table **??** in appendix B can help to clarify this. For the hole eigenstates one observes a significant mixing of heavy hole and light hole states regardless of the state index. For the electrons on the other hand, one observes a much weaker mixing with one of the bulk eigenstates clearly dominating. However, as the eigenvalue spectrum and the projections onto bulk eigenstates give only limited information about the actual symmetries of the calculated eigenstates, one has to look at the wavefunctions to get a more complete picture.

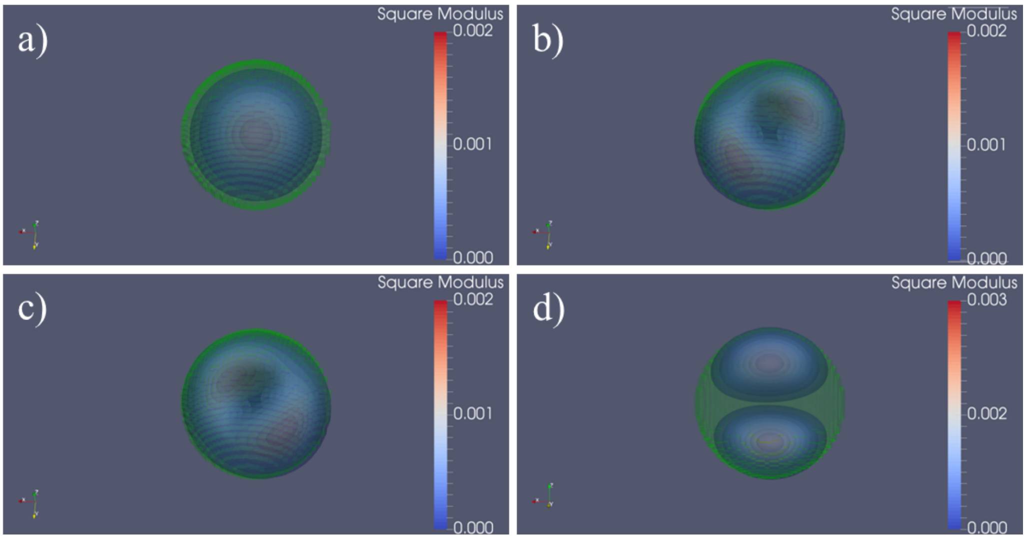

Figure 2.18.: Square modulus of the first eight electron wavefunctions for a spherical quantum dot. As the eigenstates are spin-degenerate, only the four unique profiles of the square modulus of the wavefunctions are shown: a) Square modulus of the s-like electron wavefunctions, b) and c) linear combinations of p_x- and p_y-like wavefunctions, and d) p_z like wavefunctions

Figure 2.18 shows the square moduli of the eight calculated electron eigenstates. As the states are spin degenerate, only the four unique profiles are shown. The shown square moduli have symmetries which would have been expected from the spherical symmetry of the material distribution. The first two eigenstates show a spherical symmetry similar to an atomic $s-$orbital while the next four eigenstates could be interpreted as a linear combination of p_x- and p_y orbitals. The last two eigenstates show the symmetry of an atomic p_z-orbital. For the hole eigenstates, the picture looks quite different. Here one finds a series of almost $p-$like wavefunctions shifted towards the upper hemisphere of the quantum dot as can be seen in figure 2.19. For the wavefunctions shown in figure 2.19 c) and d) one even observes two local maxima of the square modulus per lobe.

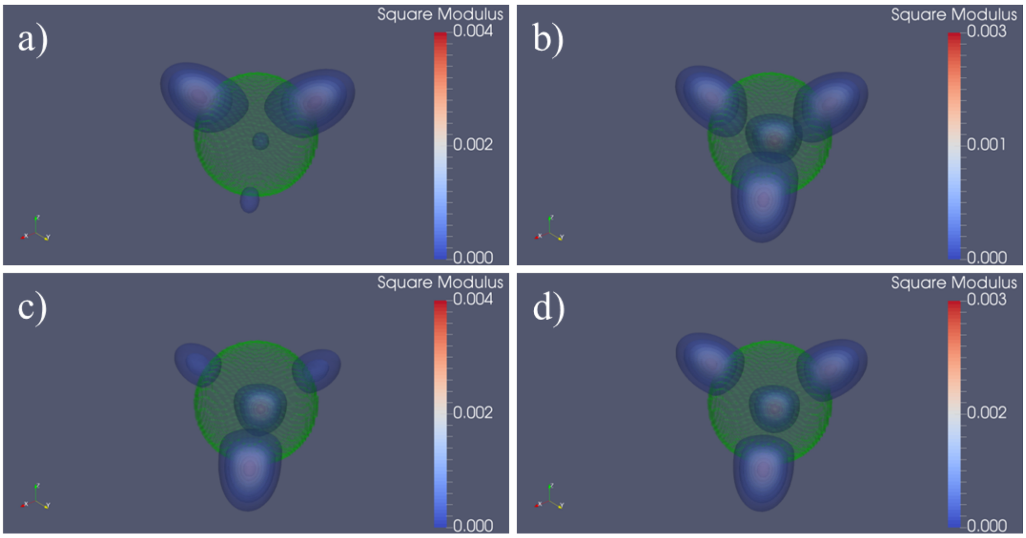

Figure 2.19.: Square modulus of the first eight hole wavefunctions for a spherical quantum dot. As the eigenstates are spin-degenerate, only the four unique profiles of the square modulus of the wavefunctions are shown. The shown isosurfaces correspond to the eigenstates a) 7 and 8, b) 5 and 6, c) 3 and 4, and d) 1 and 2.

The square moduli of the wavefunctions are of limited use when it comes to determination of the optical or Coulomb matrix elements which are required for simulations of the system dynamics within the density matrix formalism. The general procedure to calculate these matrix elements has been presented in sections 2.4 and 2.5. Since calculations of the matrix elements involve rather non-trivial steps, one does not gain too much new insight by examining the envelope wavefunctions of all spinors for all eigenstates. Picking the first p-like electron eigenstate and the hole eigenstate closes to the band gap as examples, figures 2.20 and 2.21 show the real part of the envelope wavefunctions for the individual spinor components. For the electron eigenstate one finds that the individual spinors are well localized inside the quantum dot with only minor extend into the surrounding matrix while for the selected hole eigenstate the spinors are mainly localized at the edge or outside of the quantum dot. Both results are consistent with the square moduli presented in figures 2.18 and 2.19.

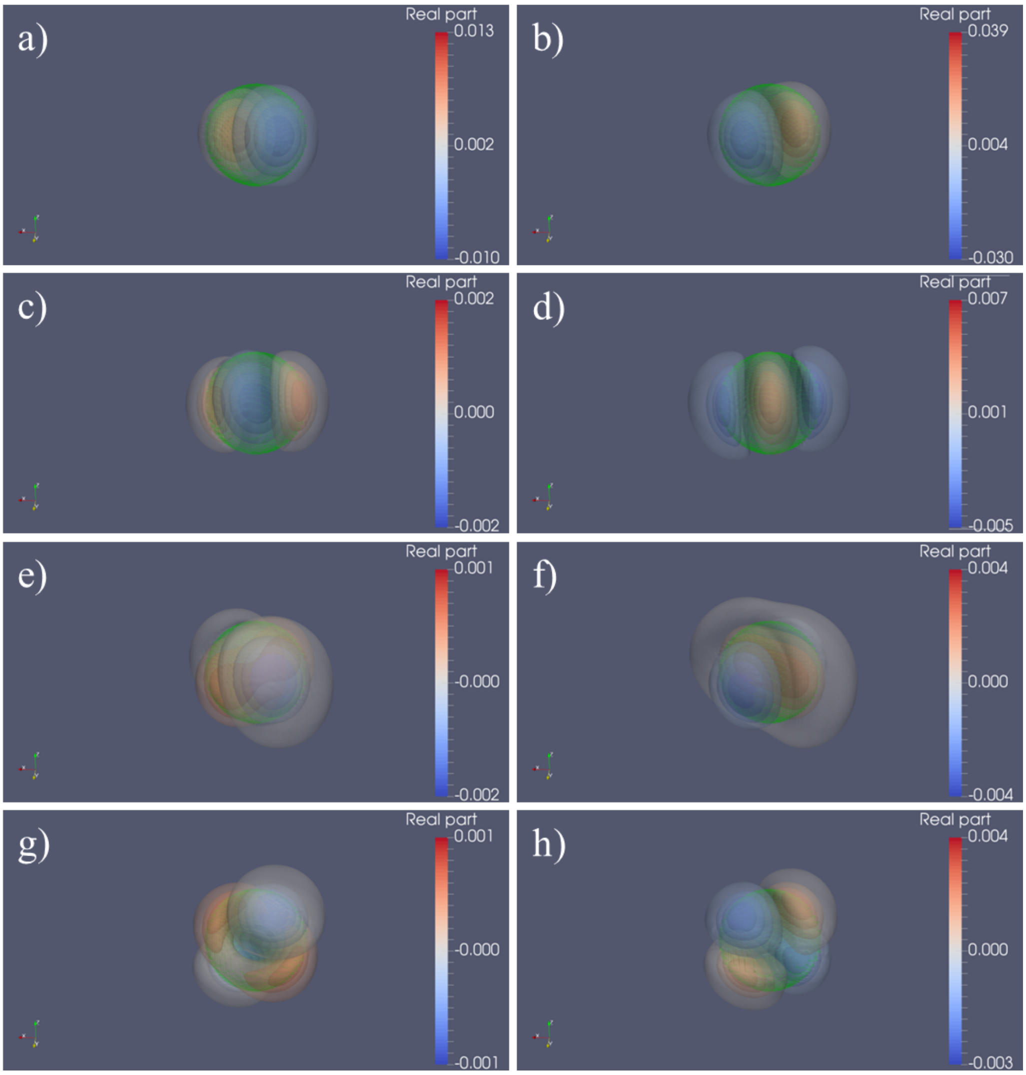

Figure 2.20.: Real parts of the envelope wavefunctions for the first p-like electron wavefunction of a spherical quantum dot. a) and b) show the real part of the S+ and S- envelope wavefunction respectively. Similarly c) and d) the X envelope wavefunction, e) and f) the Y envelope wavefunction, g) and h) the Z envelope wave function. A finite admixture of valence band states is visible, however, the amplitude is at least one order of magnitude smaller.

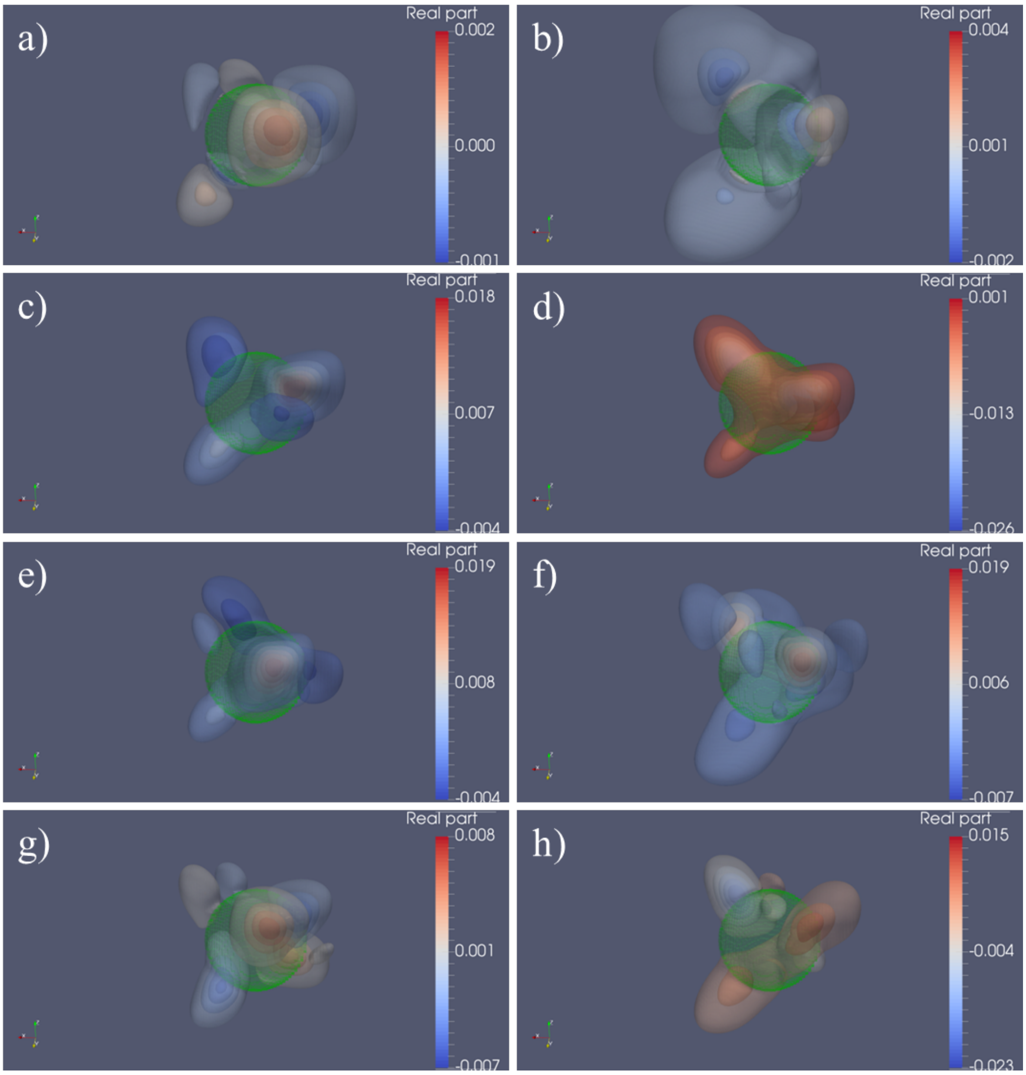

Figure 2.21.: Real parts of the envelope wavefunctions for the first hole wavefunction of a spherical quantum dot. a) and b) show the real part of the S+ and S- envelope wavefunction respectively. Similarly c) and d) the X envelope wavefunction, e) and f) the Y envelope wavefunction, g) and h) the Z envelope wave function.

Optical and Coulomb matrix elements

The optical matrix elements have been calculated using equations (2.51) and (2.56). As the dipole matrix elements scale inversely proportional to the energy difference between the involved states, one might get a wrong impression about the strength of intraband absorptions when exciting close to the band gap. To this end, here and in the following the optical matrix elements are substituted as follows:

$$\widetilde{\boldsymbol{\mu}}_{ij} = -i\left(\varepsilon_i - \varepsilon_j\right)\boldsymbol{\mu}_{ij} \tag{2.100}$$

Considering excitation with a plane wave propagating into positive z-direction, the following polarization vectors are defined:

$$\boldsymbol{\sigma}_+ = \frac{1}{\sqrt{2}}\left(1, i, 0\right)^T \tag{2.101}$$

$$\boldsymbol{\sigma}_- = \frac{1}{\sqrt{2}}\left(1, -i, 0\right)^T \tag{2.102}$$

$$\tag{2.103}$$

Defining $\left|\widetilde{\boldsymbol{\mu}}_{ij}\right|$ as the absolute value of the optical matrix element and $\left|\boldsymbol{\sigma}_\pm \cdot \widetilde{\boldsymbol{\mu}}_{ij}\right|$ as the projection on $\boldsymbol{\sigma}_\pm$ one obtains the graphs in figure 2.22 for the considered spherical quantum dot.

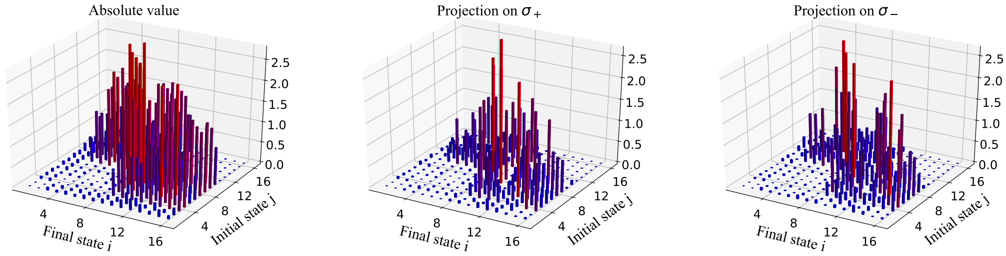

Figure 2.22.: Optical matrix elements for the considered spherical quantum dot. The matrix elements are measured in units of eÅ.

As can be seen, the substituted optical matrix elements are dominated by interband matrix elements while the intraband matrix elements are almost negligible. However, as the spherical quantum dot is considered as a rather unphysical system, the matrix elements will not be analyzed in further detail.

The Coulomb matrix elements have been determined using the PGF method described in 2.5 without additional screening. As already mentioned in that section, the theoretical number of Coulomb matrix elements considering a set of 16 states is 65536. Using simple symmetry relations this number can be reduced by a factor of four. Although this gives a significant reduction, the remaining number of matrix elements is still way to large for detailed analysis of all matrix elements. As examples, here and in the following, Coulomb matrix elements of the form V_{ijjl} will be presented with j corresponding to the first electron state or the first hole state at the respective band edge. Figure 2.23 shows the respective results for the considered spherical quantum dot. For both selected subsets of Coulomb matrix elements, the diagonal elements, i.e. $i = l$ are dominant. The off-diagonal elements are almost negligible.

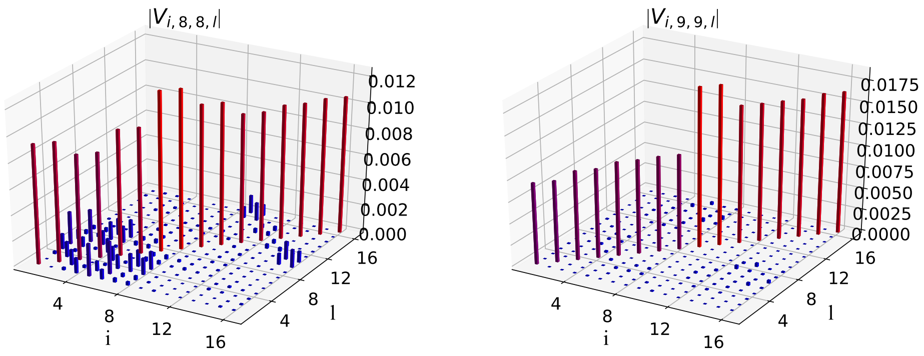

Figure 2.23.: Selected Coulomb matrix elements for the considered spherical quantum dot measured in eV.

2.6.2. Ellipsoidal Quantum Dot

The next considered system is an ellipsoidal semiconductor quantum dot as depicted in figure 2.24. Its diameter d is chosen to be $d = 14.6$ nm, its height is given by $h = 3.65$ nm. Considering symmetry, this system is still quite close to a spherical quantum dot in the sense that one just has to squeeze the spherical quantum dot along the z-axis in order to obtain the ellipsoidal one.

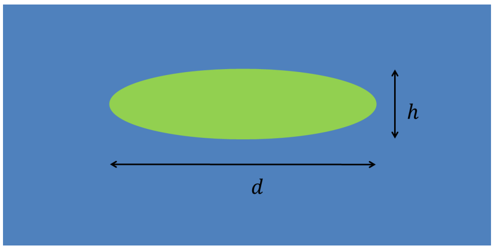

Figure 2.24.: Model of an ellipsoidal quantum dot. The diameter with respect to the semi-major axis is denoted as d, the diameter with respect to the semi-minor axis as h respectively. The blue region corresponds to the GaAs host matrix whereas the green region is filled with InAs.

To this end, again from pure symmetry considerations, one would expect a series of s- and p-like wavefunctions in the vicinity of the band gap. Here, however, one would not expect to find a p_z-like state in the vicinity of the band gap since the confinement length into z-direction is much smaller compared to the case of the spherical quantum dot.

Figure 2.25 shows the calculated eigenvalue spectrum for the eight electron and hole eigenstates closest to the band gap. As could be expected, for the electron one finds two degenerate eigenvalues right at the band gap followed by four degenerate eigenvalues and another pair of degenerate eigenvalues at a slightly larger energy.

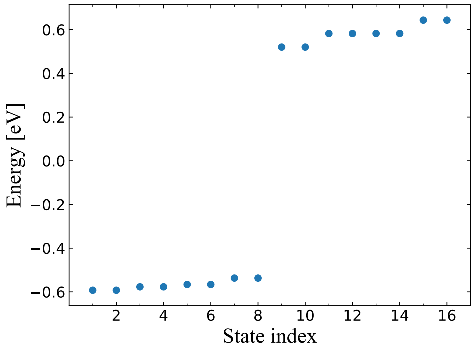

Figure 2.25.: Eigenvalue spectrum of an ellipsoidal quantum dot. For the calculations eight hole eigenstates and eight electron eigenstates have been taken into account.

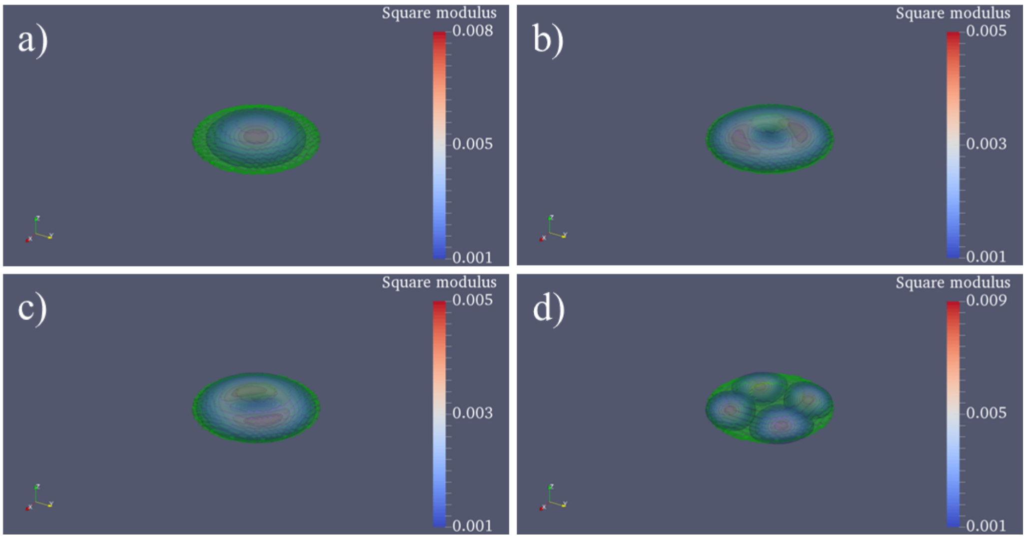

Figure 2.26.: Square modulus of the first eight electron wavefunctions for an ellipsoidal quantum dot. As the states are spin degenerate, only the four unique profiles are shown. The shown isosurfaces correspond to the state indices: a) 9 and 10, b) 11 and 12, c) 13 and 14, and d) 15 and 16.

Similar to the case of the spherical quantum dot the eigenvalues spectrum of the hole eigenstates can be divided into four pairs of degenerate eigenvalues. Based on this observation one might be tempted to assume that one finds similar results for the wave functions as well. Figures 2.26 and 2.27 show the square moduli of the calculated electron and hole eigenstates respectively.

For the electrons one observes a sequence of an s-like wavefunction followed by two wavefunctions given a linear combinations of p_x- and p_y-like wave functions. In this case, due to the smaller confinement length in z-direction, the p_z-like wavefunction is replaced by a wavefunction with a strong similarity to an atomic d-orbital. The term s-like may be misleading in this case as the shown square modulus of the first two electron eigenstates does not exhibit full radial symmetry. However, similar to an atomic s-orbital it has no internal nodes or node planes. Here and in the following such wavefunctions will be referred to as s-like, regardless of full radial symmetry.

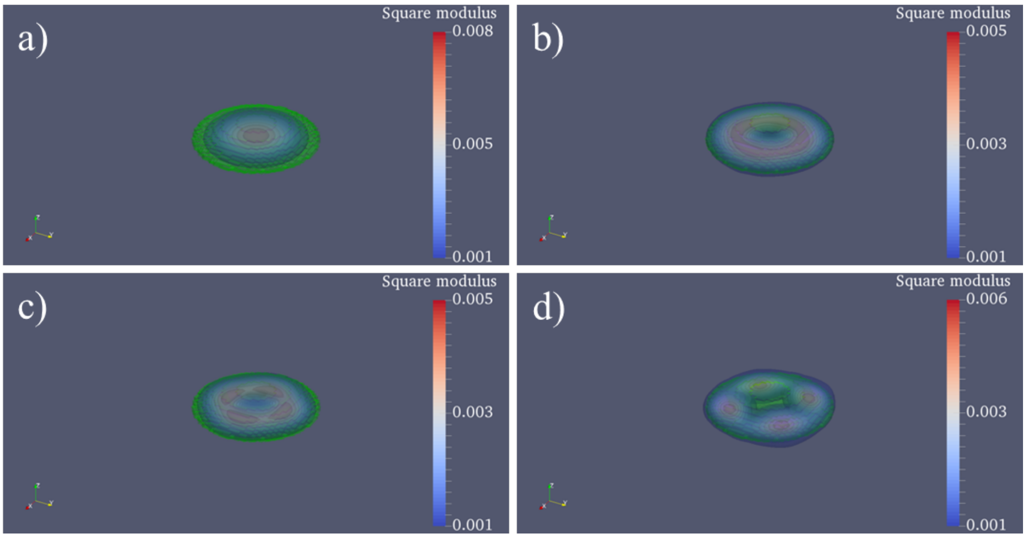

Figure 2.27.: Square modulus of the first eight hole wavefunctions for an ellipsoidal quantum dot. As the states are spin degenerate, only the four unique profiles are shown. The shown isosurfaces correspond to the state indices: a) 8 and 7, b) 6 and 5, c) 4 and 3, and d) 2 and 1.

Based on symmetry considerations, one would expect similar results for the hole eigenstates, but as in the case of the spherical quantum dot, the calculated square moduli differ from the expected results. In this case, however, the actual results are significantly closer to the expected ones than in the case of the spherical quantum dot. Possibly the first observation is that all hole eigenstates are well localized inside the quantum dot in contrast to the observation in case of the spherical quantum dot. The square modulus for the first two hole wavefunctions now shows the expected s-like symmetry. Similar to the electron eigenstates, the square modulus of the wavefunction for the 7th and 8th hole eigenstate shows a *d*-like symmetry.

For the intermediate eigenstates, expected *p*-like symmetry is not achieved. Figures 2.28 and 2.29 show the envelope wavefunctions for the spinors of the first *p*-like electron eigenstate and the first hole eigenstate respectively. Similar to the square moduli of the wavefunctions a much greater similarity of the results is observable.

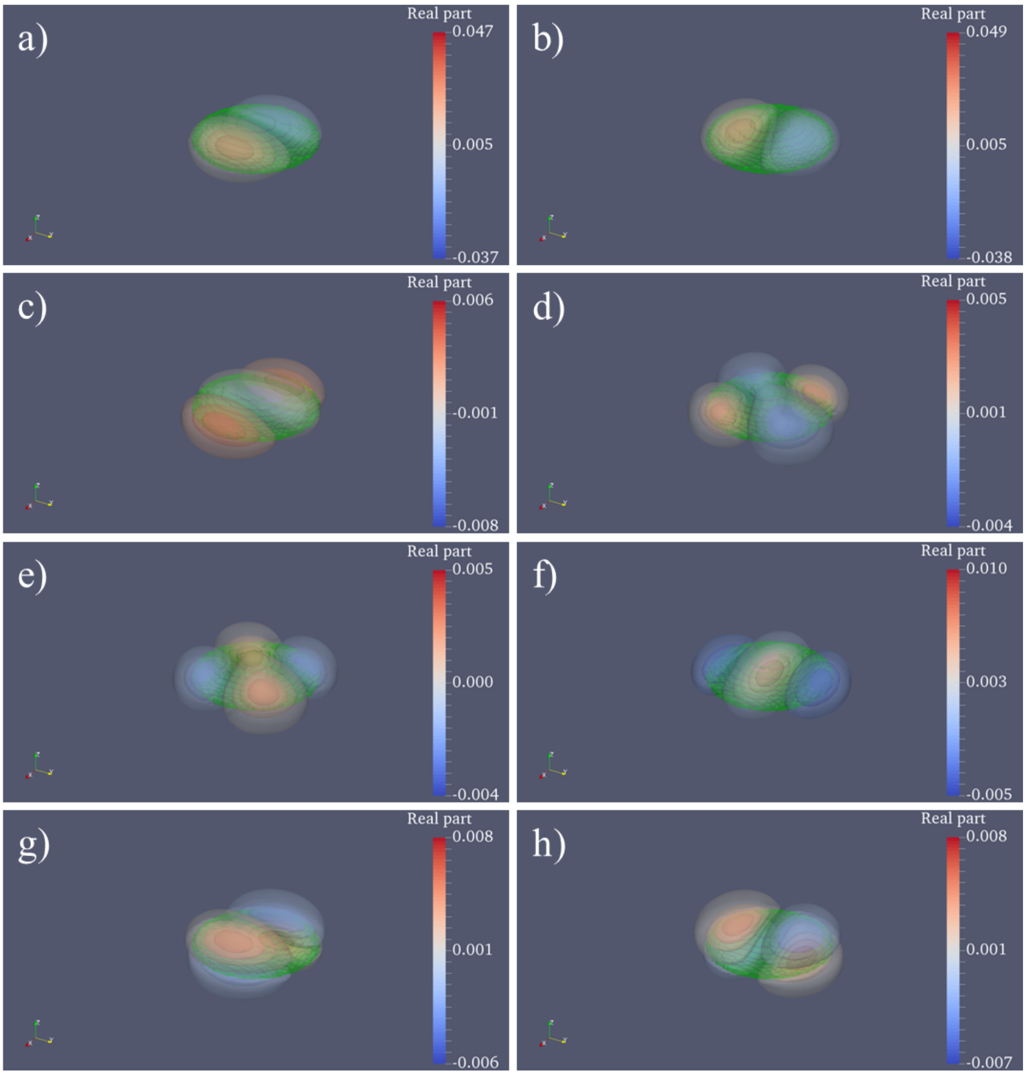

Figure 2.28.: Real parts of the envelope wavefunctions of the first *p*-like electron wavefunction of an ellipsoidal quantum dot. a) and b) show the real part of the S+ and S- envelope wavefunction respectively. Similarly c) and d) the X envelope wavefunction, e) and f) the Y envelope wavefunction, g) and h) the Z envelope wave function.

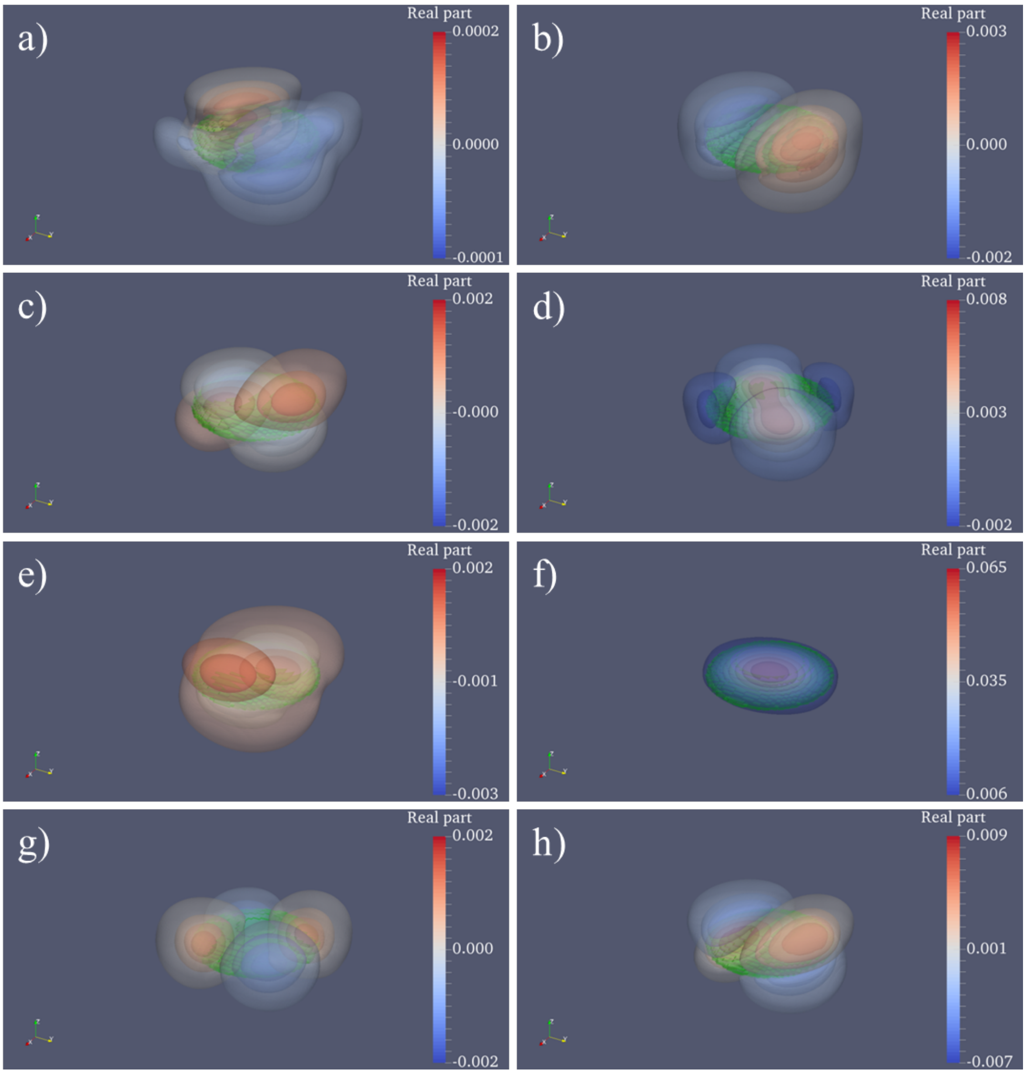

Figure 2.29.: Real parts of the envelope wavefunctions for the first hole wavefunction of an ellipsoidal quantum dot. a) and b) show the real part of the S+ and S- envelope wavefunction respectively. Similarly c) and d) the X envelope wavefunction, e) and f) the Y envelope wavefunction, g) and h) the Z envelope wave function.

Optical and Coulomb matrix elements

Figures 2.30 and 2.31 show the substituted optical matrix elements and selected Coulomb matrix elements for the considered ellipsoidal quantum dot. For the optical matrix elements one observes that fewer elements have a significant magnitude compared to the spherical quantum dot. As before, the matrix is dominated by interband elements with strongest magnitude in the direct vicinity of the band gap.

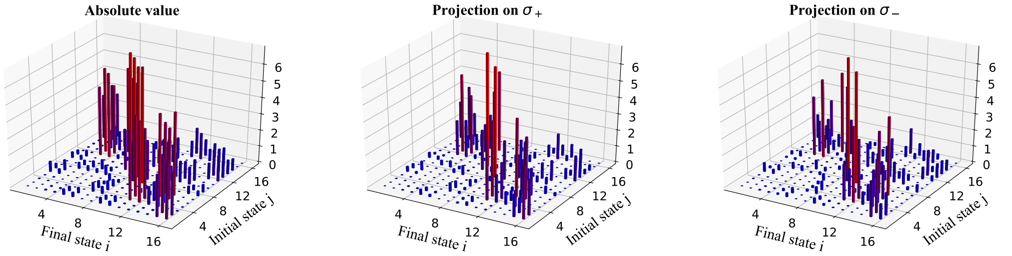

Figure 2.30.: Optical matrix elements for the considered ellipsoidal quantum dot measured in e$\mathring{A}$.

Qualitatively there is no difference between the two selected subsets of Coulomb matrix elements. And even from a quantitative point of view, the difference is not too big. As before, the off-diagonal matrix elements are negligible in both cases.

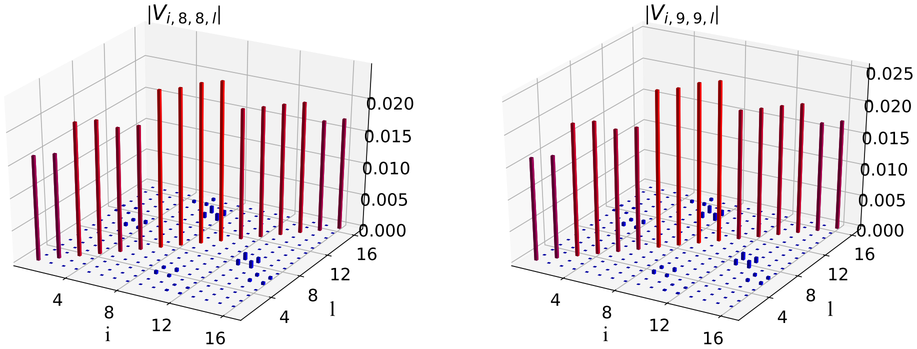

Figure 2.31.: Selected Coulomb matrix elements for the considered ellipsoidal quantum dot measured in eV.

2.6.3. Lens shaped Quantum Dot

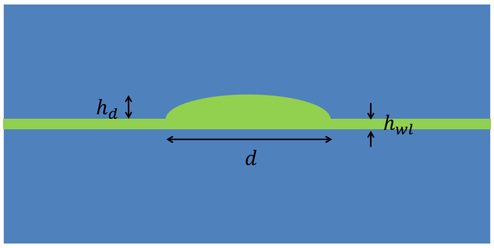

Figure 2.32.: Model of a lens shaped quantum dot modeled by a semiellipsoid on top of a thin layer. The base diameter of the quantum dot is denoted as d, the height of the quantum dot and the width of the wetting layer as h_d and h_{wl} respectively. The blue region marks the GaAs host matrix whereas the green regions correspond to InAs.

The considered lens shaped quantum dot has a base diameter of $d = 14.6$ nm and a height of $h = 2.9$ nm. The thickness of the wetting layer is considered as $h_{wl} = 1$ nm. Figure 2.33 shows the calculated eigenvalue spectrum. Qualitatively the calculated eigenvalue spectrum is quite similar to the spectrum of the ellipsoidal quantum dot considered in the last subsection.

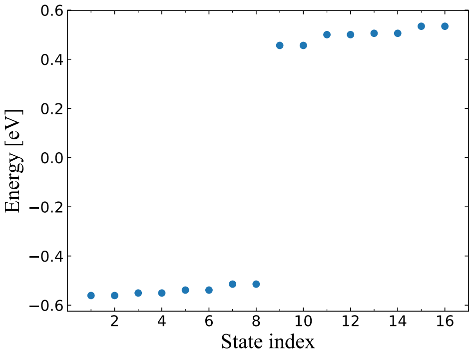

Figure 2.33.: Eigenvalue spectrum of a lens shaped quantum dot. For the calculations eight hole eigenstates and eight electron eigenstates have been taken into account.

As mentioned in the beginning of this section, the system of a lens shaped quantum dot will be utilized to show the impact of different parameters which all affect the strain in the system.

Influence of strain

The general influence of strain on the given lens shaped quantum dot is tremendous. Neglecting the strain effects at all, i.e. neglecting band alignments, state mixing, and piezo electric charges, no bound hole states could be determined. The reason becomes clear when looking at the bandedges in figure 2.34. While there is a sufficiently deep potential well for electrons, the potential well for holes is too shallow to allow localized hole states. This system could only be used as an electron trap.

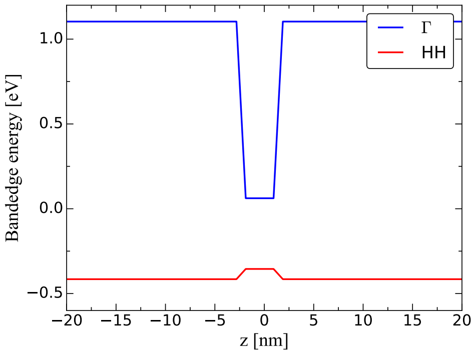

Figure 2.34.: Bandedge energies for the Γ and HH band along the growth direction neglecting strain effects.

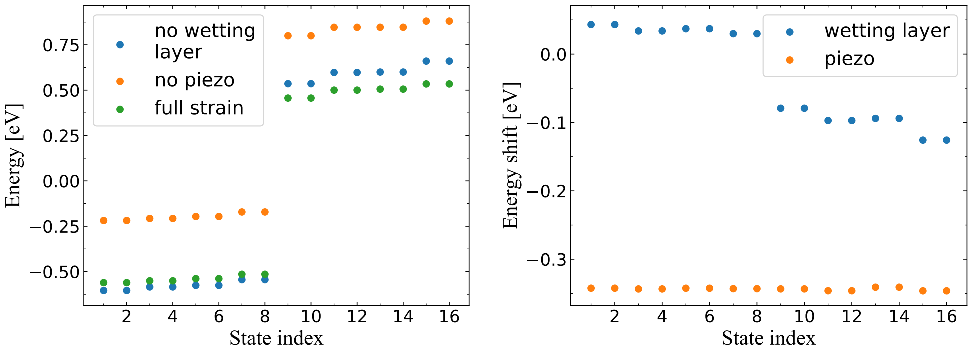

Figure 2.35.: Left: Calculated eigenvalue spectra for three quantum dot systems emphasizing different strain effects. Right: Spectral shifts due to presence of the wetting layer and piezo electric charges.

In addition to a complete neglection of strain effects, two different setups have been considered emphasizing different strain effects. Firstly, a quantum dot of the same size without its wetting layer. Comparing this system to the original one should show the impact of the strain field of the wetting layer. Secondly, the impact of piezo electric charges on the given system is shown by calculations for an identical quantum dot neglecting piezo electric charges. Figure 2.35 shows the calculated eigenvalue spectra in comparison. Comparing the spectrum of the original system to the one without wetting layer, one observes that the presence of the wetting layer results in a shift of the eigenvalues. This shift is, however, not uniform for all eigenvalues. For the hole eigenstates the energies are slightly shifted towards smaller negative energies with the states further apart from the band edge being shifted slightly stronger than the states in the vicinity of the band edge.

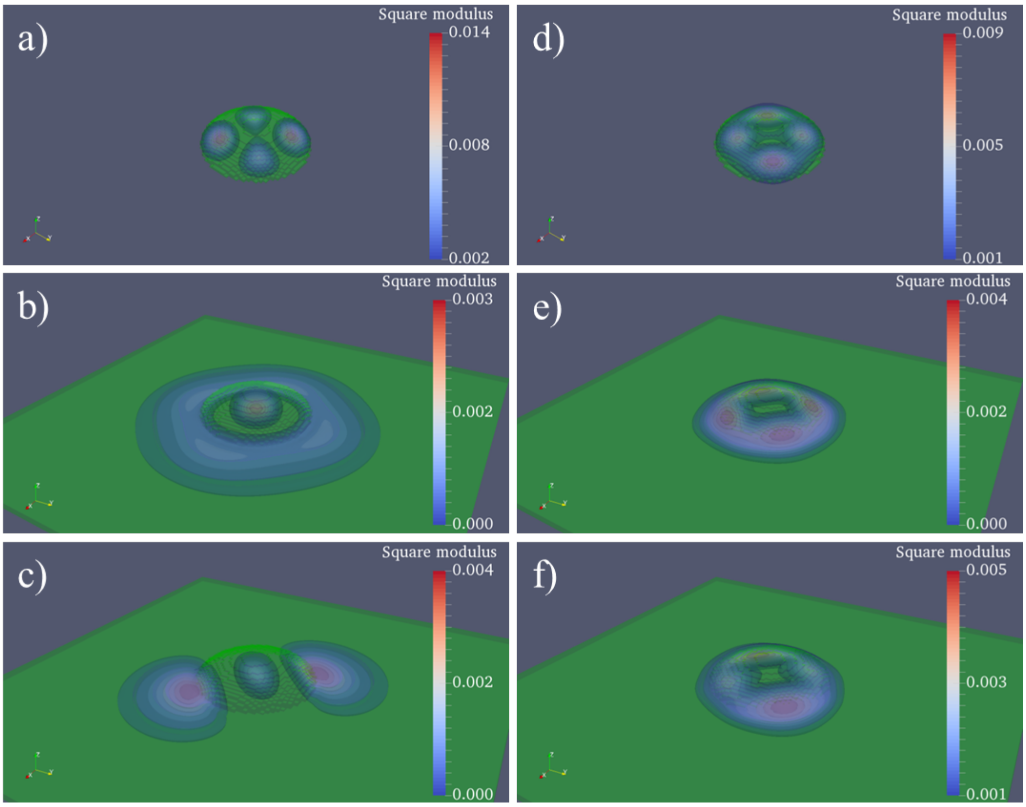

Figure 2.36.: Square modulus of selected wavefunctions depending on different strain effects. a) - c) The 7th electron eigenstate for a quantum dot without wetting layer, without piezo electric charges, and with both wetting layer and piezo electric charges. d)-f) Analogous plots for the 7th hole eigenstate.

For the electrons on the other hand, the eigenvalues are shifted towards smaller energies with a considerably larger shift than for the holes. Similar to the hole eigenvalues, electron eigenvalues further apart from the band edge are affected stronger than eigenvalues in the vicinity of the band edge. The band gap is reduced from about 1.07 eV without wetting layer to about 0.97 eV with wetting layer. Considering the effect of piezo electric charges, one observes an almost uniform shift of the complete spectrum towards lower energies with only minor fluctuations. This could be expected considering that these charges are included via an additional potential term which acts uniformly on all states.

The impact of the different strain effects is most visible for the eigenstates further apart from the band gap. To this end, figure 2.36 shows the square modulus of the electron and hole eigenstates with the largest distance to the band gap. For the electron state the observed differences are much more obvious than for the hole eigenstate. The overall shape of the hole eigenstate is not changed significantly. Presence of the wetting layer leads to a small extend of the wavefunction into the wetting layer and the piezo electric charges lead to a redistribution among the maxima of the square modulus. The electron eigenstate on the other hand shows a significant change in both shape and magnitude.

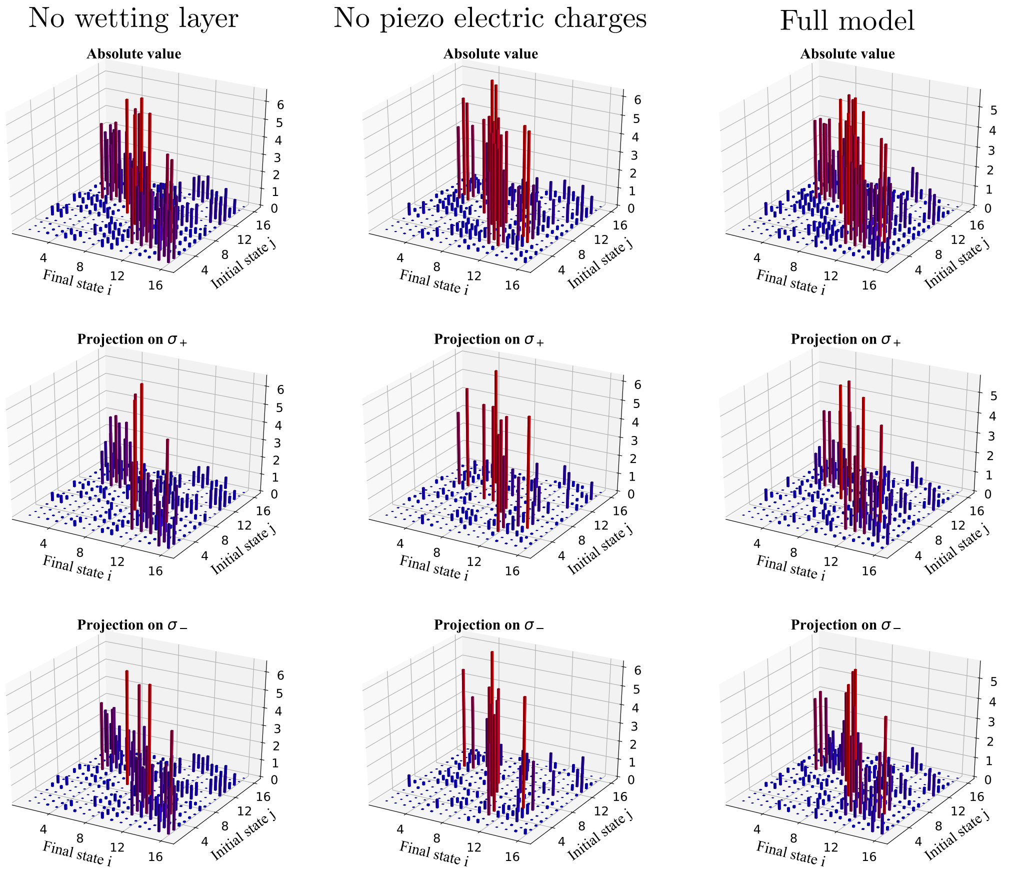

Figure 2.37.: Comparison of the optical matrix elements considering several strain effects. Left column: quantum dot without wetting layer. Middle column: quantum dot with wetting layer, but without piezo electric charges. Right column: quantum dot with wetting layer and piezo electric charges. The matrix elements are measured in units of eÅ.

Figure 2.37 shows the optical matrix elements for the considered systems in comparison. The optical matrix elements of the quantum dot without wetting layer look quite similar to those of the ellipsoidal quantum dot. Adding the wetting layer while removing piezo electric charges results in a reduction of matrix elements with significant magnitude. Adding the piezo electric charges again results in a sort of revival of matrix elements for both interband and intraband matrix elements.

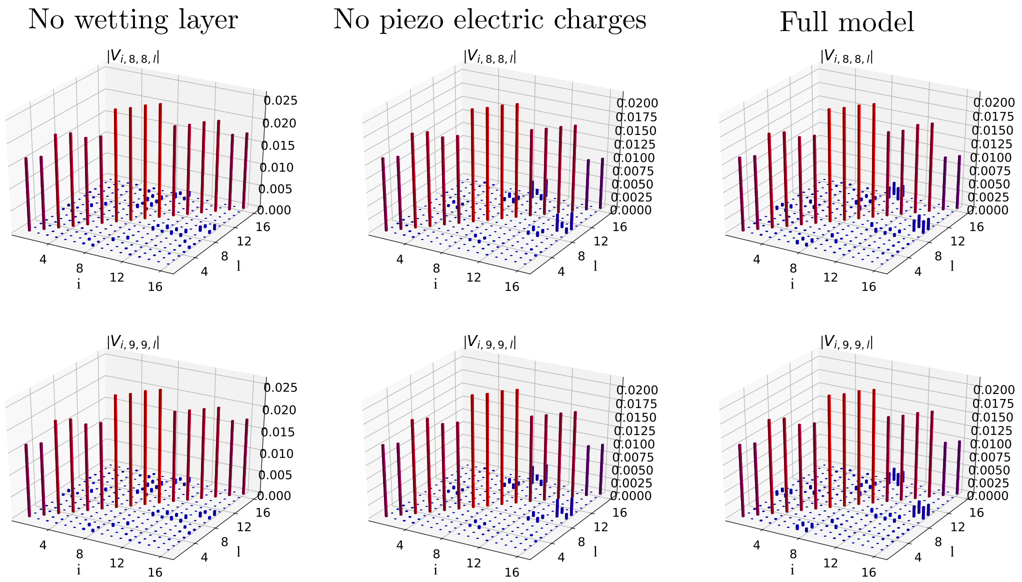

Figure 2.38.: Selected Coulomb matrix elements depending on different strain effects. The matrix elements are measured in units of eV.

Figure 2.38 shows selected subsets of the Coulomb matrix elements for the considered systems. Surprisingly, theses subsets do not change significantly when changing the conditions. The only obvious changes are a slight increase of off-diagonal elements and a reduction of the matrix elements with $i, l \in \{15, 16\}$.

Influence of material inhomogeneities

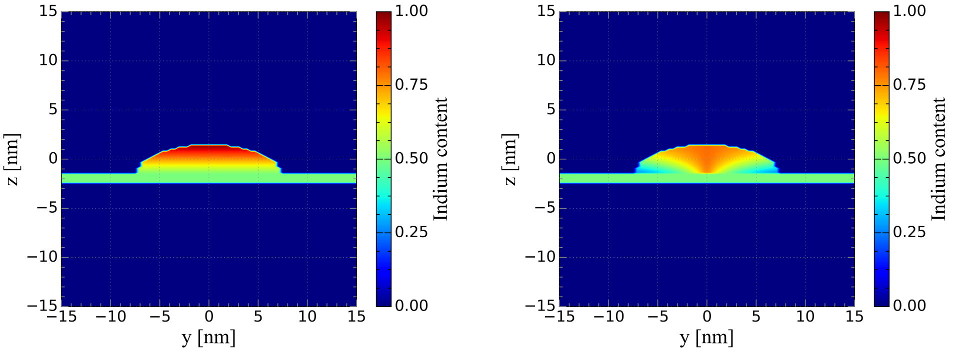

Figure 2.39.: Cut planes through the center of a lens shaped quantum dot with inhomogeneous Indium content. Left: Linear increase of the Indium content from the wetting layer to the top of the quantum dot. Right: Trumpet shaped profile of the Indium content.

A point which also affects strain in a given system are material inhomogeneities. Up until now the considered quantum dots were composed of 100% InAs. In reality, however, due to the growth conditions during the Stranski-Krastanov growth, one may be faced with substantial material inhomogeneities inside the quantum dots and the wetting layer [68, 69, 70, 71]. In essence, the impact of material inhomogeneities is twofold. Considering the ternary alloy $\mathrm{In}_x\mathrm{Ga}_{1-x}\mathrm{As}$ the lattice constant of the bulk material depends on the Indium content x. Accordingly, if one considers a quantum dot composed of this ternary, the strain in the system and in consequence both the electronic structure and distribution of piezo electric charge densities can change significantly if the Indium content shows a spatial dependence.

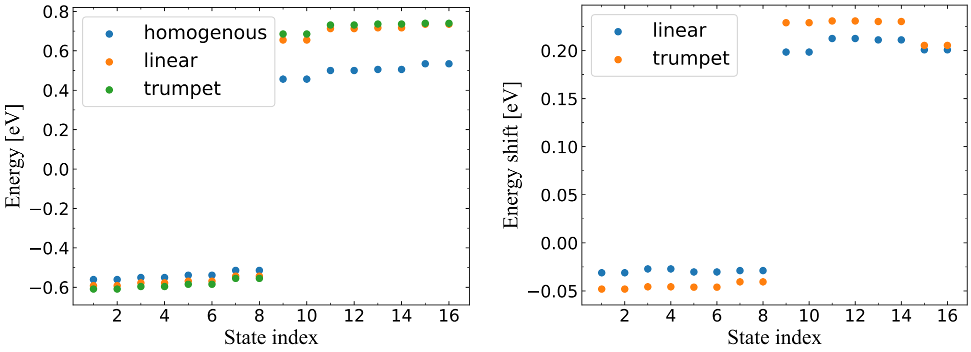

Figure 2.40.: Left: Calculated eigenvalue spectra of a quantum dot with three different material compositions. Right: Energy shifts compared to the homogeneous system.

On the left figure 2.40 shows the calculated eigenvalue spectra for the three considered material distributions in comparison. For both inhomogeneous compositions one observes that the electron states are much more affected by the material composition of the quantum dot than the hole states. The energy shift when switching from the homogeneous material composition to one of the inhomogeneous compositions is almost uniform for the hole eigenstates. For the electron on the other hand, the observed shift has a significantly larger magnitude and is clearly nonuniform.
Figure 2.41 shows the square modulus of the electron and hole eigenstates with largest distance to the band gap. Despite the significant shift of the eigenvalue, the overall shape of the electron state does not change too much when switching to one of the nonuniform material compositions. For the considered hole eigenstate, the only visible effect seems to be an increase of contrast between maxima and minima and a slightly stronger localization inside the quantum dot.

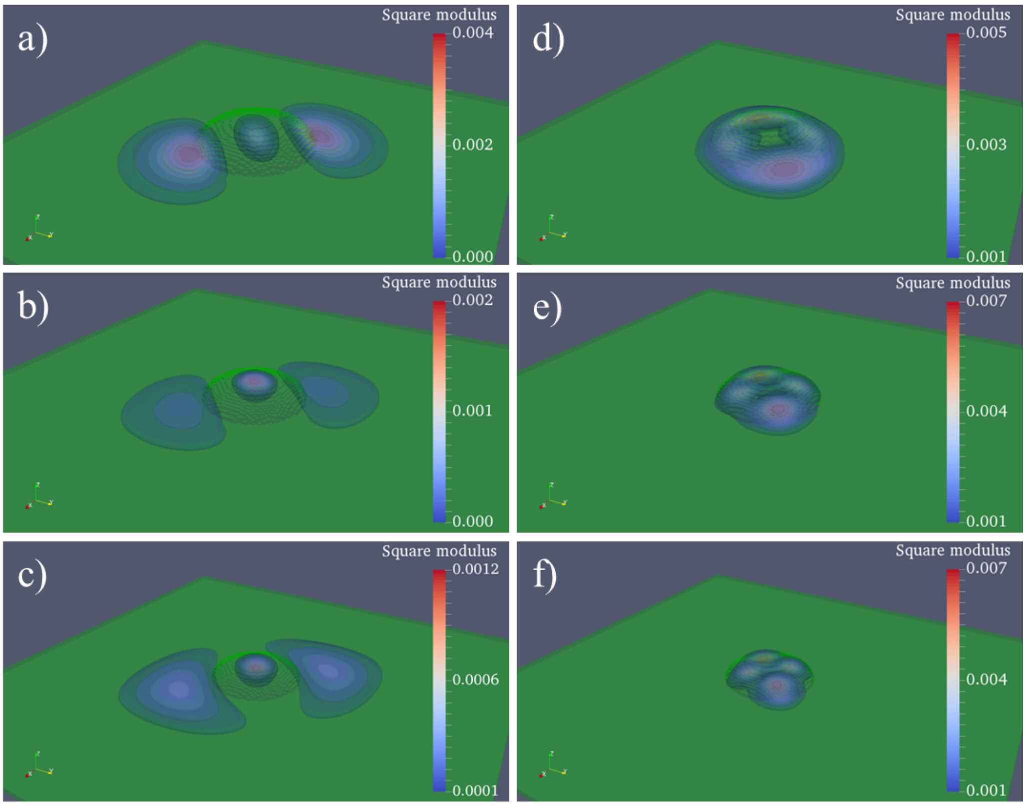

Figure 2.41.: Square modulus of selected wavefunctions depending on the material composition. a)-c) The 7th electron eigenstate for homogeneous, linearly increasing, and trumpet shaped Indium content. d)-f) Analogous plots for the 7th hole eigenstate.

Figures 2.42 and 2.43 show the Coulomb and optical matrix elements for the considered systems. For the Coulomb matrix elements the observation is quite similar to the one for the different direct strain effects. The most obvious effect is a decrease of the diagonal matrix elements with $i, l \geq 11$.

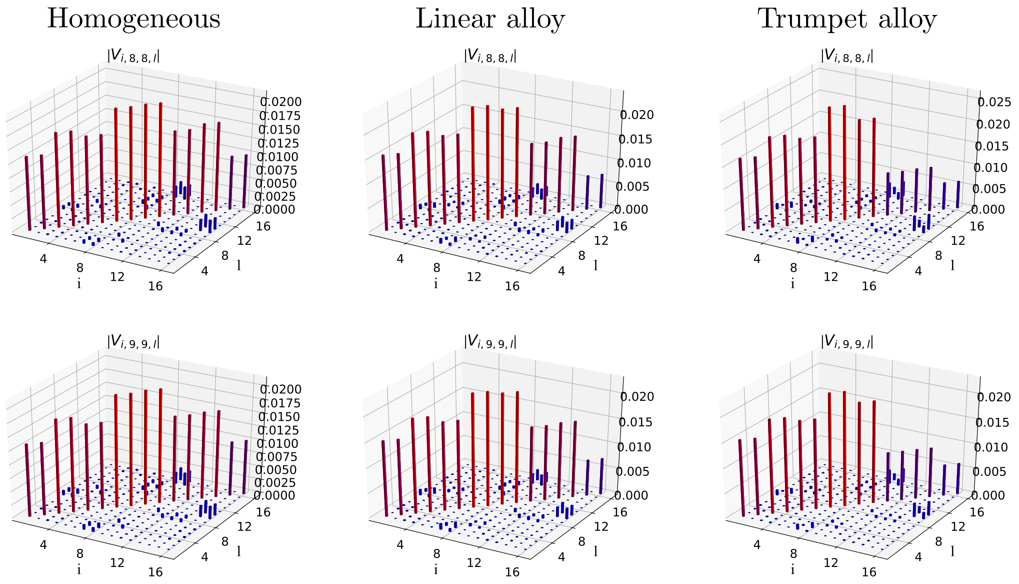

Figure 2.42.: Selected Coulomb matrix elements showing the impact of material composition. The matrix elements are measured in units of eV.

The optical matrix elements show a significant dependence on the underlying material composition of the quantum dot. Switching from a homogeneous to an inhomogeneous composition reduces the number of matrix elements with a significant magnitude. Considering the projection onto circular polarization, only two matrix elements in the vicinity of the band gap retain a significant magnitude for the trumpet shaped Indium content. This is consistent with the experimentally observed selection rules for absorption of light by a quantum dot.

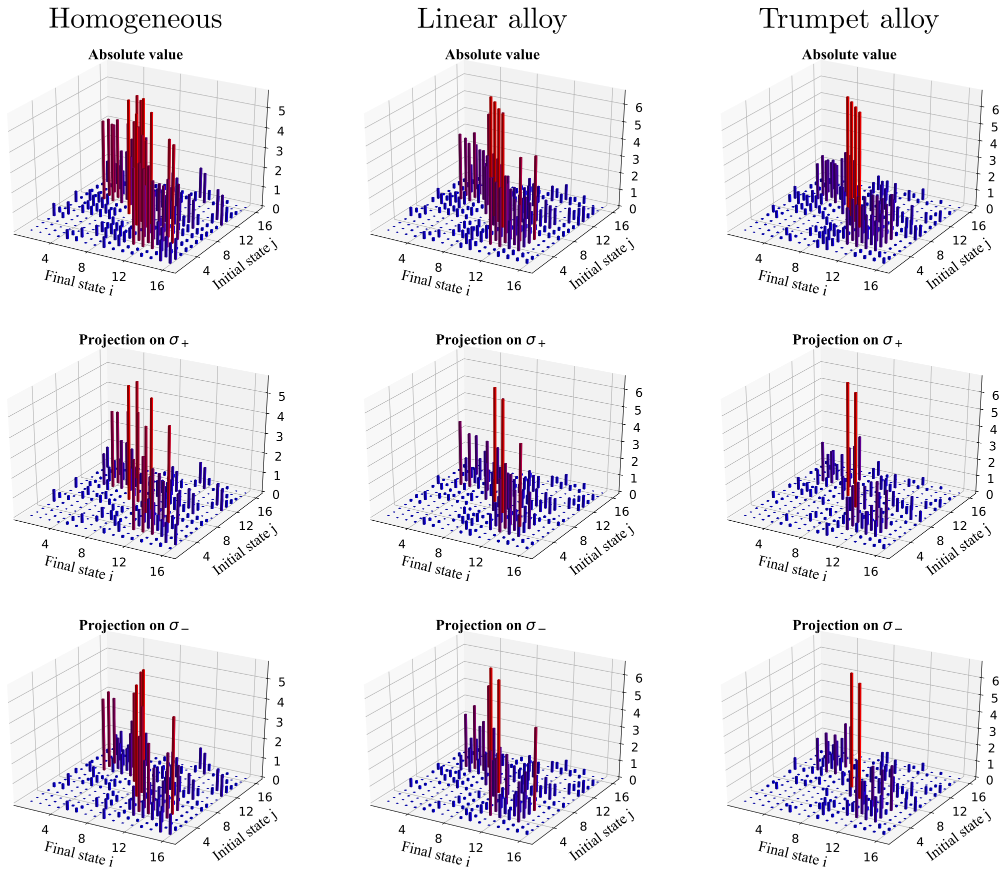

Figure 2.43.: Comparison of the optical matrix elements depending on the material composition. Left column: quantum dot without wetting layer. Middle column: quantum dot with wetting layer, but without piezo electric charges. Right column: quantum dot with wetting layer and piezo electric charges. The matrix elements are measured in units of eÅ.

2.6.4. Quantum dot molecules

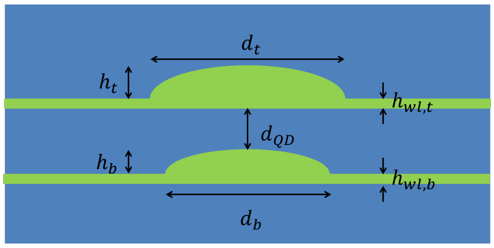

Figure 2.44.: Model of a semiconductor quantum dot molecule consisting of two vertically stacked quantum dots. The base diameter and height of the bottom dot are denoted as d_b and h_b. The same holds for the top dot with index b replaced by index t. The heights of the two wetting layers are denoted as $h_{wl,b}$ for the bottom dot and $h_{wl,t}$ for the top dot respectively.

Conceptually, the treatment of quantum dot molecules is not different from that of single quantum dots. In this work quantum dot molecules of two vertically stacked single quantum dots as depicted in figure 2.44 are considered. The size parameters and the distance between the individual dots have been chosen according to reported values by Scheibner *et al.* [26] as given in table 2.3.

Parameter	Value [nm]
d_b	14.6
h_b	2.9
d_t	17.9
h_t	2.1
d_{QD}	6.6

Table 2.3.: Calculation parameters for the quantum dot molecule.

Considering a sufficiently large distance between the two individual quantum dots, one would expect the eigenstates of the quantum dot molecule to be just the eigenstates of the individual quantum dots without any significant changes. Thus, one would for each of the quantum dots expect a series of s- and p-like, if enough states are calculated, maybe even d-like wavefunctions at least for the electrons.

From a simple point of view, if the distance between the dots is decreased, the eigenstates of the individual dots might start overlapping such that they do not build up an orthonormal set anymore. Any numerical method for diagonalization of the Hamiltonian will then find a set of potentially hybrid states. However, keeping in mind that the strain in the system depends on the material distribution, the situation gets more complicated since one has to consider perturbations of the original eigenstates other than simple overlaps.

In order to get a reasonable number of eigenstates for both quantum dots, calculations for the quantum dot molecule were performed considering each 16 electron hole eigenstates[5], giving a total of 32 eigenstates. The calculated eigenvalue spectrum is shown in figure 2.45. As in case of the other systems, the calculated eigenvalues come in pairs due to spin degeneracy.

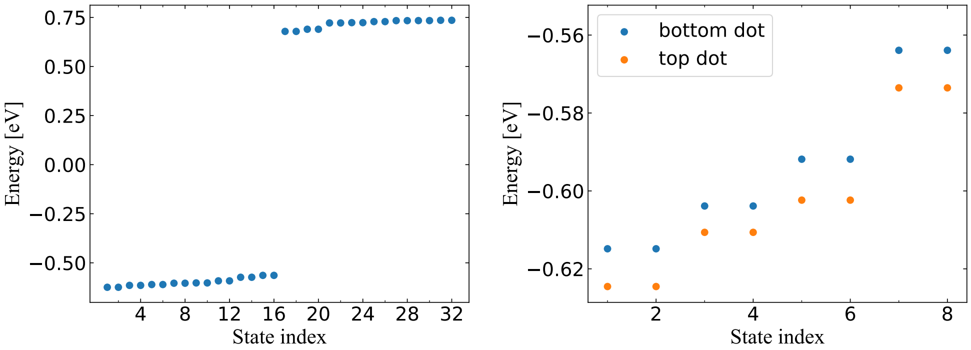

Figure 2.45.: Calculated eigenvalue spectrum of a quantum dot molecule considering each 16 electron and hole states.

Sorting the hole eigenstates according to their localization gives an energy spectrum as shown on the right in figure 2.45. Looking at the sorted spectra it seems somewhat surprising that the first p-like states of the top quantum dot (indices 5 and 6) and the second p-like states of the bottom quantum dot (indices 3 and 4) show now significant sign of hybridization despite the fact that they are energetically almost degenerate.

As already mentioned in a footnote, the calculated eigenstates are sorted in ascending order by their respective eigenvalue. This means that eigenstates with a similar eigenvalue are not necessarily located in the same quantum dot.

Figure 2.46 shows the square modulus of the eight hole wavefunctions corresponding to the eight eigenvalue pairs closes to the fundamental gap. The first thing one observes is that the hole wavefunctions are still well localized in the individual quantum dots. This is usually attributed to their higher effective mass. As can also be seen, obviously the degeneracy of the p-like hole states has been lifted, since the first p-like state in the bottom quantum dot is energetically followed by a p-like state in the upper quantum dot.

Apart from the energetic reordering, the calculated results for the hole eigenstates are not really surprising. Comparing just the spatial profile of the wavefunctions, the

---

[5] As the numeric solver inside nextnano just searches for the eigenvalues closest to the fundamental gap, it is not guaranteed, that one ends up with eigenstates equally distributed among both quantum dots

wavefunctions of the quantum dot molecule qualitatively correspond to what could be expected based on the result for a single lens shaped or ellipsoidal quantum dot.

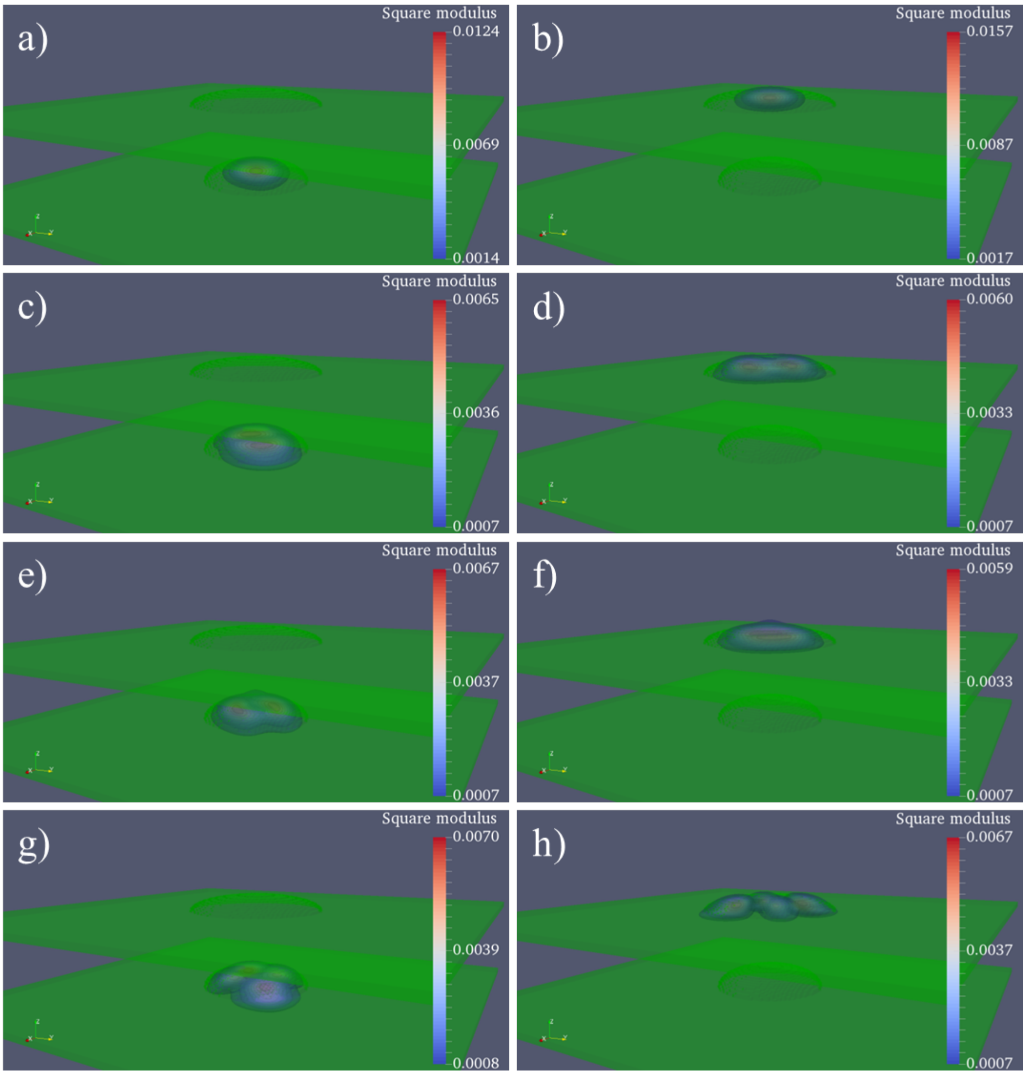

Figure 2.46.: Square modulus of the hole wavefunctions corresponding to the eight eigenvalue pairs closest to the fundamental gap. The shown square moduli correspond to a) eigenvalue 16, b) eigenvalue 14, c) eigenvalue 12, d) eigenvalue 10, e) eigenvalue 8, f) eigenvalue 6), g) eigenvalue 4, and h) eigenvalue 2.

For the electron wavefunctions one finds a quite complex picture. Figure 2.47 shows the square modulus for the electron eigenstates corresponding to the first four pairs of eigenvalues closest to the fundamental gap, similar to the picture already shown for the hole eigenstates. While the *s*-like state for the bottom quantum dot is still localized well inside the bottom quantum dot, the corresponding state of the top quantum dot already shows a finite extend into the bottom quantum dot. As this feature is not quite visible in figure 2.47 b), figure 2.48 shows a close-up image of the wavefunction.

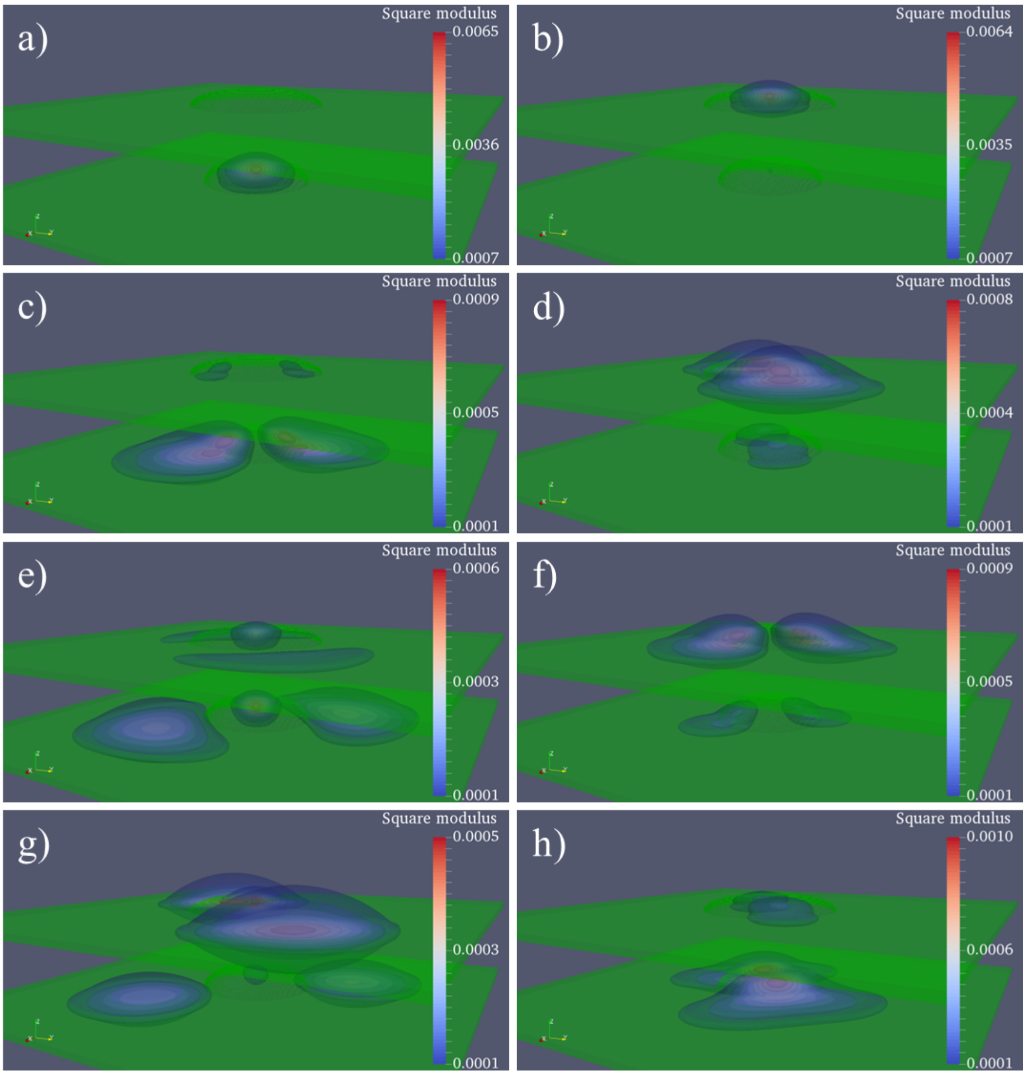

Figure 2.47.: Square modulus of the electron wavefunctions corresponding to the eight eigenvalue pairs closest to the fundamental gap. The shown square moduli correspond to a) eigenvalue 17, b) eigenvalue 19, c) eigenvalue 21, d) eigenvalue 23, e) eigenvalue 25, f) eigenvalue 27, g) eigenvalue 29, and h) eigenvalue 31.

The spatial hybridization becomes much more obvious for the electron states with higher energies as can be seen in figure 2.47 e)-h). The wavefunctions in question show a significant extent over both quantum dots. Based on this finding, it gets harder to tell whether a given optical resonance in the system stems from a spatially direct or indirect transition.

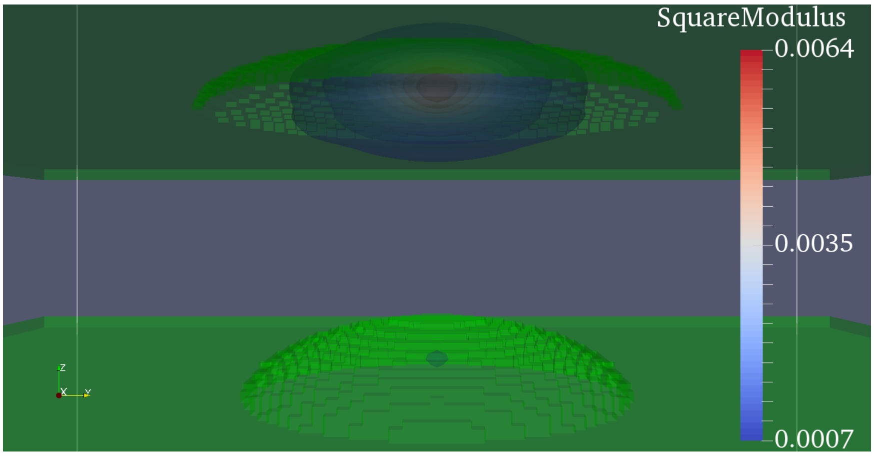

Figure 2.48.: Close-up image of the square modulus of the s-like eigenstate of the top quantum dot. The wavefunction shows a small, yet finite extend into the bottom quantum dot recognizable by the small blue dot in the lower half of the picture.

Optical and Coulomb matrix elements

The optical matrix elements and selected subsets of the Coulomb matrix elements are shown in figures 2.49 and 2.50. The optical matrix elements are dominated by a set of elements in the vicinity of the band gap.

Qualitatively the shown subsets of Coulomb matrix elements do not differ. One observes a slightly larger magnitude for $V_{i,16,16,l}$. For both subsets the off-diagonal elements for $i, l < 16$ are significantly smaller than for $i, l > 16$.

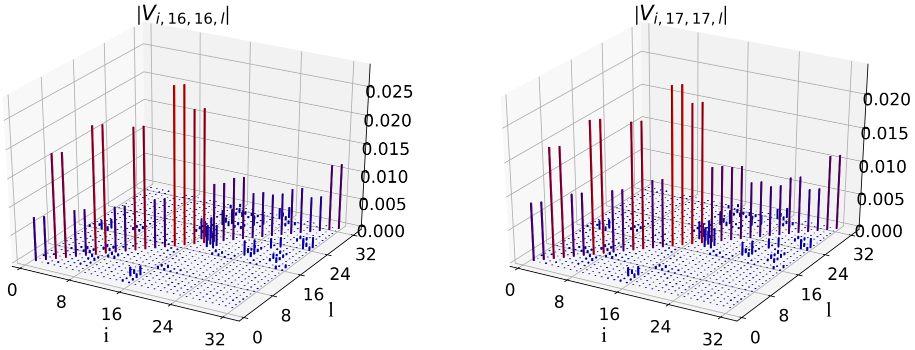

Figure 2.49.: Selected Coulomb matrix elements for the considered quantum dot molecule. The matrix elements are measured in units of eV.

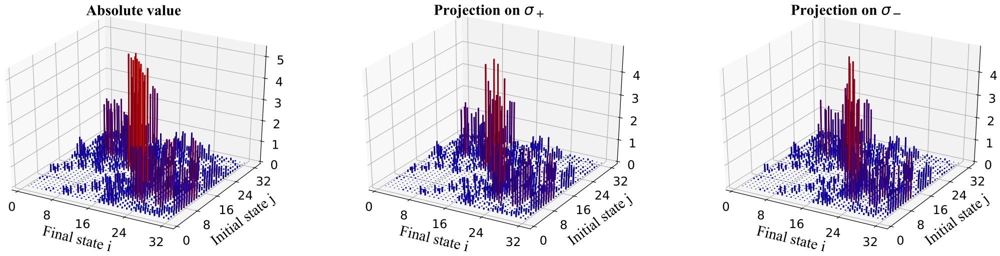

Figure 2.50.: Optical matrix elements for the considered quantum dot molecule. The matrix elements are measured in units of eÅ.

2.7. Modelling quantum dot systems embedded in a Schottky diode

Up to now, results for semiconductor quantum dots embedded in a homogeneous host matrix have been shown. In case of single quantum dot, the growth conditions can only affect the size and maybe to some extent the material composition of the resulting quantum dots. This means, manipulating the growth conditions, one only has static control over the electronic structure of the quantum dots. In order to investigate Stark shifts and charged exciton complexes in case of single quantum dots [72] as well as various charge configurations resulting from biexcitons in quantum dot molecules [73, 26, 74], these systems have been embedded in Schottky diode structures. These structures allow the manipulation of the quantum dot systems by static electric fields. Depending on the individual experiments, electric fields have been used to Stark tune the quantum dot resonances or control tunneling rates of charge carriers. Schottky diodes for quantum dot experiments usually consist of a highly doped back contact followed by an intrinsic semiconductor layer containing the quantum dot systems. Sometimes super lattice structures are grown on top of the quantum dot layer in order to prevent holes that have been generated optically inside the quantum dots from tunneling to the Schottky contact on top of the structure. The bandedge profile for an extremely simplified one dimensional model is shown in figure 2.51. By applying gate voltages at the Schottky contact (thought to be somewhere on the right) the tilt of the bandedges across the quantum dot region, and thus the tunneling barrier between the doped back contact and the quantum dots, may be manipulated. This allows controlled charging and uncharging of the quantum dots. In addition, applying static electric fields allows to operate the quantum dot in different regimes regarding the recombination of optically generated electrons. For example, applying sufficiently high bias voltages, the tunneling rates of electrons or holes may be tuned in such a way that the respective charge carrier tunnels out of the quantum dot at time scales considerably shorter than the radiative life time of a quantum dot exciton [75]. This regime is commonly called *photocurrent regime*. On the other hand, the applied voltage may also serve to suppress charge carrier tunneling, resulting in almost pure radiative recombination of excitons.

Considering the dimensions of real world Schottky diode structures, it is not hard to imagine that a 3D simulation of the complete device is unfeasible. Simple one dimensional simulations in effective mass approximation have been performed for the simplified structure shown in figure 2.51.

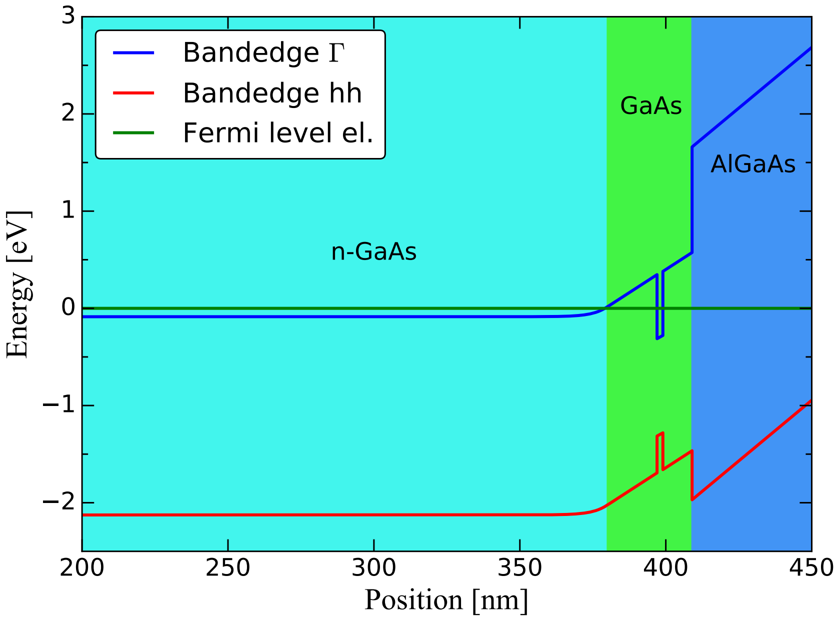

Figure 2.51.: One-dimensional modal of a quantum dot embedded in a Schottky diode structure. The potential well inside the GaAs region is supposed to correspond to an InAs region.

These calculation gave at least 20 electron states located in the back contact before the first electron state located inside the quantum dot. Considering that probably only a few of these states near the Fermi level play a significant role for charging experiments, a lot of computational resources would be wasted calculating irrelevant eigenstates. Of course, these states affect the dynamics of the system via Coulomb interaction. However, the occupation of these states will probably not change significantly during typical experiments, such that their presence is better modeled by some sort of interaction with a suitable charge carrier bath.

2.7.1. Quantum Dot Molecule

The quantum dot molecule presented in section 2.6.4 will serve as an example system since it nicely demonstrates several difficulties arising during the $\boldsymbol{k}\cdot\boldsymbol{p}$ calculations. The effect of an applied voltage at the Schottky diode on the quantum dot system may in first order be approximated by a constant electric field within the quantum dot region. In order to model such an electric field nextnano++ provides so called charge neutral contact regions which supply suitable boundary conditions for solution of Poisson's equation.

However, these contacts have to be used with care as well. As it turns out, presence of piezo electric charges within the simulation domain result in unphysical potential wells and barriers in the contact region. In order not to clutter the $\boldsymbol{k}\cdot\boldsymbol{p}$ results with unphysical states located at the artificial wells, one has to make the distance of the contacts from the region of interest sufficiently large. Luckily one does not have to extend the quantum region such that the time for the actual $\boldsymbol{k}\cdot\boldsymbol{p}$ solution does not scale dramatically.

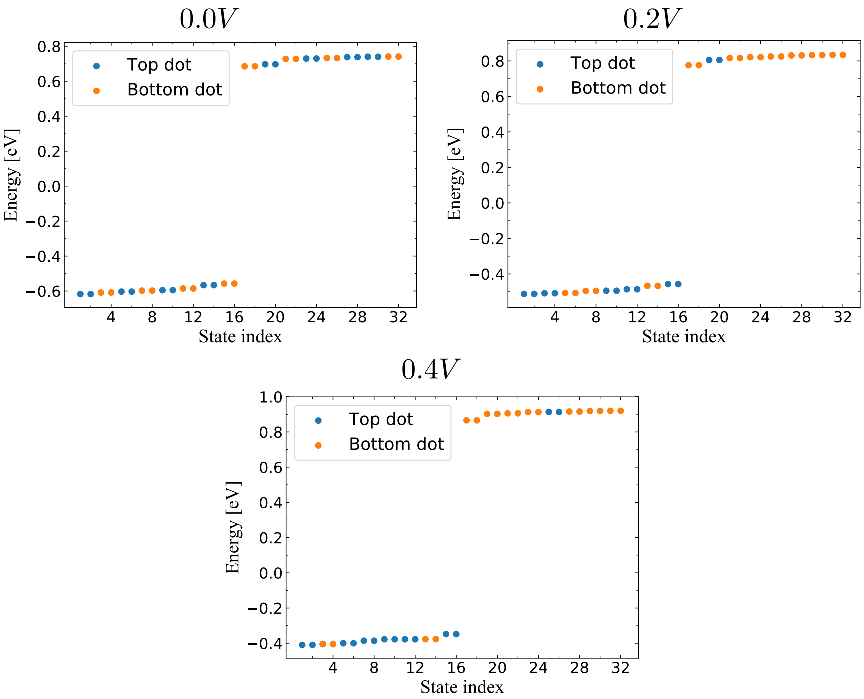

Figure 2.52.: Calculated eigenvalue spectra of a quantum dot molecule at different applied voltages.

Figure 2.52 shows the calculated eigenvalue spectra of the considered quantum dot molecule at several potential differences across the simulation space. In order to get a better feeling for the respective potential landscape, figure 2.53 shows the band edges of the Γ conduction band and the heavy hole valence band for an applied potential difference of 0.4 V. As can be seen, although the applied potential difference seems quite high, the tilt of the band edges stays at a reasonable level.

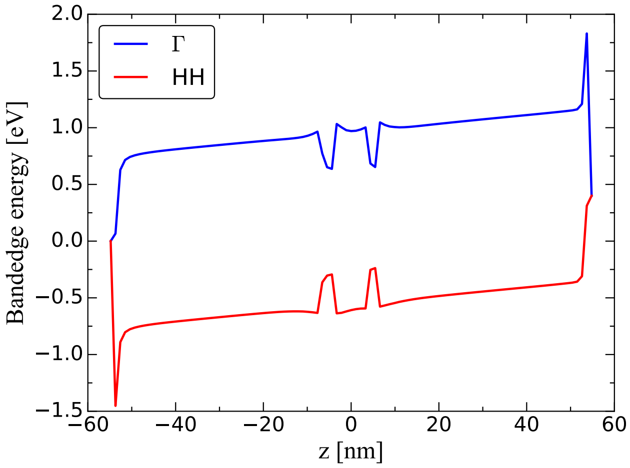

Figure 2.53.: Band edges of the Γ conduction band and the heavy hole valence band evaluated on a line through the center of the stacked quantum dots.

Coming back to the eigenvalue spectra in figure 2.52 one observes another difficulty which has already been mentioned. At a potential difference of 0.0 V across the simulation domain, the calculated eigenstates are evenly distributed among the two quantum dots with 8 electron and 8 hole eigenstates per dot. Considering absorption simulations within the density matrix formalism, this might serve as a suitable basis set. Turning up the potential difference, the situation changes significantly. Even at the lower of the two applied potential differences, the eigenvalue solver delivers only a single electron state in the top dot among the 16 calculated electron states. At the same time only six of the 16 calculated hole eigenstates are located in the bottom quantum dot. In order to spot the states which were present in the setup with 0 V applied potential difference one would have to significantly increase the number of calculated eigenstates and therefore the numerical effort. Although a direct comparison does not make too much sense since one is dealing with different sets of eigenstates, figures 2.54 and 2.55 show the optical matrix elements and selected subsets of the Coulomb matrix elements for the at the different applied potential differences.

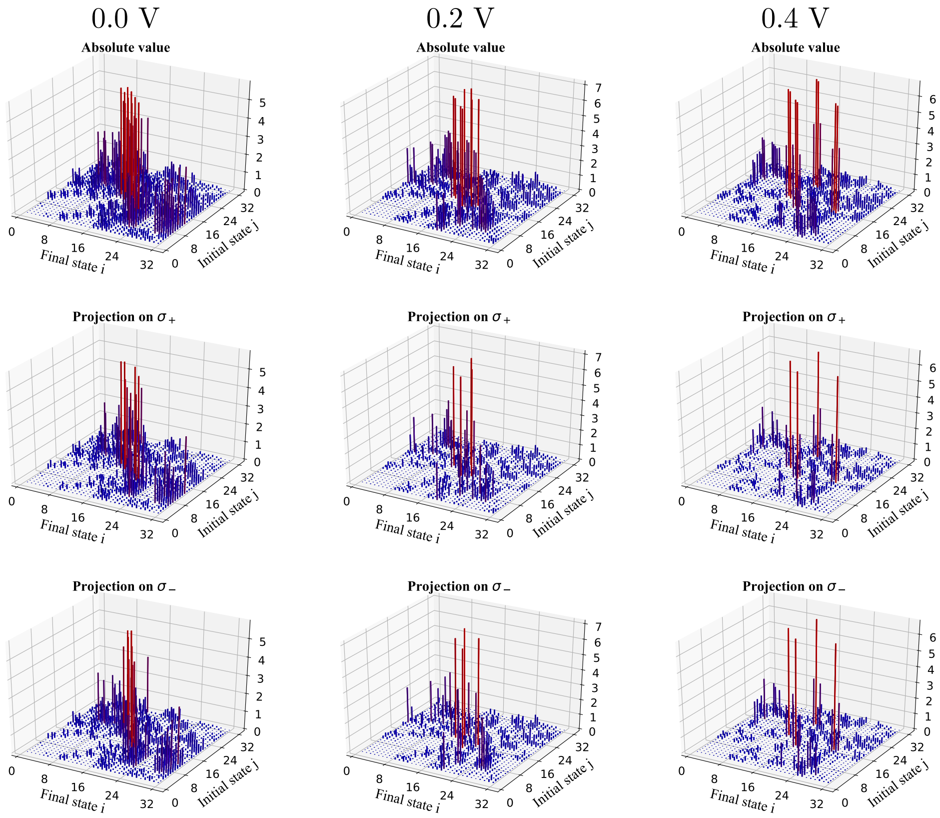

Figure 2.54.: Optical matrix elements, measured in units of eÅ, for the considered quantum dot molecule at different applied potential differences.

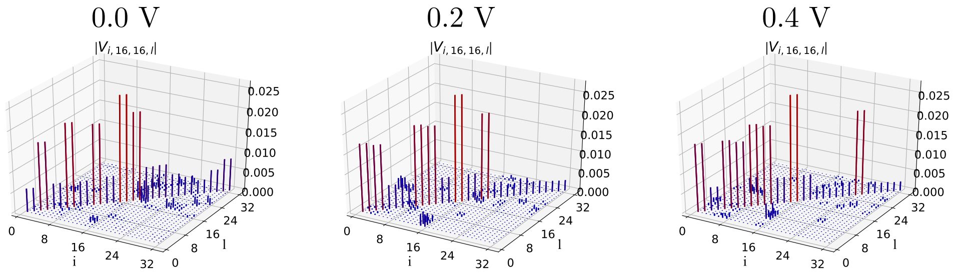

Figure 2.55.: Selected subsets of the Coulomb matrix elements, measured in eV, for the considered quantum dot molecule at different potential differences.

Considering the presented problems and the computational effort for the solution at a single applied potential difference, calculating a consistent set of optical and Coulomb matrix elements for a quasi continuous set of potential differences is considered unfeasible.

3. Modeling the dynamics of Quantum Dots within density matrix formalism

3.1. Equations of motion for a general FLS

The density matrix formalism for FLSs is well known in literature and has already found its way into textbooks governing the dynamics of atomic systems [76] as well as semiconductor nanostructures under optical excitation [77, 47]. A general FLS may be considered as given in figure 3.1. There is a finite set of single particle eigenstates with given eigenvalues. As has been shown earlier, one does not have to make any assumption on the exact localization of the corresponding single particle wave functions since this information will be implicitly contained in the respective coupling elements between the individual states.

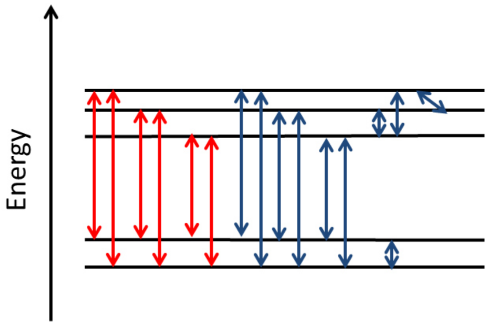

Figure 3.1.: Sketch of a general FLS. The red arrows indicate possible couplings between individual eigenstates via light-matter interaction whereas the blue arrows indicate couplings via Coulomb interaction.

At the moment, only three assumptions are made:

1. the set of eigenstates is discrete, yet allowing for degenerate eigenstates
2. the real system is considered small compared to the wave length of the exciting electric field
3. there is an energy gap between initially populated and initially empty eigenstates

The latter assumption is not really needed for the derivation of the equations of motion, but is required if one wants to model absorption spectra of semiconductor nanostructures in their ground state. The second assumption on the other hand, is needed to justify the use of an electric field which varies over time only. Considering systems with geometrical extensions comparable to or larger than the wave length of the exciting field, one would have to take retardation effects into account.

The optical couplings depicted in figure 3.1 are restricted to so-called interband couplings. Depending on the eigenstates of the underlying system, finite intraband couplings are of course possible. In this work, the energy gap between the initially populated states and the initially unpopulated states is considered to be significantly larger than the energy gap between two initially populated or unpopulated states. If one then considers optical excitation at frequencies close to the fundamental gap, intraband absorption should play only a minor role since the respective transition is driven strongly off-resonant.

Using second quantization formulation where $a_i^\dagger$ creates an electron in state i and a_i destroys an electron in state i the total Hamiltonian of the FLS interacting with a semi-classical light field may be written as

$$\hat{H} = \hat{H}_0 + \hat{H}_{lm} + \hat{H}_C \tag{3.1}$$

$$\hat{H}_0 = \sum_i \varepsilon_i a_i^\dagger a_i \tag{3.2}$$

$$\hat{H}_{lm} = -\frac{1}{2}\boldsymbol{E}(t) \cdot \sum_{i \neq j} \boldsymbol{\mu}_{ij} a_i^\dagger a_j + \boldsymbol{\mu}_{ij}^* a_j^\dagger a_i \tag{3.3}$$

$$\hat{H}_C = \frac{1}{2} \sum_{i,j,k,l} V_{ijkl} a_i^\dagger a_j^\dagger a_k a_l \tag{3.4}$$

where

$$\omega_{ij} = \frac{\varepsilon_i - \varepsilon_j}{\hbar}$$

Looking into literature, people often make a distinction between operators acting on initially populated states and operators acting on initially empty states even when they are not using the electron-hole picture. While this may be helpful for determining the exact nature of a given operator product of two or more operators, it is somewhat inconvenient for a general derivation of equations of motion for a given system since one quickly deals with an increasing number of different product patterns when deriving the equations of motion. Using the fermionic anticommutation rules for the creation and annihilation operators

$$\left[a_i, a_j^\dagger\right]_+ = \delta_{ij} \tag{3.5}$$

$$\left[a_i^{(\dagger)}, a_j^{(\dagger)}\right]_+ = 0 \tag{3.6}$$

the temporal dynamics of the system can be described by the Heisenberg equations of motion

$$\frac{d}{dt}\hat{O} = -\frac{i}{\hbar}\left[\hat{O}, \hat{H}\right] + \frac{\partial}{\partial t}\hat{O} \tag{3.7}$$

where $\hat{O}$ may be an arbitrary, yet meaningful, operator. If the operator $\hat{O}$ is not explicitly time dependent, the last term on the right hand side vanishes. Taking the expectation value on both sides one obtains

$$\frac{d}{dt}\left\langle \hat{O} \right\rangle = -\frac{i}{\hbar}\left\langle \left[\hat{O}, \hat{H}\right] \right\rangle \tag{3.8}$$

As the commutator is a linear operator the derivation of the equations of motion can be carried out one at a time for each part of the total Hamiltonian.
Starting with the general operator product $a_i^\dagger a_j$ one finds

$$\left.\frac{d}{dt}\left\langle a_i^\dagger a_j \right\rangle\right|_0 = i\omega_{ij}\left\langle a_i^\dagger a_j \right\rangle \tag{3.9}$$

$$\left.\frac{d}{dt}\left\langle a_i^\dagger a_j \right\rangle\right|_{lm} = \frac{i}{\hbar}\boldsymbol{E} \cdot \sum_k \boldsymbol{\mu}_{jk} a_i^\dagger a_k - \boldsymbol{\mu}_{ki} a_k^\dagger a_j \tag{3.10}$$

$$\begin{aligned}\left.\frac{d}{dt}\left\langle a_i^\dagger a_j \right\rangle\right|_C = &\frac{1}{2}\sum_{lmn} V_{jlmn} a_i^\dagger a_l^\dagger a_m a_n + \frac{1}{2}\sum_{kmn} V_{kjmn} a_k^\dagger a_i^\dagger a_m a_n \\ &- \frac{1}{2}\sum_{kln} V_{klin} a_k^\dagger a_l^\dagger a_j a_n - \frac{1}{2}\sum_{klm} V_{klmi} a_k^\dagger a_l^\dagger a_m a_j.\end{aligned} \tag{3.11}$$

Equation (3.11) shows the onset of the well-known many body hierarchy. Evaluation of the equation of motion for an operator product consisting of $2N$ operators requires knowledge of the expectation value of operator products consisting of $2N + 2$ operators. When considering bulk materials one is dealing with a quasi infinite number of electrons in the system and an infinite hierarchy of equations[1]. However, when considering a system with a finite, manageable number of electrons, there is a natural truncation of the many body hierarchy since any operator product which contains more annihilation operators than electrons in the system has to evaluate to zero when acting on the many particle wave function.

---

[1] Of course the number of electrons is not really infinite, but way too large to treat all electrons explicitly

Throughout this thesis a finite number of electrons will be assumed such that the many body hierarchy can be truncated without applying a correlation expansion [78] or a perturbation expansion in powers of the electric field [79].
Although the derivation of the equations of motion for the higher order operator products is, at least in principle, straight forward and requires only simple operator algebra, it gets quite cumbersome and error prone with increasing number of factors in the operator products. To this end as part of this thesis, a program was developed on top of the SymPy library [80] which is able do derive symbolic equations of motion for the required operator products given a system containing a fixed number of electrons. In a second stage the symbolic equations are used to generate C++ code for numerical solution of the equations of motion[2].
In order to keep the notation cleaner, the following abbreviations are used:

$$\hat{O}_{\bar{i}_N} = a^\dagger_{i_1} a^\dagger_{i_2} \cdots a^\dagger_{i_{N/2}} a_{i_{N/2+1}} \cdots a_{i_N} \tag{3.12}$$

$$\omega_{\bar{i}_N} = \frac{\varepsilon_{i_1} + \cdots + \varepsilon_{i_{N/2}} - \varepsilon_{i_{N/2+1}} - \cdots - \varepsilon_{i_N}}{\hbar} \tag{3.13}$$

Using this notation and adding a phenomenological damping term the equations of motion take the following general form

$$\frac{d}{dt}\left\langle \hat{O}_{\bar{i}_N} \right\rangle \bigg|_0 = i\omega_{\bar{i}_N} \left\langle \hat{O}_{\bar{i}_N} \right\rangle \tag{3.14}$$

$$\frac{d}{dt}\left\langle \hat{O}_{\bar{i}_N} \right\rangle \bigg|_{lm} = \sum_{\bar{j}_N} g_{lm,\bar{j}_N}(t) \left\langle \hat{O}_{\bar{j}_N} \right\rangle \tag{3.15}$$

$$\frac{d}{dt}\left\langle \hat{O}_{\bar{i}_N} \right\rangle \bigg|_C = \sum_{\bar{j}_N} g_{C,\bar{j}_N} \left\langle \hat{O}_{\bar{j}_N} \right\rangle + \sum_{\bar{j}_{N+2}} g_{C,\bar{j}_{N+2}} \left\langle \hat{O}_{\bar{j}_{N+2}} \right\rangle \tag{3.16}$$

$$\frac{d}{dt}\left\langle \hat{O}_{\bar{i}_N} \right\rangle \bigg|_{damp.} = -\gamma_{\bar{i}_N} \left(\left\langle \hat{O}_{\bar{i}_N,eq.} \right\rangle - \left\langle \hat{O}_{\bar{i}_N} \right\rangle \right) \tag{3.17}$$

where all summations are to be understood as sums over all coupled operator products. The individual terms shall be discussed in more detail in the following paragraphs. The first equation describes the free rotation of the expectation value within the complex plane. Looking at the definition (3.13), one will see that the operator products fall into two categories. The first category consists of operator products with pairwise identical indices of creation and annihilation operators which will give $\omega_{\bar{i}_N} = 0$. These operator products will be referred to as populations or density like quantities. The second category consists of all operator products with $\omega_{\bar{i}_N} \neq 0$. In general these operator products can be thought of as products of microscopic polarizations or screened microscopic polarizations.

---

[2] See appendices C.1 and C.2 for details about the implementation

The second equation describes the light-matter couplings among the operator products. The first thing one has to note is that due to energy conservation only operator products with differing (effective) eigenfrequencies may be coupled directly by the electric field. If, however, degeneracy is lifted by other terms from the Hamiltonian one may see finite coupling. The coupling elements are of the form

$$g_{lm,\bar{j}_N}(t) = \pm\frac{i}{\hbar}\boldsymbol{E}(t)\cdot\boldsymbol{\mu}_{mn}$$

where one index of the dipole matrix element comes from the multi index of the operator product on the left hand side of the equation and one index comes from the multi index of the coupled operator product. Without further knowledge about the system or the exact electric field one can not infer further properties of the coupling elements at this point.

The third equation describes the Coulomb coupling to operator products of equal or higher order. The structure of the coupling coefficients is not quite special.

$$g_{C,\bar{j}_{N(N+2)}} = -\frac{i}{\hbar}\sum_{\bar{k}_4}\alpha V_{k_1,k_2,k_3,k_4} \quad \alpha\in\{-1,1\}$$

Again the summation is not to be understood as a summation over all possible multi indices of length four. A noteworthy point is that the first term on the right hand side is only present if $N > 2$ whereas the coupling to the next higher order is only present if $N < 2N_{el}$ if N_{el} is the number of electrons in the system. If $N = 2N_{el}$ the coupled operator would consist of $N_{el}+1$ creation and $N_{el}+1$ annihilation operators. Application of such an operator product to a wave function of an N_{el}-electron system always evaluates to zero.

The last equation describes the assumed phenomenological damping which, in general, has to be taken with great care. In the current form this term describes a simple exponential decay to some equilibrium value. In reality one may find competing mechanisms which lead to decoherence and depopulation of excited states in combinations which will break this simple exponential behavior. More realistic damping terms may be derived using a formalism introduced by Lindblad [81]. A less mathematical description can be found in [82]. The fundamental idea is coupling of a given quantum system S to a large, but finite reservoir R giving a total system $S+R$. The Hamiltonian of the total system is then given as a sum of three different terms

$$\hat{H} = \hat{H}_S + \hat{H}_{S,R} + \hat{H}_R$$

where $\hat{H}_S$ and $\hat{H}_R$ describe the dynamics of the systems S and R in isolation whereas $\hat{H}_{S,R}$ governs coupling terms among S and R. Based on considerations for the evolution of a pure state vector in a closed quantum system Schaller derives the so called master equation in Lindblad form for the combined System $S+R$ by taking the partial trace over the System R

$$\frac{d}{dt}\rho = \mathcal{L}\rho = -i\left[\hat{H},\rho\right] + \sum_{\alpha,\beta}\gamma_{\alpha,\beta}\left(A_\alpha \rho A_\beta^\dagger - \frac{1}{2}\left\{A_\beta^\dagger A_\alpha,\rho\right\}\right). \tag{3.18}$$

It is pointed out that in this general form $\hat{H}$ is a hermitian operator which can be interpreted as an effective Hamiltonian governing the unitary evolution of the system, but need not coincide with the original system Hamiltonian. In terms of the considered FLS this means that for example the effective eigenenergies may shift due to coupling with an external bath. The second term in equation (3.18) then describes dissipative mechanisms leading to decay and decoherence in the considered system S.

Although phonon assisted dynamics have not been taken into account for the quantum dot structures introduced in sections 2.6.1-2.6.4, a brief overview over the derivation of the respective additional terms in the equations of motion shall be given, explaining why these terms have not been taken into account for the considered structures.

Considering the presence of phonons, the Hamiltonian (3.1) has to be augmented by two additional terms [83, 84], namely

$$\hat{H}_{ph} = \sum_{\mu,\boldsymbol{q}} \hbar\omega_{\mu\boldsymbol{q}} b_{\mu\boldsymbol{q}}^\dagger b_{\mu\boldsymbol{q}} \tag{3.19}$$

$$\hat{H}_{el-ph} = \sum_{ij\boldsymbol{q}\boldsymbol{k},\mu} g_{ij\mu\boldsymbol{q}} a_{i,\boldsymbol{k}+\boldsymbol{q}}^\dagger \left(b_{\mu\boldsymbol{q}} + b_{\mu,-\boldsymbol{q}}^\dagger\right) a_{j\boldsymbol{k}}. \tag{3.20}$$

The first equation describes the energy of the phonon system whereas the second equation describes the electron-phonon coupling. The coupling elements in (3.20) are given by

$$g_{ij\mu\boldsymbol{q}} = g_{ij\mu\boldsymbol{q}}^{3d} F_{ij}(\boldsymbol{q}) \tag{3.21}$$

$$g_{ijLO\boldsymbol{q}}^{3d} = \sqrt{\frac{e^2\hbar\omega_{LO}}{2\varepsilon_0 V}\left(\frac{1}{\varepsilon_b} - \frac{1}{\varepsilon_{st}}\right)\frac{1}{q}} \tag{3.22}$$

$$g_{ijLA\boldsymbol{q}}^{3d} = \delta_{ij}\sqrt{\frac{\hbar q}{2\rho c_{LA} V}} D_{\bar{\boldsymbol{i}}}. \tag{3.23}$$

Structurally, the given equations are not especially demanding or hard to understand. However, the presence of the so called form factors F_{ij} complicates the situation. The form factors are given by

$$F_{ij}(\boldsymbol{q}) = \int_\Omega \varphi_i^*(\boldsymbol{r})\varphi_j(\boldsymbol{r}) e^{i\boldsymbol{q}\cdot\boldsymbol{r}} d^3 r \tag{3.24}$$

which can be interpreted as the Fourier transform of the wavefunction overlap. The basic problem on incorporation of electron-phonon interaction for general structures becomes quite obvious when looking at the expression for the form factors. Without further simplifications due to structural symmetries, for each pair of state indices, i and j, one has to calculate form factors for a sufficiently large fraction of the momentum space explicitly for any direction. While the actual calculation for any pair of states can be done quite efficiently using a 3d FFT, the sheer number of additional terms appearing in the equation of motion renders a straight forward incorporation of these terms infeasible in terms of computational effort on time integration of the equations of motion. Another difficulty arises due to the fact, that, considering the quantum dot systems embedded in Schottky diodes, the phonon dispersions may be changed significantly. To this end, electron-phonon interaction has been neglected for most parts of this work and dephasings and depopulation accordingly treated phenomenologically via mono-exponential decay terms.

Coming back to the equations of motion (3.14)-(3.17) for a general FLS, it becomes obvious that the number of coupling terms in the equations of motion rapidly grow with an increasing number of electron states in the considered quantum system. To this end, parallel evaluation of the time derivatives would be highly desirable from a performance point of view. As it turns out, when using straight forward OpenMP parallelization which is possible for most C/C++ compilers, performance craters and the program runs even slower compared to single-threaded execution[3]. Accordingly the implemented program uses single-threaded execution for the time integration.

---

[3] By the time of writing down this thesis, a phenomenon called false sharing has been identified as the most probable cause of the performance penalty. See C.3 for further details.

3.2. Dynamics of a TLS

We consider a simple system consisting of just two allowed states. The state with the lower energy is initially populated with a single electron. Since there is no other electron to cause any Coulomb interaction the Hamiltonian of the system reduces to

$$\hat{H} = \varepsilon_0 a_0^\dagger a_0 + \varepsilon_1 a_1^\dagger a_1 - \boldsymbol{E}(t) \cdot \left(\boldsymbol{\mu}_{01} a_0^\dagger a_1 + \boldsymbol{\mu}_{10} a_1^\dagger a_0 \right). \tag{3.25}$$

The Heisenberg equations of motion for this system are then given by

$$\frac{d}{dt} a_0^\dagger a_0 = \frac{i}{\hbar} \boldsymbol{E}(t) \cdot \boldsymbol{\mu}_{01} a_0^\dagger a_1 - \frac{i}{\hbar} \boldsymbol{E}(t) \cdot \boldsymbol{\mu}_{10} a_1^\dagger a_0 \tag{3.26}$$

$$\frac{d}{dt} a_1^\dagger a_1 = \frac{i}{\hbar} \boldsymbol{E}(t) \cdot \boldsymbol{\mu}_{10} a_1^\dagger a_0 - \frac{i}{\hbar} \boldsymbol{E}(t) \cdot \boldsymbol{\mu}_{01} a_0^\dagger a_1 = -\frac{d}{dt} a_0^\dagger a_0 \tag{3.27}$$

$$\frac{d}{dt} a_1^\dagger a_0 = i\omega_{10} a_1^\dagger a_0 + \frac{i}{\hbar} \boldsymbol{E}(t) \cdot \boldsymbol{\mu}_{01} \left(a_1^\dagger a_1 - a_0^\dagger a_0 \right) \tag{3.28}$$

$$\frac{d}{dt} a_0^\dagger a_1 = i\omega_{01} a_0^\dagger a_1 + \frac{i}{\hbar} \boldsymbol{E}(t) \cdot \boldsymbol{\mu}_{10} \left(a_0^\dagger a_0 - a_1^\dagger a_1 \right) \tag{3.29}$$

where

$$\omega_{ij} = \frac{\varepsilon_i - \varepsilon_j}{\hbar}.$$

Looking of the first two equations one finds the conservation law

$$a_1^\dagger a_1 = 1 - a_0^\dagger a_0 \tag{3.30}$$

and the equations for the 'interband' coherences reduce to

$$\frac{d}{dt} a_1^\dagger a_0 = i\omega_{10} a_1^\dagger a_0 + \frac{i}{\hbar} \boldsymbol{E}(t) \cdot \boldsymbol{\mu}_{01} \left(1 - 2a_0^\dagger a_0 \right) \tag{3.31}$$

$$\frac{d}{dt} a_0^\dagger a_1 = i\omega_{01} a_0^\dagger a_1 + \frac{i}{\hbar} \boldsymbol{E}(t) \cdot \boldsymbol{\mu}_{10} \left(2a_0^\dagger a_0 - 1 \right) \tag{3.32}$$

Given the fact that

$$a_1^\dagger a_0 = \left(a_0^\dagger a_1 \right)^\dagger \Rightarrow \left\langle a_1^\dagger a_0 \right\rangle = \left\langle a_0^\dagger a_1 \right\rangle^*$$

one ends up with a system of two coupled equations fully describing the dynamics of the two level system

$$\frac{d}{dt} \left\langle a_0^\dagger a_0 \right\rangle = \frac{i}{\hbar} \boldsymbol{E}(t) \cdot \boldsymbol{\mu}_{01} \left\langle a_0^\dagger a_1 \right\rangle - \frac{i}{\hbar} \boldsymbol{E}(t) \cdot \boldsymbol{\mu}_{10} \left\langle a_0^\dagger a_1 \right\rangle^* \tag{3.33}$$

$$\frac{d}{dt} \left\langle a_0^\dagger a_1 \right\rangle = i\omega_{01} \left\langle a_0^\dagger a_1 \right\rangle + \frac{i}{\hbar} \boldsymbol{E}(t) \cdot \boldsymbol{\mu}_{10} \left(2 \left\langle a_0^\dagger a_0 \right\rangle - 1 \right) \tag{3.34}$$

For numerical evaluation it is advantageous to transform these equations into a reference frame where the individual quantities vary slowly. This technique is commonly known as rotating wave approximation (RWA) in literature. To this end one introduces new quantities such that

$$\left\langle a_i^\dagger a_j \right\rangle = \widetilde{\left\langle a_i^\dagger a_j \right\rangle} e^{i(n_{ij}\omega_l + \delta)t} \tag{3.35}$$

which corresponds to the frequency decomposition

$$\omega_{ij} = n_{ij}\omega_l + \delta.$$

Considering resonant excitation, i.e. $\omega_l = \omega_{10}$, insertion of (3.35) into (3.33) and (3.34) yields

$$\begin{align}
\frac{d}{dt}\left\langle a_0^\dagger a_0 \right\rangle &= \frac{i}{\hbar}\boldsymbol{E}(t)\cdot\boldsymbol{\mu}_{01}\widetilde{\left\langle a_0^\dagger a_1 \right\rangle} e^{in_{01}\omega_l t} - \frac{i}{\hbar}\boldsymbol{E}(t)\cdot\boldsymbol{\mu}_{10}\widetilde{\left\langle a_0^\dagger a_1 \right\rangle}^{*} e^{-in_{01}\omega_l t} \tag{3.36}\\
\frac{d}{dt}\widetilde{\left\langle a_0^\dagger a_1 \right\rangle} &= \frac{i}{\hbar}\boldsymbol{E}(t)\cdot\boldsymbol{\mu}_{10}\left(2\left\langle a_0^\dagger a_0 \right\rangle - 1\right) e^{-in_{01}\omega_l t} \tag{3.37}
\end{align}$$

To further simplify these equations consider the exciting electric field to be of the following form

$$\boldsymbol{E}(t) = \boldsymbol{E}_0 e^{i\omega_l t} + \boldsymbol{E}_0^* e^{-i\omega_l t} \tag{3.38}$$

Since $\omega_{01} < 0$ one finds $n_{01} = -1$ in case of resonant excitation. Substituting $n_{01} = -1$ and inserting (3.38) yields

$$\begin{align}
\frac{d}{dt}\left\langle a_0^\dagger a_0 \right\rangle = {} & \frac{i}{\hbar}\boldsymbol{E}_0\cdot\boldsymbol{\mu}_{01}\widetilde{\left\langle a_0^\dagger a_1 \right\rangle} + \frac{i}{\hbar}\boldsymbol{E}_0^*\cdot\boldsymbol{\mu}_{01}\widetilde{\left\langle a_0^\dagger a_1 \right\rangle} e^{-2i\omega_l t}\\
& - \frac{i}{\hbar}\boldsymbol{E}_0\cdot\boldsymbol{\mu}_{10}\widetilde{\left\langle a_0^\dagger a_1 \right\rangle}^{*} e^{2i\omega_l t} - \frac{i}{\hbar}\boldsymbol{E}_0^*\cdot\boldsymbol{\mu}_{10}\widetilde{\left\langle a_0^\dagger a_1 \right\rangle}^{*} \tag{3.39}\\
\frac{d}{dt}\widetilde{\left\langle a_0^\dagger a_1 \right\rangle} = {} & \frac{i}{\hbar}\boldsymbol{E}_0\cdot\boldsymbol{\mu}_{10}\left(2\left\langle a_0^\dagger a_0 \right\rangle - 1\right) e^{2i\omega_l t} + \frac{i}{\hbar}\boldsymbol{E}_0^*\cdot\boldsymbol{\mu}_{10}\left(2\left\langle a_0^\dagger a_0 \right\rangle - 1\right) \tag{3.40}
\end{align}$$

If the energy difference between the two eigenstates is on the order of 1 eV the terms containing the exponential factors are rapidly oscillating and tend to average out during time integration (Riemann-Lebesgue lemma). So in order to further simplify the equations one may just drop these terms and ends up with

$$\begin{align}
\frac{d}{dt}\left\langle a_0^\dagger a_0 \right\rangle &= \frac{i}{\hbar}\boldsymbol{E}_0\cdot\boldsymbol{\mu}_{01}\widetilde{\left\langle a_0^\dagger a_1 \right\rangle} - \frac{i}{\hbar}\boldsymbol{E}_0^*\cdot\boldsymbol{\mu}_{10}\widetilde{\left\langle a_0^\dagger a_1 \right\rangle}^{*} \tag{3.41}\\
\frac{d}{dt}\widetilde{\left\langle a_0^\dagger a_1 \right\rangle} &= \frac{i}{\hbar}\boldsymbol{E}_0^*\cdot\boldsymbol{\mu}_{10}\left(2\left\langle a_0^\dagger a_0 \right\rangle - 1\right) \tag{3.42}
\end{align}$$

Equations (3.41)-(3.42) are called the optical Bloch equations as their structure is identical to the equations governing the dynamics of a spin 1/2 particle in an external magnetic field. Since all appearing quantities are now just slowly varying one may use a much larger time step when numerically solving the equations. However, one has to take care if the energy difference between the states get small. In this case neglection of the exponential terms might introduce significant errors.

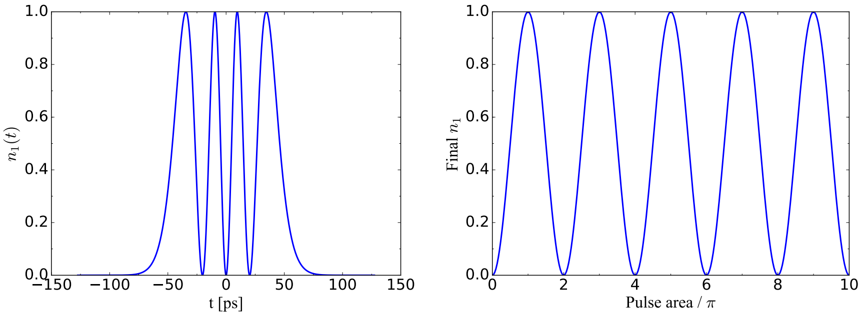

Figure 3.2.: Rabi oscillations of the excited state population. Left: Time resolved Rabi oscillations of the population of the excited state at a pulse area of 8π of the exciting light field. Right: Final population of the excited state depending on the pulse area of the exciting pulse.

Although equations (3.41)-(3.42) are useful to gain general insight of the dynamics of a quantum system under the influence of an external electric field they are not quite useful for modeling realistic systems. In their current form these equations are not able to describe the decay of microscopic polarizations or generated population of the excited state observed in experiments since all terms appearing on the right-hand side are products containing the external electric field. In short this means that once the exciting pulse is gone the given quantities will not change their absolute values any more. A straightforward fix is provided by introducing phenomenological damping terms

$$\frac{d}{dt}\left\langle a_0^\dagger a_0\right\rangle\Big|_{damp.} = -\underbrace{\frac{1}{T1}}_{\gamma_1}\left(1-\left\langle a_0^\dagger a_0\right\rangle\right) \tag{3.43}$$

$$\frac{d}{dt}\widetilde{\left\langle a_0^\dagger a_1\right\rangle}\Big|_{damp.} = -\underbrace{\frac{1}{T_2}}_{\gamma_2}\widetilde{\left\langle a_0^\dagger a_1\right\rangle}. \tag{3.44}$$

These terms lead to a exponential decay of the induced microscopic polarization and the excited charge carrier density at the cost of two additional fitting parameters. In general both of the introduced decays are caused by a combination of different effects and by no means independent of each other. For example the dephasing of the microscopic polarization results from so called *pure* dephasing mechanisms, i.e. processes which do not alter the populations, and processes which lead to a change in the population [85]. As Skinner puts it, *pure dephasing* can be described by processes whose sole effect is a stochastic change of the eigenenergies in the system resulting in the loss of a defined phase difference between the two eigenstates in the system. For a two level system the dephasing time of the microscopic polarization may be written as

$$\frac{1}{T_2} = \frac{1}{T_{2,pure}} + \frac{1}{2T_1}. \tag{3.45}$$

The interrelation of the two decay constants arises from the fact that any process that destroys population of the excited state automatically destroys the polarization of the system as well. In the so called coherent limit ($T_{2,pure} = 0$) one finds $T_2 = 2T_1$ [86]. This corresponds to the case in which only spontaneous radiative decay is considered as a process destroying population in the excited state.

Figure 3.3 shows the normalized values of $|p|$ and n_1 over time where

$$\begin{aligned} p &:= \left\langle a_0^\dagger a_1 \right\rangle \\ n_1 &:= \left\langle a_1^\dagger a_1 \right\rangle \end{aligned}$$

and $T_1 = 400$ ps considering a Gaussian excitation with 50 ps full width at half intensity (FWHI).

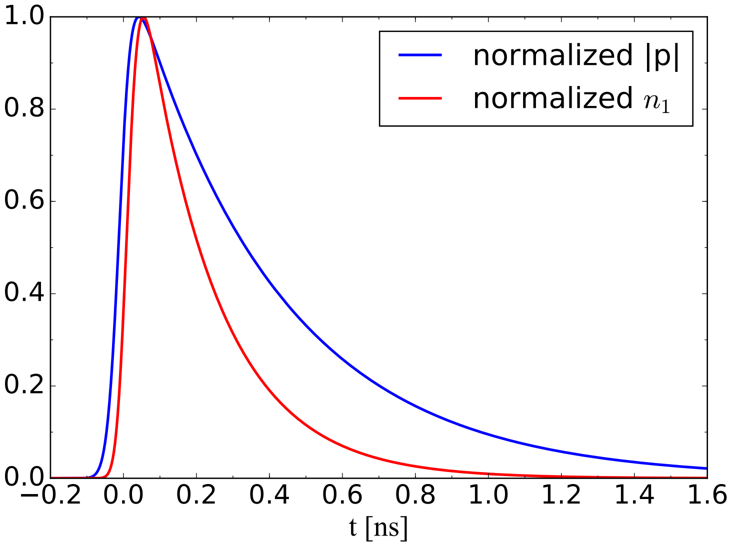

Figure 3.3.: Normalized values of $|p|$ and $|n_1|$ over time

3.3. Modeling Ramsey-type experiments in terms of a FLS [4]

The original experiment proposed by Ramsey [27] was designed for molecular beams and basically consisted of two interaction zones with oscillating fields with a non-interacting zone of variable length between them. Nowadays, similar experiments can be performed using a suitable pulsed laser source. Recently such a setup has been used by the experimental group of Artur Zrenner at Paderborn University to demonstrate coherent control of a field tunable quantum dot embedded in a Schottky diode. The quantum dot is illuminated with a sequence of two $\frac{\pi}{2}$ pulses with a variable pulse delay T_o as depicted in figure 3.4 a). The applied bias voltage at the gate electrode controls the detuning of the fundamental exciton resonance in the quantum dot from the central frequency of the two laser fields. Depending on the detuning, the superposition state generated by the first optical pulse picks up a certain phase between the two optical pulses and the second laser pulse may interact constructively or destructively with it, i.e the laser may cause a complete population inversion or a complete depopulation as depicted in figure 3.4 b). In addition to the static voltage used to tune the quantum dot resonance, the experimental setup allows for application of an ultra fast electric control pulse which adds to the already applied gate voltage and may be used to change the phase picked up by the superposition state between the two optical pulses.

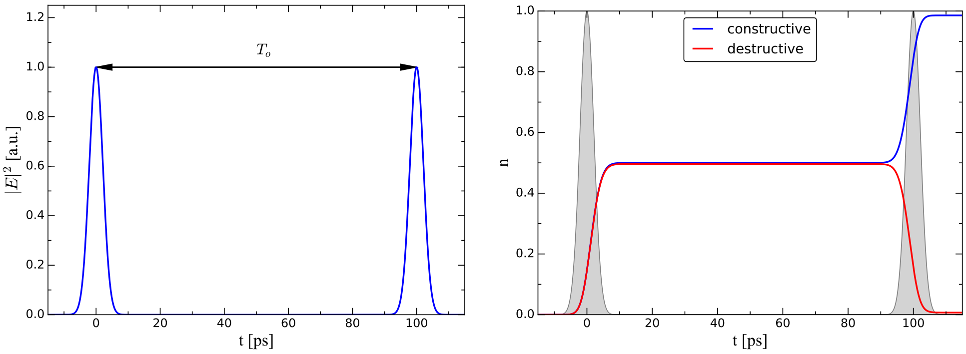

Figure 3.4.: Schematic pulse sequence for the Ramsey type experiments. Left: Sequence of the optical pulses. Right: Temporal evolution of the population of the excited state for constructive and destructive interaction between the generated superposition state and the second laser pulse.

Figure 3.5 shows the Ramsey fringe pattern depending on the applied bias voltage without an applied control pulse. The extremal points with a small magnitude of the photocurrent correspond to a destructive interaction of the second laser pulse with the generated superposition state whereas the extremal points with larger magnitude of the photocurrent correspond to constructive interaction. As measuring the current

---

[4] Parts of the results presented in this section have been published in [28]

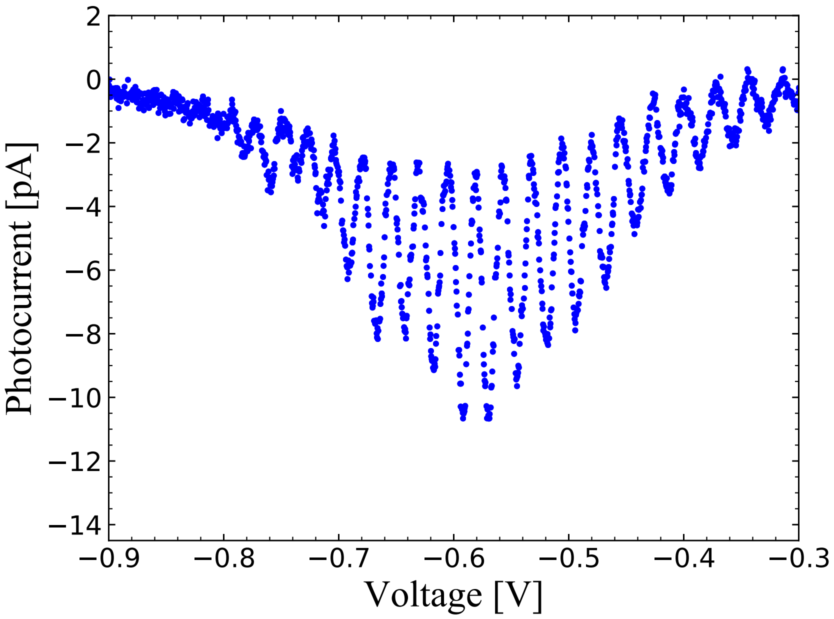

Figure 3.5.: Photocurrent signal from a quantum dot embedded in a Schottky diode depending on the applied bias voltage. The data have been kindly provided by the experimental group of Prof. Dr. Artur Zrenner, by now published in [28]

produced by a single electron is pretty demanding, the experiment is performed with a pulsed laser source which generates the optical pulse pairs with a repetition rate of ~80 MHz. The measured peak magnitude of the photocurrent corresponds roughly to a little below one extracted electron per optical pulse pair.

In order to accurately model the experimental data, one has to think about how the photocurrent signal is generated. Considering constructive interaction of the second laser pulse with the superposition state generated by the first laser pulse, the pair of optical pulses creates a single exciton. Sticking to the pure electron picture, the given pulse sequence promotes a single electron from its ground state to an excited state. In order to generate a measurable current signal, the electron has to tunnel out of the quantum dot, most probably to the back contact of the Schottky diode. For simplicity, equal tunneling rates for electrons and holes may be assumed, such that at the same time the excited electron tunnels to the back contact the hole tunnels to the gate electrode, resulting in a net current of one electron per pulse pair. So, one possibility to model the experiment is to integrate the equations of motion for a TLS in the coherent limit using the population decay term as a feed for the photocurrent signal. The resulting equations of motion are given in (3.46)-(3.49)

$$\frac{d}{dt}p(t) = i\frac{\Omega_0}{2}\left(n_1(t) - n_0(t)\right) - i\delta p(t) - \left(\frac{2}{T_1}\right)p \tag{3.46}$$

$$\frac{d}{dt}n_0(t) = i\frac{\Omega_0}{2}\left(p^*(t) - p(t)\right) + \frac{1}{T_1}(1 - n_0(t)) \tag{3.47}$$

$$\frac{d}{dt}n_1(t) = i\frac{\Omega_0}{2}\left(p(t) - p * (t)\right) - \frac{1}{T_1}n_1(t) \tag{3.48}$$

$$\frac{d}{dt}PC(t) = \frac{1}{T_1}n_1 \tag{3.49}$$

Integrating these equations with $T_1 = 350$ ps, yields a theoretical fringe pattern as given in figure 3.6. The optical pulses have been modeled by two Gaussian functions with a FWHI value of 5 ps and an amplitude adjusted to give a pulse area of $\frac{\pi}{2}$ for each of the pulses. In comparison to the experimentally obtained signal in figure 3.5 one observes a comparable peak magnitude of the photocurrent signal whereas the current minima of the experimental curve get closer to zero compared to the calculated photocurrent signal. In principal, one can get the current minima closer to zero by increasing the value of T_1 since this decreases the pick up of signal between the two pulses. Calculated fringe patterns for different values of T_1 are plotted in figure 3.7.

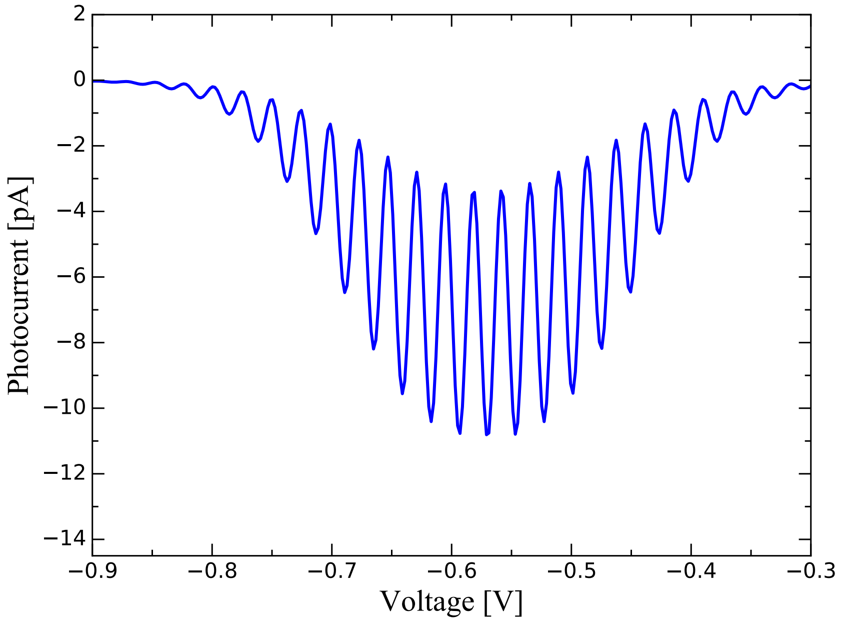

Figure 3.6.: Calculated photocurrent signal without applied control pulse.

As can be seen so far, the minima and maxima of the fringe pattern depend on the tunneling time T_1. Defining the current difference of two neighboring extremal points

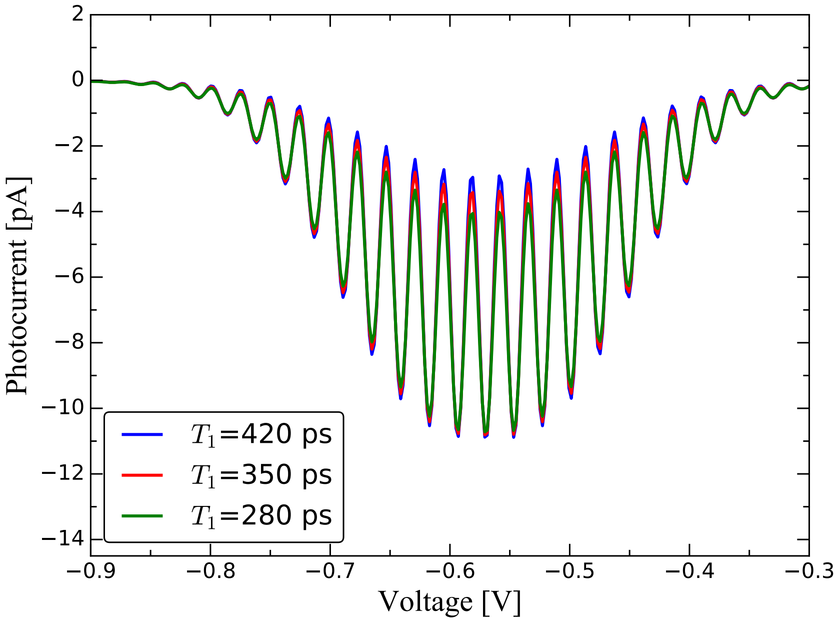

Figure 3.7.: Calculated photocurrent signal using TLS equations of motion in the coherent limit with T_1=280 ps.

of the fringe pattern as fringe contrast, one observes an asymmetric loss of fringe contrast for the experimentally obtained signal. Looking at the calculated signals in figures 3.7, the loss of fringe contrast is totally symmetric, regardless of the chosen value of T_1. In this regard, the description of the experiment in terms of a TLS delivers results comparable to the experimental data, but is not able to reproduce all features seen in the experiment.

As already mentioned in the beginning of this section, the experimental setup allows application of ultra fast electronic pulses which act on top of the applied static voltage and may change the phase picked up between the two optical pulses. Schematically one can think of a pulse sequence as given in figure 3.8. The shown schematic represents a somewhat idealized pulse sequence for this kind of experiment. In principle such a pulse sequence could be achieved by increasing the delay between the two optical pulses. In practice, however, the delay values are strongly limited by the life time of the excitons in the quantum dot system. In the limit of delays longer than the exciton life time, the two optical pulses would generate independent photocurrent signals and one would totally loose contrast. On the other hand, considering short optical pulses with a small delay, this setup could be used to sample the electric field generated by the control pulse. As already mentioned, the applied control voltage acts on top of an already applied voltage. So the total voltage determining the detuning of the exciton is given by

$$V(t) = V_{static} + V_c(t)$$

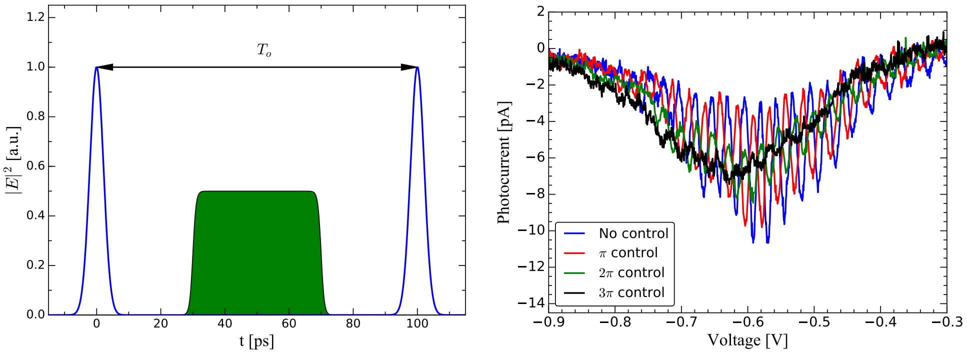

Figure 3.8.: Ramsey-type experiment with applied control pulse. Left: Schematic pulse sequence. Right: Experimental photocurrent signals showing a phase change of the fringe pattern from 0 to 3π. The data have been kindly provided by the experimental group of Prof. Dr. Artur Zrenner, by now published in [28]

resulting in a time dependent detuning of the form

$$\delta(t) = C\left(V_{static} + V_c(t)\right) \tag{3.50}$$

where C is a calibration constant depending on the exact structure of the diode. From absorption measurements in the photocurrent regime C has been estimated as ~ 1.78 meV/V. In the limit of ultra short optical pulses, the phase picked up between the two optical pulses is given as

$$\Phi = \int_{t_0}^{t_0+T_o} C\left(V_{static} + V_c(t)\right) dt = \underbrace{C\int_{t_0}^{T_o} V_{static} dt}_{\Phi_{static}} + \underbrace{C\int_{t_0}^{T_o} V_c(t) dt}_{\Delta\Phi} \tag{3.51}$$

If the delay T_o is chosen such that $V(t)$ varies significantly only at timescales considerably larger than T_o, the second term in (3.51) may be approximated as

$$\Delta\Phi \approx C V_c(t_0) T_o \tag{3.52}$$

giving

$$V_c(t_0) \approx \frac{\Delta\Phi}{C T_o}. \tag{3.53}$$

This means, by measuring the phase change of a given fringe pattern while scanning the value of t_0 over the applied control pulse, one is able to reconstruct the electric signal of the control pulse. Leaving the limit of short optical pulses and small pulse

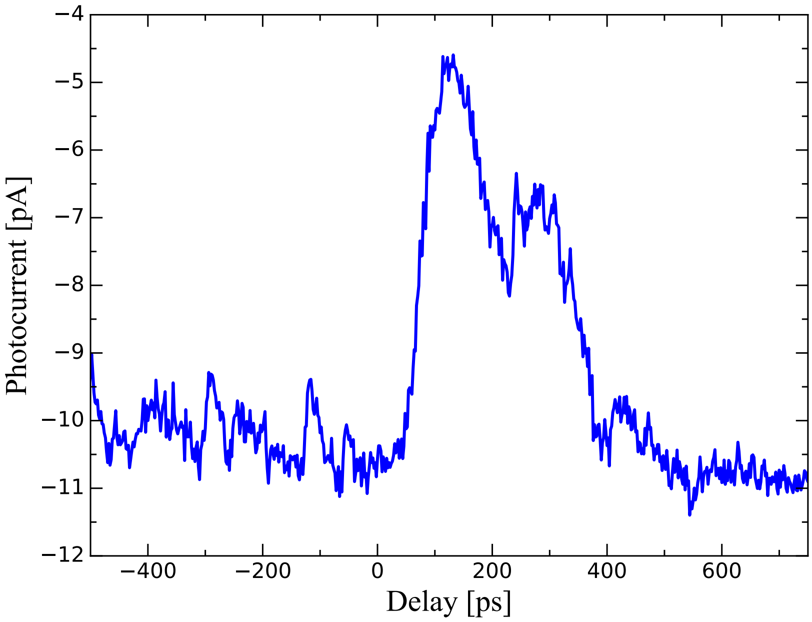

Figure 3.9.: Photocurrent signal obtained by scanning the optical pulse pair over the applied control pulse. The data have been kindly provided by the experimental group of Prof. Dr. Artur Zrenner, by now published in [28].

delays, the fundamental reasoning stays the same, but the measured phase difference gives information only about the integral over the control voltage. Actually, in order to nicely resolve the phase change of a complete fringe pattern like the experimental data shown above, one has to consider sufficiently large delays of the optical pulses since the pulse delay limits the maximum number of visible fringes when keeping the interval of scanned bias voltages fixed.

As the experimental setup did not allow full control over the shape of the applied control pulse, an attempt was made to retrieve the actual form of the pulse by aforementioned sampling technique. By scanning the optical pulse pair over the control π control pulse the photocurrent signal plotted in figure 3.9 has been obtained. As can be seen, the sampling curve is quite nontrivial. By simple reasoning one can only conclude two things. Firstly, the applied control pulse is significantly longer than the delay between the optical pulses. Secondly, the pulse has to be asymmetric. The first observation gets immediately clear by looking at the sampling signal. For the second observation one needs to recall the integral representation of the additional phase pick up due to the control pulse

$$\Delta\Phi = C \int_{t_0}^{t_0+T_o} V_c(t)dt.$$

If the control pulse were symmetric with respect to some point in time, one would expect to find a symmetric sampling signal with maximum amplitude when the control pulse is centered between the two optical pulses, i.e. the peak voltage is located at $t = t_0 + \frac{T_o}{2}$. However, in order to accurately model the experimental data for applied control pulses, a reasonable approximation of the control voltage signal is needed. As the number of pulse shapes resulting in the observed sampling signal is unlimited, at least in principle, a simple Gaussian function has been chosen for the control voltage.

$$V(t) = V_0 e^{-\left(\frac{t-T_c}{\tau_c}\right)^2} \tag{3.54}$$

Using an optical pulse pair with the first pulse fixed at $t = 0$ and $T_o = 100$ ps, the free parameter T_c may serve as an equivalent for the delay value from the experiment. The aim was then to find proper values for V_0 and τ_c in order to give a rise time of the photocurrent signal comparable to the one observed in experiment, i.e. a phase change from 0 to π on the order of 100 ps. Fixing the value of V_0 to 13 mV, calculations for different values of τ_c have been performed in order to find a pulse width giving the desired rise time. The results are shown in figure 3.10. As has already been predicted, the calculated signals are symmetric about a delay value of 50 ps which corresponds to the center of the time interval defined by the two optical pulses. The rise times obtained

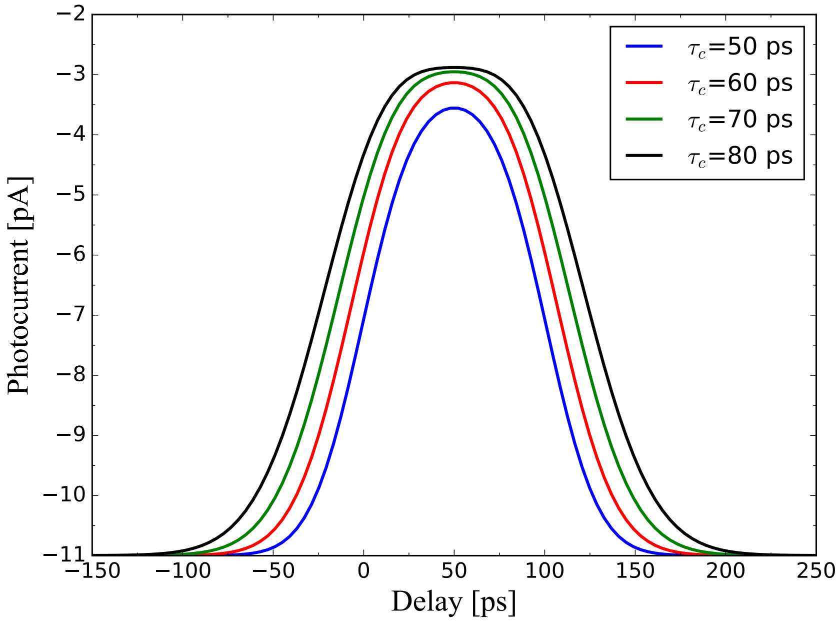

Figure 3.10.: Calculated photocurrent sampling signal for different widths of the control pulse.

for the two shorter control pulses seems somewhat too low whereas the rise times of 70 ps and 80 ps pulses are quite close to the rise time observed in experiment. Looking closer, one observes some sort of saturation behavior for the 80 ps pulse, recognizable by the flat behavior of the curve around 50 ps delay. This is an indication, that the maximum phase change which may be caused by this pulse, is already beyond π. For this reason, $\tau_c = 70$ ps has been chosen as the width value for the control pulse while searching for a suitable value of the amplitude V_0. Figure 3.11 shows the calculated sampling signals for different amplitudes of the control pulse.

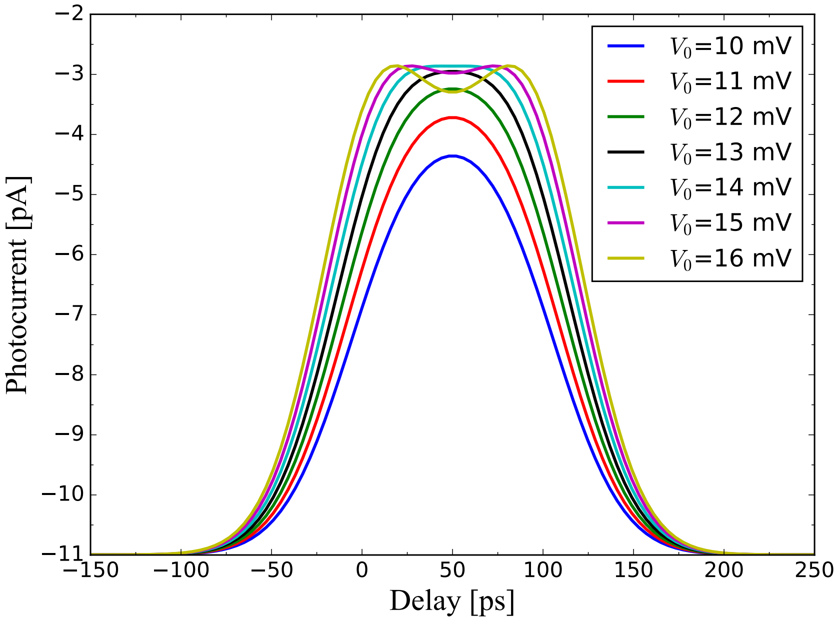

Figure 3.11.: Calculated photocurrent sampling signal for different amplitudes of the control pulse.

As can be seen, the full phase change of π can not be achieved for pulse amplitudes smaller than 13 mV. For amplitudes larger than 13 mV, the already mentioned saturation behavior gets visible. However, for the pulse amplitudes of 15 mV and 16 mV one observes some oscillatory behavior around a delay of 50 ps. This clearly indicates that the maximum phase change goes significantly beyond π. For this reason, $V_0 = 13$ mV, $\tau_c = 70$ ps and $T_c = 50$ ps haven been chosen as parameters for the π control pulse. Considering the 2π and 3π control pulses, the width and delay have been kept fixed and just the amplitude has been scaled up. The results are shown in figure 3.12. Table 3.1 summarizes the parameters for the three control pulses.

Although the desired shift of the fringe pattern compared to the pattern obtained without applied control pulse has been achieved, deviations from the experimental

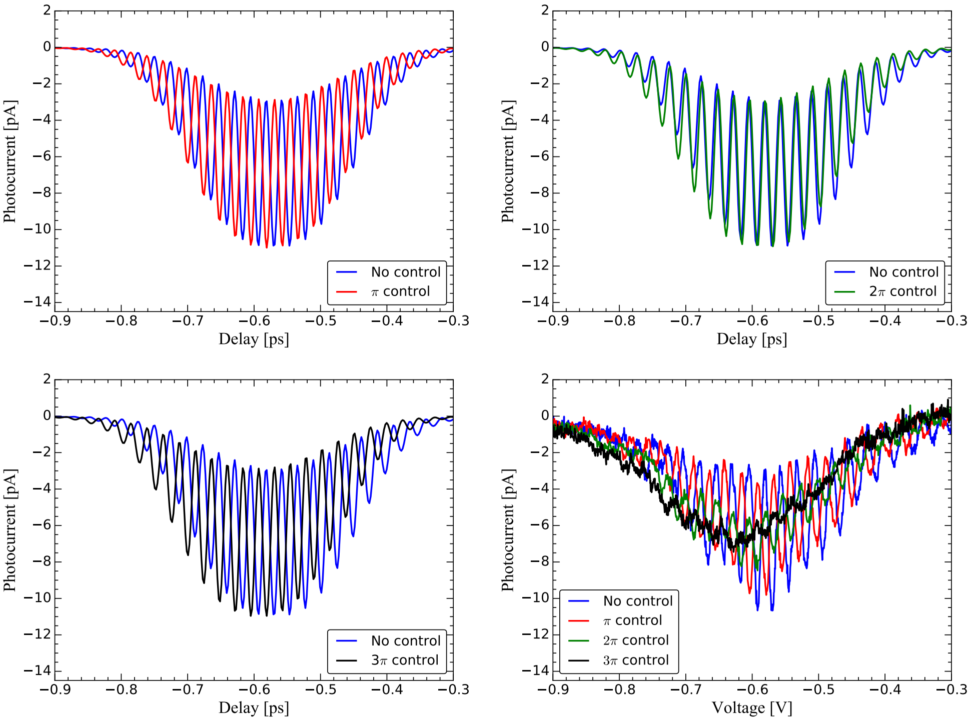

Figure 3.12.: Calculated fringe patterns with applied π, 2π, and 3π control pulses. Top left: π control pulse. Top right: 2π control pulse. Bottom left: 3π control pulse. Bottom right: Photocurrent signals from the experiment already shown in figure 3.8

data presented in figure 3.8 are quite obvious. From the theoretical curves one would conclude that the applied control pulse merely shifts the fringe pattern towards larger negative bias voltages. This shift feature is also visible in the experimental data. However, the experimental curves suffer from a significant loss of fringe contrast with increasing phase shift which can not be reproduced by the theory so far. In addition to the obviously missing loss of contrast, another issue still not addressed is the asymmetric loss of fringe contrast which is visible in the experimental data, but not in the calculated curves. The only free parameter considering the underlying TLS so far is the tunneling time T_1. As has been shown, changing this parameter does not change the symmetry of the calculated curves. However, the data shown in figure 3.7also indicate that a smaller T_1 value leads to a reduced fringe contrast. To this end, the desired asymmetric loss of fringe contrast could be easily accounted for by introduction of a voltage dependent tunneling time. From a physical point of view, this makes perfect sense when keeping in mind that the quantum dot is embedded in a Schottky diode. Changing the applied bias voltage results in a different tunneling barrier for electrons towards the back contact with higher tunneling rates at larger negative bias voltages.

Parameter	π	2π	3π
V_0 [mV]	13	26	41
T_c [ps]	50	50	50
τ_c [ps]	70	70	70

Table 3.1.: Fitted parameters for π, 2π, and 3π control pulses centered between the two optical pulses.

In order to account for the voltage dependent, eventually asymmetric, tunneling rates for electrons and holes, a model which has been previously used in the description of a similar experiment [87] has been adopted and shall be explained in the following. Within a dressed state picture one might think as follows. In its ground state, the quantum dot contains no excitons, i.e. it is empty, while in its excited state the quantum dot contains a single exciton. Both charge carriers may tunnel individually from the quantum dot, giving rise to two additional states in the given picture. The first of these states results from the electron tunneling out of the quantum dot, once the exciton state has been prepared, leaving the quantum dot in a positively charged state. The second state arises if the hole tunnels out of the quantum dot, leaving the quantum dot in a negatively charged state. Figure 3.13 gives a graphical illustration. A noteworthy point is, that the single charge states may not be excited by interaction

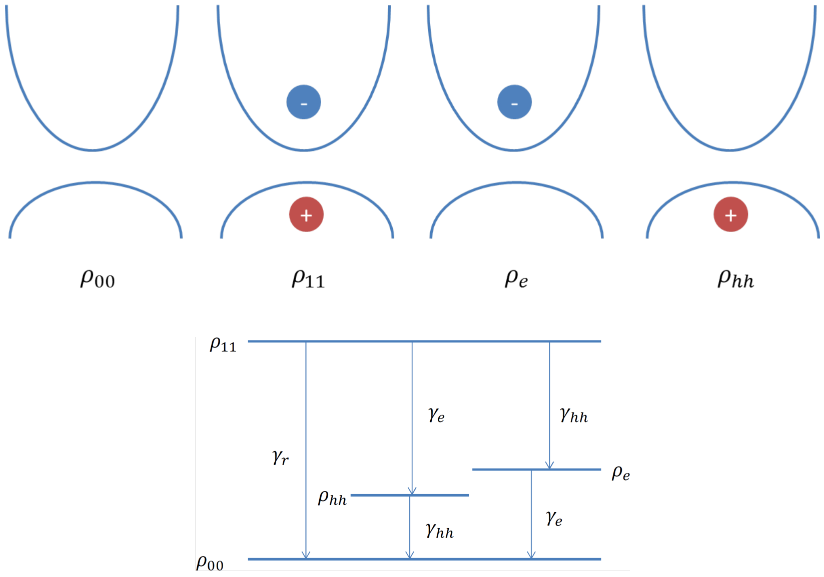

Figure 3.13.: Modified model to account for asymmetric tunneling rates of electrons and holes. The diagram on the bottom indicates the decay channels by which the system can relax to its ground state.

with an optical field but result solely from tunneling events.
The equations of motion in RWA for this system are

$$\frac{d}{dt}\rho_{01} = i\frac{\Omega_0}{2}e^{i\Phi}\left(\rho_{11}e^{-i\Phi} - \rho_{00}e^{i\Phi}\right) - i\delta\rho_{01} - \left(\frac{\gamma_r + \gamma_e + \gamma_{hh}}{2}\right)\rho_{01} \tag{3.55}$$

$$\frac{d}{dt}\rho_{00} = i\frac{\Omega_0}{2}\left(\rho_{10}e^{i\Phi} - \rho_{01}e^{-i\Phi}\right) + \gamma_r\rho_{11} + \gamma_{hh}\rho_{hh} + \gamma_e\rho_e \tag{3.56}$$

$$\frac{d}{dt}\rho_{11} = i\frac{\Omega_0}{2}\left(\rho_{01}e^{-i\Phi} - \rho_{10}e^{i\Phi}\right) - \underbrace{(\gamma_r + \gamma_e + \gamma_{hh})}_{=:\Gamma}\rho_{11} \tag{3.57}$$

$$\frac{d}{dt}\rho_{hh} = \gamma_e\rho_{11} - \gamma_{hh}\rho_{hh} \tag{3.58}$$

$$\frac{d}{dt}\rho_e = \gamma_{hh}\rho_{11} - \gamma_e\rho_e \tag{3.59}$$

$$\frac{d}{dt}PC = (\gamma_e + \gamma_{hh})\,\rho_{11} \tag{3.60}$$

For simplicity, the radiative recombination rate γ_r and the hole tunneling rate γ_{hh} are assumed to be constant. An approximated expression for the tunneling rate of a charge carrier confined in a quantum dot is given by

$$\gamma_t = \frac{\hbar}{8m^*a^2}\exp\left(\frac{-4\sqrt{2m^*}}{3eE\hbar}\sqrt{E_{conf}}^3\right) \tag{3.61}$$

with the effective mass m^*, the height of the quantum dot a, the static electric field E, and the confinement energy E_{conf}. Although the height of the quantum dot and the confinement energy are not known, the given equation predicts that the following proportionality should hold:

$$\gamma_t = A\exp\left(-\frac{B}{V}\right) + C_t$$

provided that the static electric field is proportional to the applied bias voltage. The additive constant is introduced to account for eventual finite tunneling rates at 0 applied voltage. Values A, B and C_t have been determined by fitting the peak width of absorption peaks measured in the photocurrent regime. Assuming a Lorentzian line shape and that the width is dominated by electron tunneling, the following values have been determined

Parameter	Value
A	0.00153086 1/fs
B	-4.38 1/V
C_t	$4.88757\cdot 10^{-6}$ 1/fs

Considering a finite hole tunneling rate and radiative recombination rate each of 1 ns, the fitted parameters have been adjusted to

Parameter	Value
A	0.00153086 1/fs
B	-5 1/V
C_t	$6.10947 \cdot 10^{-6}$ 1/fs

However, considering a voltage dependent decay rate may not explain the systematic loss of fringe contrast for stronger control pulses observed in the experiment. A mechanism discussed as a candidate to explain the loss of fringe contrast is time jitter. Considering that the synchronization of the optical pulses and the control pulses is not perfect, the control pulse might produce different phase changes for subsequent shots during a measurement. As the measured photocurrent can be thought of as the average photocurrent from a series of subsequent shots, a possible way to account for time jitter is drawing the center of the control pulse from a given random distribution. Considering the control pulses centered between the two optical pulses the required interval from which the center of the control pulse is drawn is far too big to match experimental reality. Looking closer at the experimental data one observes that the fringe envelope is shifted towards larger negative bias voltages for increasing strength of the control pulse.

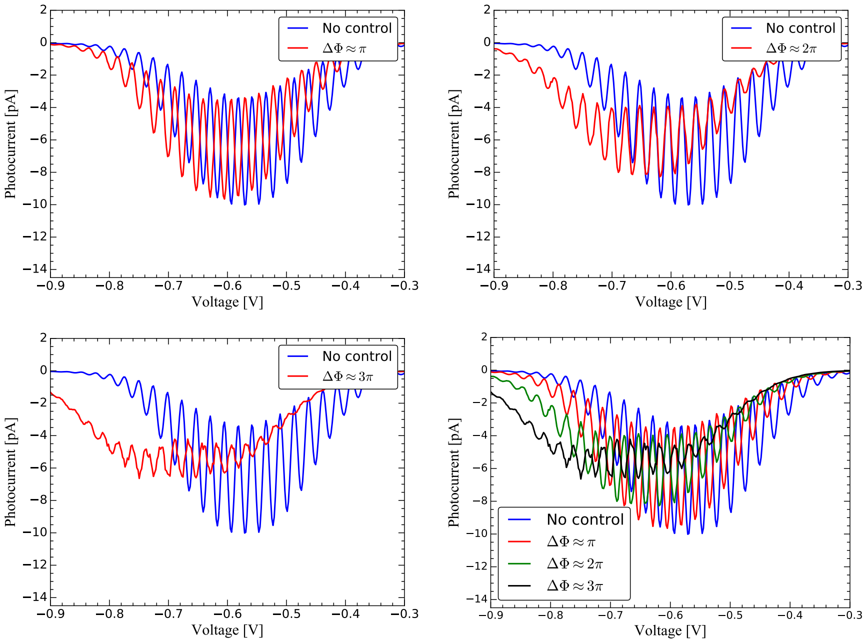

Figure 3.14.: Calculated photocurrent signals for time jittered control pulses.

This is an indication, that either of the optical pulses has a significant overlap with the control pulse. To this end, a new set of control pulses centered on the first optical pulse has been set up, considering the interval [-5.5ps;5.5ps] for the center of the respective control pulse. Figure 3.14 shows the simulation results.

The photocurrent signals have been simulated by averaging 100 individual single shot calculations for each bias voltage drawing the center of the respective control pulse from a uniform probability distribution on the mentioned interval. Although no quantitative agreement between the theoretical and the experimental data has been achieved, the theoretical fringe patterns resemble the features seen in the experiment. For increasing strength of the control pulse the envelope of the fringe pattern is shifted toward larger negative bias voltages and the fringe patterns suffer from a significant loss of contrast for stronger control pulses.

A similar effect can be achieved jittering the amplitude of the control pulses as can be seen in figure 3.15. In this case the center of the control pulses has been fixed to the center of the first optical pulse and its amplitude has been drawn from the interval $V_0 \pm 10$ mV. As for the time jittered control pulses, the curves have been obtained by averaging over 100 single shot calculations for each bias voltage.

Parameter	π	2π	3π
V_0 [mV]	60	120	180
T_c [ps]	0	0	0
τ_c [ps]	70	70	70

Table 3.2.: Fitted parameters for π, 2π, and 3π control pulses centered on the first optical pulse.

For both time and amplitude jittered control pulses the theoretical photocurrent curves show a stronger shift of the fringe envelope than the experimental curves which is a clear indication that the amplitudes of the chosen pulses are too large. Nevertheless, time and amplitude jitter can, at least in principle, explain the experimentally observed loss of fringe contrast and overall shift of the fringe pattern towards larger negative bias voltages. As the amplitude jitter needs a relatively large amplitude of 10 mV it can possibly ruled out as a realistic candidate.

Another possible explanation for the loss of fringe contrast that has been discussed with the group of Prof. Dr. Artur Zrenner is electron tunneling from the back contact into the quantum dot. In the given experimental setup it is possible that the diode comes close to the forward bias regime allowing electrons from the back contact to tunnel into an unoccupied state of the quantum dot. The additional charge then dephases the considered exciton TLS and may cause the loss of fringe contrast. In the current model, however, this effect can not be captured.

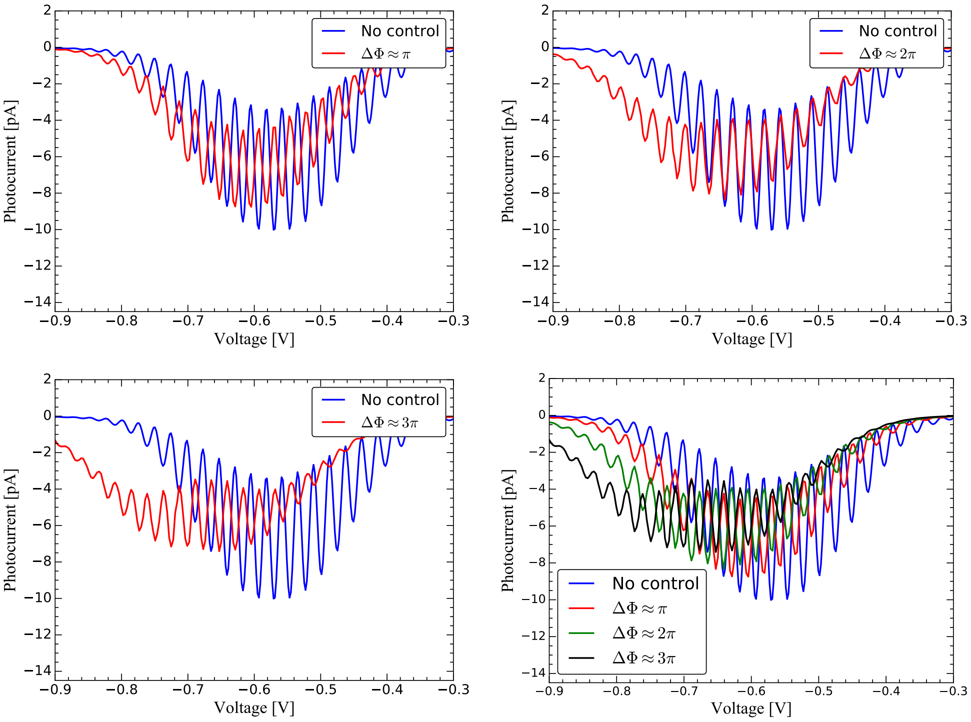

Figure 3.15.: Calculated photocurrent signals for amplitude jittered control pulses.

Based solely on model calculations, no final decision over the process underlying the experimentally observed loss of fringe contrast can be made. Basically any process that leads to a decoherence of the exciton TLS or randomized phase pickup between the optical pulses can potentially cause the loss of fringe contrast.

3.4. Modeling Rapid Adiabatic Passage in terms of a FLS[5]

Using the refined dressed state model introduced in the last section, theoretical calculations to understand the measurements of another experiment performed in the group of Prof. Dr. Artur Zrenner have been made. The given experiment is aimed at robust state preparation by so called rapid adiabatic passage (RAP) using a single optical pulse for the excitation. The basic phenomenon is quite well known in literature [88, 89, 90]. In general the term RAP is used to denote robust population transfer from one quantum state to another. As Greentree *et al.* [89] propose, the given states may even be spatially separated. The basic idea, at least for the considered experiment, can be summarized as follows. Given a transition between two states in a given quantum system, a time dependent detuning is imprinted to the given transition. In theory it does not make any difference whether the transition frequency between the two states or the frequency of the exciting field is varied. A key point is however, that at some point during interaction with the external field the system should be excited resonantly. On the left figure 3.16 shows an example of how the detuning may look in a pulsed experiment. In the sketched setup, the point of zero detuning has been chosen to coincide with the center of the excitation pulse.

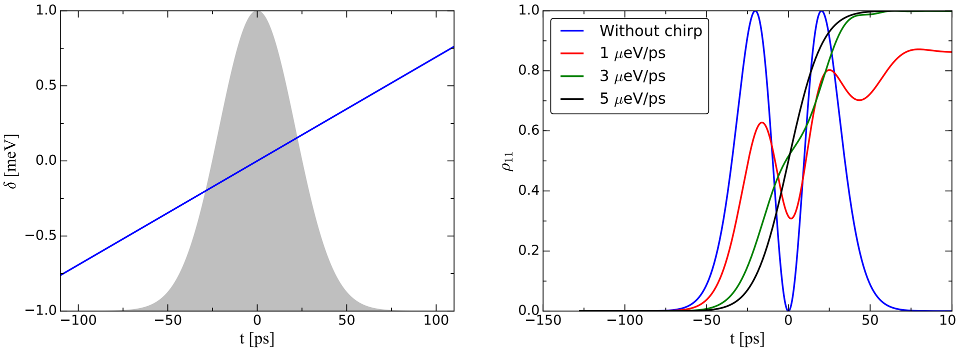

Figure 3.16.: Left: TLS detuning in a RAP experiment with zero detuning at the intensity maximum of the exciting laser pulse. The grey shaded area indicates the temporal intensity profile of the exciting laser pulse. Right: Time resolved exciton population for a 4π-pulse neglecting all decay and decoherence mechanisms.

On the right figure 3.16 shows the calculated time resolved exciton population considering a 4π-pulse while neglecting all decay and decoherence mechanisms. For the model introduced in the last section this means $\gamma_e = \gamma_r = \gamma_{hh} \equiv 0$. Without applied chirp the population shows the expected oscillation ending up in the ground state after the excitation is gone. With an applied linear chirp one observes a transition from the

---

[5] A joint publication with the group of Prof. Dr. Artur Zrenner is in preparation.

ground state to the excited state, but the chirp suppresses the population oscillations. In the sketched situation, application of a linear chirp with a slope of 5μeV/ps is sufficient to almost totally suppress the population oscillation and replace it by a smooth transition to the excited state.

In the considered experiment the two states of interest are the ground state consisting of an empty quantum dot and the excited state where the quantum dot is populated with a single exciton. The time dependent detuning is achieved by Stark tuning the quantum dot exciton resonance via an ultra fast electric control pulse at the gate contact of a Schottky diode[6]. Given a sufficiently strong laser pulse and a sufficiently fast passage of the detuning through resonance, one expects to find a robust preparation of the exciton state with respect to intensity fluctuations of the exciting light field.

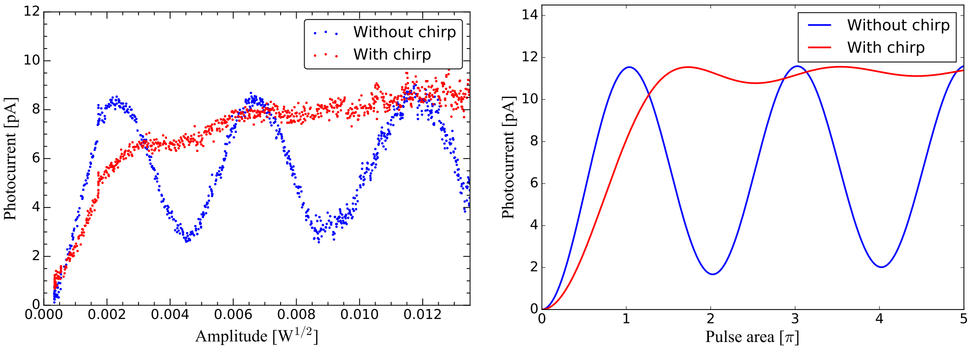

Figure 3.17.: Left: Photocurrent measurements of an electrically tuned quantum dot with and without applied chirp. Data have been kindly provided by the experimental group of Prof. Dr. Artur Zrenner, publication is in preparation. Right: Calculated photocurrent signal for pulse areas up to 5π

On the left side figure 3.17 shows the result of photocurrent measurements on the electrically tuned quantum dot, both with and without applied chirp. The measurements without applied chirp correspond to resonant excitation and show the expected oscillating behavior indicating Rabi oscillations of the exciton population. A somewhat counter-intuitive observation is that the photocurrent does not drop to zero at finite amplitudes. Applying the simple model that has already been used for the Ramsey experiment, this can be understood quite easily. In principle the photocurrent signal is nothing but the time integrated non-radiative decay of the excited state of the exciton TLS. Considering finite tunneling rates of electrons and holes, this decay starts as soon as the optical pulse has generated population in the excited state.

The right side of figure 3.17 shows the calculated photocurrent signal up to a pulse area of 5π with and without an applied chirp. The chirp has been chosen linear with

---

[6] Patent on the application of the electric chirp to the quantum dot submitted to DPMA on March 13, 2018

a slope of 1.5 μeV/ps and zero detuning at the center of the optical pulse. For the optical pulse a fixed width of 50 ps FWHI has been chosen. In order to achieve a finite photocurrent signal using the model introduced in the last section $\gamma_e = 1/400$ 1/ps, $\gamma_{hh} = 1$ 1/ns, and $\gamma_r = 0$ have been assumed. The finite value of γ_{hh} is needed for consistency. In case $\gamma_{hh} = 0$ had been assumed, the given system would not relax into its ground state, but into a state where $\rho_{hh} = 1$.

As can be seen, the qualitative agreement with the experimental data is quite good. In case of resonant excitation one observes Rabi oscillations of the photocurrent signal with finite signal at even multiples of π whereas in case of an applied chirp to the detuning of the TLS resonance one observes a well defined saturation behavior with only small signal fluctuations left in the saturated part of the curve. Quantitative agreement could not have been expected based on the simple model. However, before switching back to the realistic model with voltage dependent tunneling rates, the general dependence of the photocurrent signal on fundamental experimental parameters shall be examined. The focus of these studies lies on the robustness of the photocurrent signal.

The position of zero detuning is one of the first parameters which come to mind when asking this question. For further investigation Gaussian shaped laser pulses, centered at $t = 0$ with a width of 50 ps FWHI are assumed. A simple linear time dependence of the form

$$\delta(t) = m_c\,(t - T_c) \tag{3.62}$$

is assumed where T_c is the point of zero detuning. Assuming that the photocurrent signal is directly proportional to the electric field intensity at the time of zero detuning, one would expect a decreasing photocurrent signal for increasing absolute values of T_c. Figure 3.18 shows the photocurrent signal and the temporal intensity profile of the exciting laser pulse. Both curves have been normalized for easier comparison. As can be seen, the curves are almost identical despite the photocurrent curve being a little bit broader than the intensity curve. The broadening can be attributed to the finite spectral width of the laser pulse and the TLS resonance.

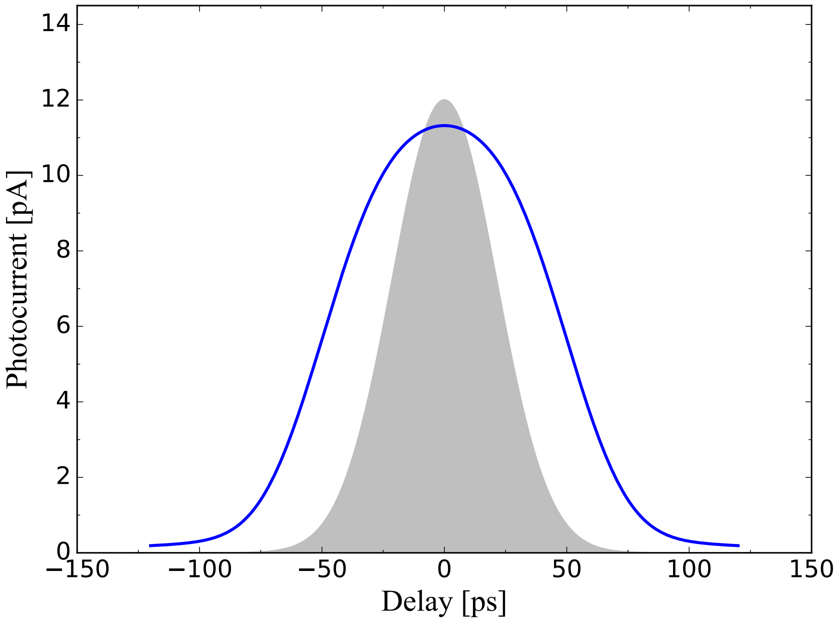

Figure 3.18.: Theoretical photocurrent signal depending on the time delay between the intensity maximum of the exciting laser pulse and the point of zero detuning from the TLS resonance.

Another interesting parameter is the energy range covered by the chirp. Increasing the slope of the chirp while keeping the point of zero detuning fixed at the maximum of the optical pulse, one should observe a smooth transition from a regime where the photocurrent signal is dominated by Rabi oscillations to a regime where it shows the desired saturation behavior. The origin of this transition is quite obvious. If the energy range covered by the chirp is smaller than the spectral width of the exciting laser pulse, the laser pulse has resonant components for its whole duration. Although the obtained photocurrent signal may vary from the situation of resonant excitation, one still expects oscillatory behavior depending on the pulse area. If, on the other hand, the energy range of the chirp is significantly bigger than the spectral range of the exciting laser pulse, the TLS is driven off-resonantly most of the time and one expects the photocurrent signal to be dominated by the RAP signature.

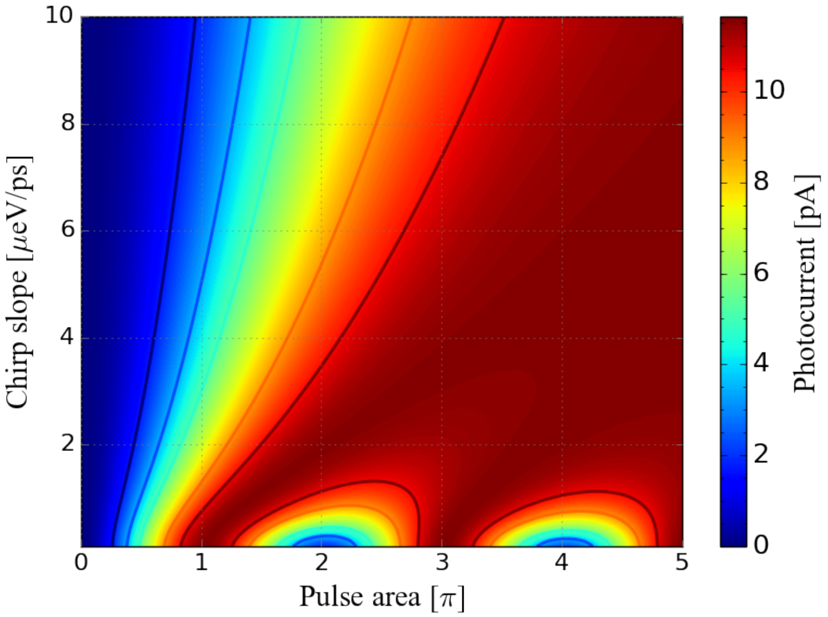

Figure 3.19.: Calculated photocurrent signal depending on the pulse area at constant temporal width of the exciting laser pulse and the slope of the chirp. Overlaid contour lines indicate of constant photocurrent, their color does not correspond to the color coded signal value.

Figure 3.19 shows the calculated photocurrent signal depending on pulse area of the exciting laser pulse and the maximum detuning of the TLS during the chirp. As expected, the photocurrent signal shows a smooth transition from Rabi oscillations to RAP. In addition one observes a shift of the saturation threshold towards larger pulse areas for increasing chirp slope[7]. Although it might not have been obvious in the initial consideration, this phenomenon can be understood quite easily. At higher chirp slopes the time window in which the optical pulse is resonant with the exciton resonance is shorter than at smaller chirp slopes. This shorter time window then requires stronger optical pulses to generate the exciton.

A point which has not been addressed so far is the dependence on the length of the optical pulse. When using an electric chirp, the optical pulse and the electric control pulse have to be synchronized to obtain the desired RAP effect. In order to make the synchronization easier, typical excitation pulses used in experiment exhibit a FWHI of ~50-100 ps. As the measured photocurrent signal generated by population decay of the excited state, there is no guarantee for a high population of the excited state given a high photocurrent signal, i.e. a high photocurrent signal does not guarantee that the population has been coherently inverted. To this end, the photocurrent signal

---

[7] In this context pulse area is equivalent to pulse amplitude.

has been calculated over a fixed range of optical pulse amplitudes and FWHI, in order to identify parameter intervals giving coherent population inversion.

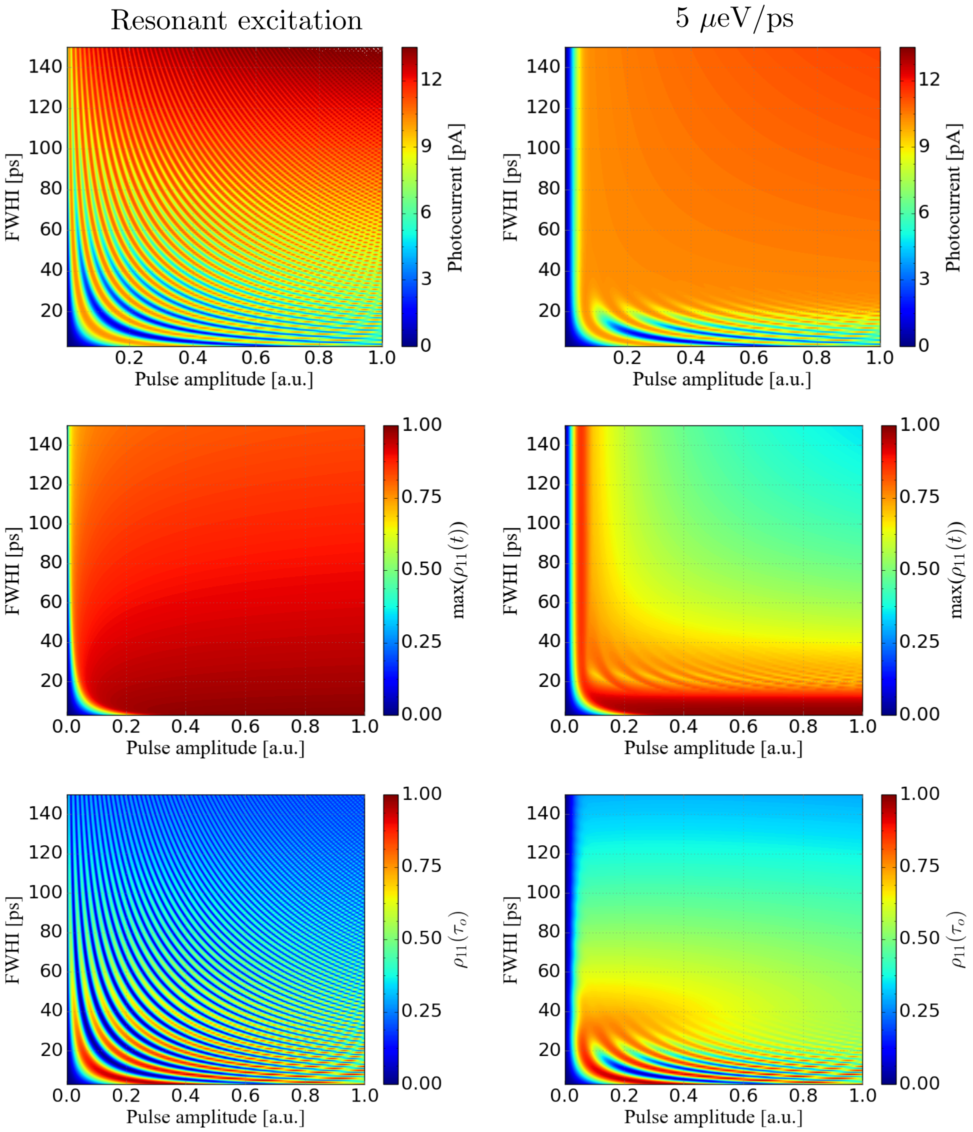

Figure 3.20.: Calculated photocurrent signal depending on the amplitude and width of the optical pulse considering linear detuning chirps with fixed slopes. Left: No chirp, i.e. resonant excitation. Right: 5 μeV/ps

In the top row, figure 3.20 shows the calculated photocurrent signal depending on the amplitude and width of the optical pulses both with and without applied electric control pulse. In case of resonant excitation one observes the expected Rabi oscillations, showing a clear dependence on both the amplitude and the width of the exciting laser pulse. For higher pulse widths, the oscillations get faster and loose contrast, i.e. the signal is starting to get more and more uniform. In case of an applied electric control pulse, the calculated photocurrent signal shows a smooth transition from an oscillating regime to a regime with quick saturation of the signal level. This transition has already been discussed in context of the slope dependence for the electric chirp. The main argument of finite temporal overlap of the exciting laser pulse and the TLS resonance stays the same. In this case, however, the temporal overlap is changed by changing the width of the optical pulse while keeping the slope of the chirp constant. In comparison to the previously shown results, one finds a more or less universal threshold pulse amplitude at which the RAP saturation occurs. However, as already mentioned, the photocurrent signal on its own may be misleading since it is basically a time integrated population decay. The middle row of figure 3.20 shows the maximum population of the excited state for the same pulse parameters as for the calculated photocurrent signal. Comparison of the maximum population of the excited state and the photocurrent signal, confirms that there is no strict correlation between the obtained photocurrent signal and the achieved maximum population of the excited state. However, for the given model parameters the calculations indicate that the system dynamics get more and more incoherent at larger pulse amplitudes for optical pulses with an FWHI larger than 60 ps. Considering the robustness of the population inversion, the achieved maximum population is no good measure either, because the optical pulse might also depopulate the system after causing a relatively high maximum population. In order to get a better measure, the bottom row figure 3.20 shows the population at $t = \tau_o$, i.e. roughly 0.5 FWHM after the pulse maximum. Comparing these data with the photocurrent signal, one finds a much better correspondence of density data and the photocurrent signal. Taking the population at $t = \tau_o$ as a measure, the calculated data suggest a relatively small parameter window around the amplitude 0.1 and a FWHI of 50 ps if one aims for a high population inversion without significant fluctuations on a changing pulse amplitude. Incoherent dynamics arise when the length of the excitation pulse gets close of even bigger than the decoherence and population decay times. To this end, in order to check whether a better population control can be achieved, the simulations have been repeated with γ_e=1/420 ps and γ_r=0. Figure 3.21 shows the respective results.

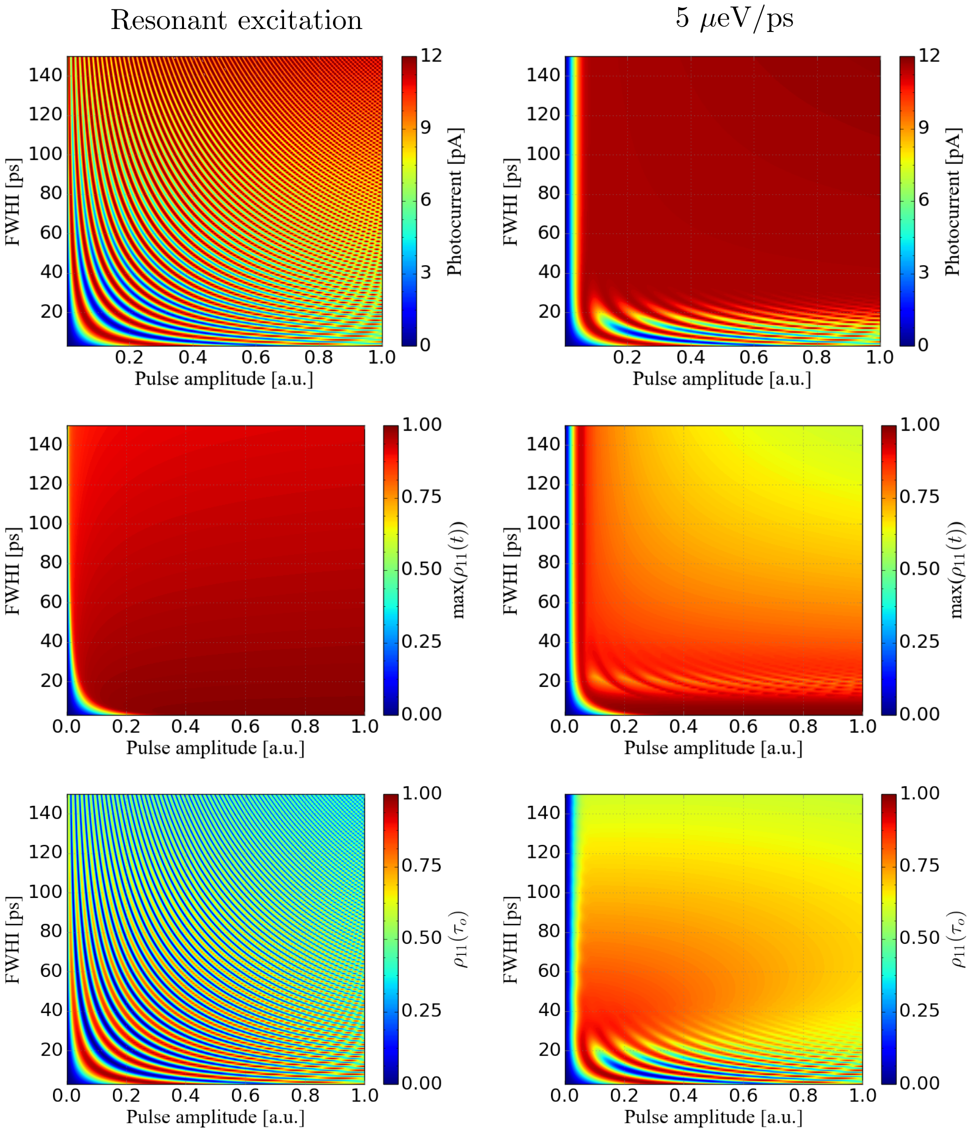

Figure 3.21.: Calculated photocurrent signals and densities depending on the amplitude and width of the optical pulse with T_1=420 ps. Top row: Photocurrent signal. Middle row: Maximum population of the excited state during the simulation. Bottom row: Population of the excited state at $t = \tau_o$.

Figure 3.22 shows the population of the excited state at $t = \tau_o$ for a pulse width of 40 ps FWHI for chirped excitation using fixed and dynamic tunneling rates compared to the population for resonant excitation. While the signal for resonant excitation shows a more or less rapid oscillation, the density for both fixed and dynamic tunneling rates is rather robust and does not show a significant decrease on the amplitude interval [0.07,0.25]. Beyond the amplitude of 0.25 a significant decrease of the achieved population is observable. Although the achieved exciton population of ~ 0.7 for the dynamic tunneling rates might seem suboptimal, the achieved robustness is quite promising. As has been shown by the additional calculations, decreased tunneling rates may push the achieved population well above 0.8.

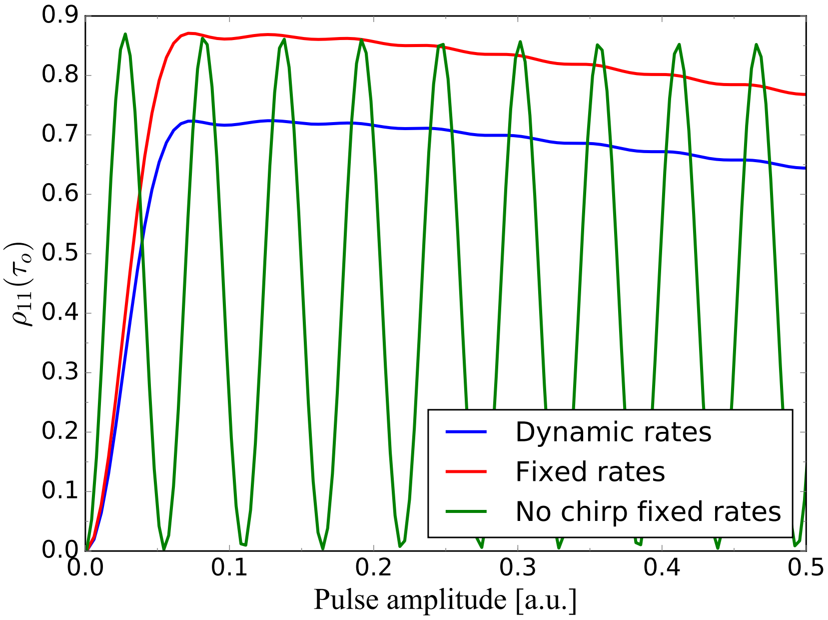

Figure 3.22.: Calculated photocurrent signals at a pulse width of 40 ps FWHI.

3.4.1. Dynamics of a four level system

The systems considered so far could be modeled rather properly in terms of an exciton TLS with additional states which are not coupled radiatively or via Coulomb interaction. Furthermore the optical and Coulomb matrix elements determined from the $\boldsymbol{k} \cdot \boldsymbol{p}$ eigenstates have been set rather unreflected until now. The simplest system with changed dynamics due to Coulomb interaction that one can think of is a four level system. The considered system consists of two initially populated and two empty states. As only two electrons are considered, the hierarchy of equations of motion is naturally truncated at the level of four point quantities. Among the four point quantities there is a special subset of operator products of the form

$$a_i^\dagger a_j^\dagger a_j a_i$$

where both indices i and j correspond to excited, i.e. initially unpopulated states, which can be interpreted as biexciton densities. Until now dynamics have been calculated on a rather phenomenological level where exciton binding energies have been assumed to included in the transition energy of a given TLS and proper excitation has been modeled by directly setting time dependent values of the Rabi frequency Ω. In this section the optical and dipole matrix elements calculated for the lens shaped quantum dot with a trumpet shaped Indium content will be used to model the optical absorption at the fundamental gap of the quantum dot system. In order to accomplish this, the matrix elements for the two s-like hole eigenstates and the two s-like electron eigenstates have been extracted from the results presented in 2.6.3. The extracted matrix elements and eigenvalues have been used as input for the generated equations of motion. For these calculations a phenomenological damping has been employed with a decay rate of $\gamma = 10^{-6}$/fs per polarization factor where polarization factors are considered as operator products of the form $a_i^\dagger a_j$ with $i \neq j$. Density factors with $i = j$ are damped with 2γ. For example the screened polarization $a_1^\dagger a_2^\dagger a_2 a_3$ would be damped with $3\gamma = 2\gamma + 1\gamma$ since it contains a density factor and a polarization factor.

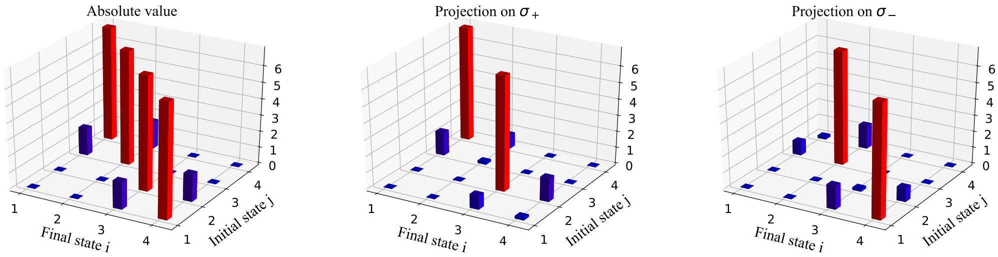

Figure 3.23.: Dipole matrix elements extracted from the output for the lens shaped quantum dot with trumpet shaped Indium content.

Figure 3.23 shows the extracted optical matrix elements. As before scaled versions of the optical matrix elements are shown. In this case, however, the diagonal 2 × 2 blocks vanish exactly since the respective states are degenerate such that a transition between these states cannot be accomplished by optical fields. As can be seen from the graphs only two transitions can be effectively accomplished via left- or right-circularly polarized light respectively. For each of the two polarizations one transition has its final state among the hole eigenstates and one has its final state among the electron states. As such one can expect to find the optical selection rules known from experiment, i.e. the quantum dot will preferably emit circularly polarized light if it is prepared in a state with a single exciton. Accordingly, the aforementioned biexciton densities should not be excited if circularly polarized excitation is considered.

Subsets of the extracted Coulomb matrix elements are shown in figure 3.24. Of course, considering only the four states closest to the gap, one should not expect to find exciton or biexciton binding energies which come close to experimentally determined values, especially since no dielectric or dynamic screening effects have been taken into account on determination of the Coulomb matrix elements. With a correct implementation of the equations of motion one should, however, observe a single resonance in case of circularly polarized excitation and a second resonance at a shifted energy in case of linearly polarized excitation.

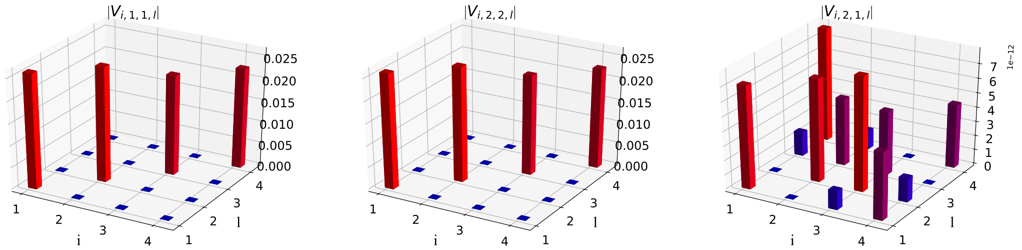

Figure 3.24.: Selected subsets of the Coulomb matrix elements extracted from the output for the lens shaped quantum dot with trumpet shaped Indium content.

Figure 3.25 shows the normalized absolute value of the calculated xx-component of what is referred to as susceptibility tensor within the scope of this work, for both linear and $\boldsymbol{\sigma}_+$ polarized excitation. To be more precise, the quantity $\chi_{\nu\mu}$ is defined as follows within this context.

$$\chi_{\nu\mu}(\hbar\omega) = \frac{P_\nu(\hbar\omega)}{E_\mu(\hbar\omega)} \tag{3.63}$$

Depending on the actual application, but especially in the context of wave mixing experiments, one may find different definitions in literature, see for example [91]. As can be seen, there is an additional resonance appearing around -4.5 meV for the case of linear polarized excitation which is not present in case of circular polarization. For

$\boldsymbol{\sigma}_+$ polarized excitation one observes only a very small signal peak around this energy. As the observed signal level is rather low, resonant response can be definitely ruled out in this case. To check whether this additional resonance really corresponds to a biexciton-like state, calculations with varying pulse amplitudes of the excitation pulse have been carried out. For a biexciton one should observe a vanishing signal weak excitation pulses. Furthermore, compared to the fundamental resonance, the biexciton resonance should exhibit Rabi oscillations at a smaller frequency. The results of these calculations are shown in 3.26. As expected, the additional resonance present for linear polarization does not show up in the color map for $\boldsymbol{\sigma}_+$ polarization. The fundamental resonance undergoes several oscillations on the considered amplitude interval. In case of linear polarization one observes a dim line around -4.5 meV in the color map. This line shows oscillating behavior with respect to the pulse amplitude as well, but with a much smaller frequency than the fundamental resonance.

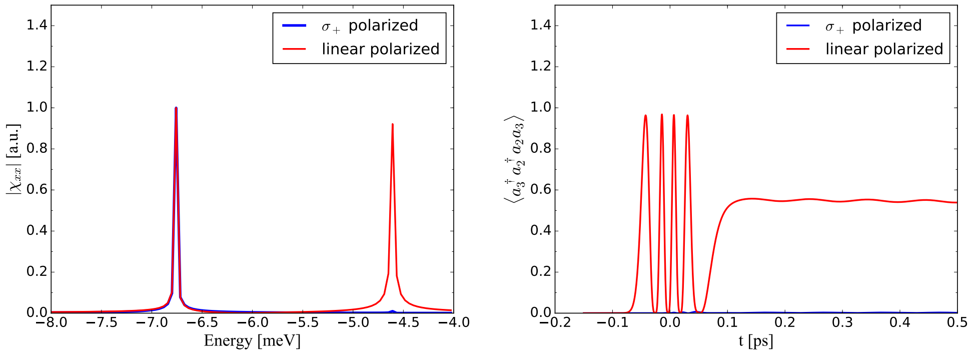

Figure 3.25.: Comparison of normalized χ_{xx} and $\left\langle a_3^\dagger a_2^\dagger a_2 a_3 \right\rangle$ for linear and $\boldsymbol{\sigma}_+$ polarized excitation.

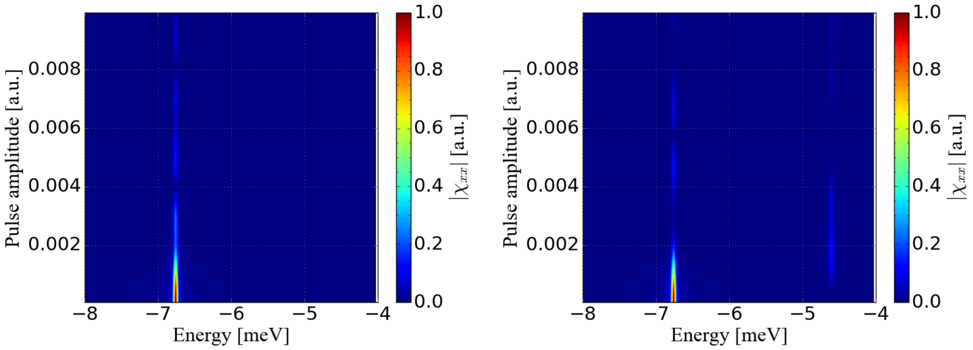

Figure 3.26.: Normalized xx-component of the susceptibility tensor for varying amplitudes of the exciting laser pulse. Left: $\boldsymbol{\sigma}_+$ polarization. Right: Linear polarization.

4. Summary and Outlook

In the first part of this work different semiconductor quantum dot systems have been investigated within the $\boldsymbol{k} \cdot \boldsymbol{p}$ framework. There it has been shown that the geometry and exact material composition of the quantum dots can have significant effects on the optical matrix elements. Also for some of the Coulomb matrix elements including indices corresponding to electron states further apart from the band gap are significantly reduced if inhomogeneous material compositions are considered instead of a homogeneous quantum dot. It has further been shown that modeling a quantum dot system embedded within a Schottky diode within $\boldsymbol{k} \cdot \boldsymbol{p}$ theory is a nontrivial task since the applied potential difference may lead to an energetic reordering of the calculated eigenstates. Calculating a consistent set of basis states for density matrix calculations gets a numerically demanding task since at larger potential differences a growing number of eigenstates is needed to retrieve all the eigenstates that have been calculated without applied potential difference. While this does not pose a general restriction on the determination of more realistic matrix elements for density matrix calculations, it renders treatment of systems with a moderately large number of eigenstates infeasible, especially if systems with applied potential differences are considered.

The second part of the thesis was dedicated to density matrix calculations to get a better understanding of different experiments. First a Ramsey-type experiment has been modeled to show that coherent phase control of an exciton FLS is possible within the decoherence time of the TLS. In addition, time and amplitude jitter on the applied electric control pulses have been demonstrated to cause loss of fringe contrast in calculated fringe patterns. Based on the needed magnitude of the amplitude jitter this mechanism can be almost certain ruled out as the viable candidate to explain loss of contrast in experiment. Secondly an experiment aimed at population inversion by RAP has been modeled. It has been shown that the photocurrent has a strong dependence on the point of zero detuning during the optical pulse. Furthermore a smooth transition from a regime dominated by Rabi oscillations to a regime with adiabatic population transfer with increasing slope of the electric chirp has been shown. The generated exciton population has been shown to be fairly robust against intensity fluctuations over a relatively broad intensity interval where an experiment with resonant excitation would have undergone several Rabi oscillations. Within the used model, the achieved exciton population has been proven to be limited by the tunneling rates. Although the achieve populations are below 90%, the shown robustness of the generated population against intensity fluctuations within this experiment makes it an interesting candidate for further improvement. As the performed calculations indicate, reduction of the optical pulse length with simultaneous increase of the chirp slope could push the generated population further up.

In the last part of the thesis a connection between the first and the second part has been set up by calculating the absorption of a four level system based on the optical and Coulomb matrix elements extracted from the $\boldsymbol{k} \cdot \boldsymbol{p}$ eigenstates. The calculations have shown, that these matrix elements qualitatively resemble optical selection rules observed in experiment. Considering the calculated energy shift of the biexciton resonance, quantitative agreement could not be expected since only four states have been considered for the calculation. While it may be justified to neglect the electron states at energies further apart from the fundamental gap since these states are not excited at the considered frequencies, the neglected hole eigenstates are initially populated with electrons and will certainly have an influence on the calculated spectra. Furthermore no screening effects have been taken into account on calculation of the Coulomb matrix elements. As a consequence single Coulomb matrix elements are probably overestimated in the current calculations. In order to account for the neglected occupied electron states the number of calculated hole eigenstates in the $\boldsymbol{k} \cdot \boldsymbol{p}$ calculations would have to be increased until no more localized hole eigenstates are found. This would, however, still not account for occupied electron states in the surrounding semiconductor matrix.

A. Third party software

The following table lists the third party software packages directly used within this work. Individual software packages or libraries may depend on other software/libraries to function properly. The reader is referred to the respective documentation pages for further information about eventually used software packages.

Software	Purpose	License
nextnano++	Calculation of the eigenenergies and eigenstates of given semiconductor heterostructures	commercial[1]
SymPy	Derivation of symbolic equations of motion and code generation	BSD
fftw3	Calculation of absorption spectra	GPL-2+
Matplotlib	Visualization of calculated data	PSF[2]
Numpy	Direct and indirect use by using Matplotlib	free software[3]
ParaView	Visualization of 3D wavefunctions	free software[4]
gcc	Compilation of the C/C++ based parts of the code	GPL
amgcl	Solution of sparse linear systems on calculation of the CMEs	MIT license

Table A.1.: Third party software packages and libraries directly used in this work

---

[1] See documentation for used 3rd party software

[2] Licensed under PSF license, further details at `https://matplotlib.org/users/license.html`

[3] Licensed according to `http://www.numpy.org/license.html` (3-Clause BSD)

[4] ParaView itself is licensed under BSD license, but relies on 3rd party packages with different licenses. See `https://www.paraview.org/paraview-license/` for details.

B. Projections of the quantum dot eigenstates onto the bulk eigenstates

no.	cb+	cb-	hh+	lh+	lh-	hh-	so+	so-	sum
1	0.005	0.002	0.388	0.272	0.175	0.092	0.022	0.044	0.044
2	0.002	0.005	0.092	0.175	0.272	0.388	0.044	0.022	0.022
3	0.005	0.002	0.382	0.321	0.127	0.106	0.016	0.042	0.042
4	0.002	0.005	0.106	0.127	0.321	0.382	0.042	0.016	0.016
5	0.004	0.002	0.368	0.320	0.121	0.132	0.017	0.037	0.037
6	0.002	0.004	0.132	0.121	0.320	0.368	0.037	0.017	0.017
7	0.004	0.002	0.335	0.226	0.213	0.168	0.023	0.029	0.029
8	0.002	0.004	0.168	0.213	0.226	0.335	0.029	0.023	0.023
9	0.032	0.921	0.001	0.006	0.012	0.017	0.007	0.004	0.004
10	0.921	0.032	0.017	0.012	0.006	0.001	0.004	0.007	0.007
11	0.158	0.772	0.005	0.010	0.011	0.027	0.012	0.004	0.004
12	0.772	0.158	0.027	0.011	0.010	0.005	0.004	0.012	0.012
13	0.757	0.172	0.027	0.011	0.011	0.006	0.005	0.011	0.011
14	0.172	0.757	0.006	0.011	0.011	0.027	0.011	0.005	0.005
15	0.693	0.237	0.012	0.027	0.012	0.004	0.008	0.007	0.007
16	0.237	0.693	0.004	0.012	0.027	0.012	0.007	0.008	0.008

Table B.1.: Projections of the eigenstates of an ellipsoidal quantum dot onto the bulk eigenstates.

no.	cb+	cb-	hh+	lh+	lh-	hh-	so+	so-
1	0.005	0.002	0.549	0.085	0.072	0.250	0.015	0.015
2	0.002	0.005	0.250	0.072	0.085	0.549	0.022	0.022
3	0.002	0.004	0.320	0.059	0.066	0.525	0.013	0.013
4	0.004	0.002	0.525	0.066	0.059	0.320	0.010	0.010
5	0.006	0.001	0.729	0.066	0.037	0.139	0.008	0.008
6	0.001	0.006	0.139	0.037	0.066	0.729	0.013	0.013
7	0.000	0.005	0.002	0.010	0.038	0.936	0.005	0.005
8	0.005	0.000	0.936	0.038	0.010	0.002	0.004	0.004
9	0.822	0.106	0.014	0.032	0.008	0.002	0.010	0.010
10	0.106	0.822	0.002	0.008	0.032	0.014	0.007	0.007
11	0.741	0.170	0.023	0.026	0.013	0.005	0.010	0.010
12	0.170	0.741	0.005	0.013	0.026	0.023	0.011	0.011
13	0.558	0.353	0.018	0.022	0.017	0.012	0.010	0.010
14	0.353	0.558	0.012	0.017	0.022	0.018	0.011	0.011
15	0.138	0.762	0.006	0.014	0.024	0.033	0.015	0.015
16	0.762	0.138	0.033	0.024	0.014	0.006	0.009	0.009

Table B.2.: Projections of the eigenstates of a lens shaped quantum dot onto the bulk eigenstates.

no.	cb+	cb-	hh+	lh+	lh-	hh-	so+	so-
1	0.000	0.009	0.008	0.047	0.064	0.838	0.031	0.031
2	0.009	0.000	0.838	0.064	0.047	0.008	0.004	0.004
3	0.007	0.001	0.800	0.060	0.036	0.077	0.004	0.004
4	0.001	0.007	0.077	0.036	0.060	0.800	0.015	0.015
5	0.001	0.006	0.161	0.030	0.046	0.735	0.015	0.015
6	0.006	0.001	0.735	0.046	0.030	0.161	0.006	0.006
7	0.002	0.003	0.362	0.017	0.021	0.586	0.005	0.005
8	0.003	0.002	0.586	0.021	0.017	0.362	0.004	0.004
9	0.003	0.928	0.000	0.004	0.036	0.014	0.005	0.005
10	0.928	0.003	0.014	0.036	0.004	0.000	0.011	0.011
11	0.406	0.513	0.009	0.019	0.022	0.012	0.009	0.009
12	0.513	0.406	0.012	0.022	0.019	0.009	0.009	0.009
13	0.834	0.085	0.020	0.031	0.009	0.002	0.010	0.010
14	0.085	0.834	0.002	0.009	0.031	0.020	0.009	0.009
15	0.463	0.461	0.008	0.021	0.021	0.008	0.009	0.009
16	0.461	0.463	0.008	0.021	0.021	0.008	0.009	0.009

Table B.3.: Projections of the eigenstates of a lens shaped quantum dot neglecting piezoelectric charge densities onto the bulk eigenstates.

no.	cb+	cb-	hh+	lh+	lh-	hh-	so+	so-
1	0.009	0.000	0.833	0.063	0.048	0.012	0.004	0.004
2	0.000	0.009	0.012	0.048	0.063	0.833	0.031	0.031
3	0.005	0.003	0.561	0.052	0.044	0.317	0.008	0.008
4	0.003	0.005	0.317	0.044	0.052	0.561	0.011	0.011
5	0.007	0.000	0.857	0.049	0.027	0.039	0.004	0.004
6	0.000	0.007	0.039	0.027	0.049	0.857	0.017	0.017
7	0.002	0.002	0.474	0.019	0.019	0.474	0.004	0.004
8	0.002	0.002	0.474	0.019	0.019	0.474	0.004	0.004
9	0.000	0.930	0.000	0.004	0.036	0.014	0.005	0.005
10	0.930	0.000	0.014	0.036	0.004	0.000	0.011	0.011
11	0.007	0.912	0.000	0.007	0.034	0.021	0.008	0.008
12	0.912	0.007	0.021	0.034	0.007	0.000	0.010	0.010
13	0.155	0.764	0.004	0.011	0.029	0.019	0.009	0.009
14	0.764	0.155	0.019	0.029	0.011	0.004	0.010	0.010
15	0.077	0.851	0.001	0.007	0.035	0.012	0.006	0.006
16	0.851	0.077	0.012	0.035	0.007	0.001	0.012	0.012

Table B.4.: Projections of the eigenstates of a lens shaped quantum dot neglecting the wetting layer onto the bulk eigenstates.

no.	cb+	cb-	hh+	lh+	lh-	hh-	so+	so-
1	0.003	0.004	0.369	0.082	0.084	0.421	0.019	0.019
2	0.004	0.003	0.421	0.084	0.082	0.369	0.018	0.018
3	0.005	0.001	0.727	0.078	0.051	0.116	0.007	0.007
4	0.001	0.005	0.116	0.051	0.078	0.727	0.015	0.015
5	0.000	0.007	0.026	0.030	0.079	0.838	0.013	0.013
6	0.007	0.000	0.838	0.079	0.030	0.026	0.008	0.008
7	0.004	0.000	0.870	0.040	0.012	0.065	0.004	0.004
8	0.000	0.004	0.065	0.012	0.040	0.870	0.005	0.005
9	0.817	0.109	0.014	0.033	0.009	0.002	0.011	0.011
10	0.109	0.817	0.002	0.009	0.033	0.014	0.007	0.007
11	0.505	0.405	0.016	0.021	0.019	0.013	0.011	0.011
12	0.405	0.505	0.013	0.019	0.021	0.016	0.011	0.011
13	0.748	0.162	0.023	0.027	0.013	0.005	0.010	0.010
14	0.162	0.748	0.005	0.013	0.027	0.023	0.011	0.011
15	0.677	0.223	0.028	0.023	0.016	0.009	0.010	0.010
16	0.223	0.677	0.009	0.016	0.023	0.028	0.014	0.014

C. Implementation details

C.1. Implementation details for the EOM generator

As already mentioned in chapter 3.1 the program for generation of the FLS equations of motion is built on top of the SymPy library. In the current implementation the program starts with the FLS Hamiltonian in the form

$$\begin{aligned}
\hat{H} &= \hat{H}_0 + \hat{H}_{lm} + \hat{H}_C \\
\hat{H}_0 &= \sum_{m=0}^{N_s-1} \varepsilon_i a_m^\dagger a_m \\
\hat{H}_{lm} &= -\boldsymbol{E}(t) \cdot \frac{1}{2} \sum_{m,n=0}^{N_s-1} \boldsymbol{\mu}_{mn} a_m^\dagger a_n + \boldsymbol{\mu}_{nm} a_n^\dagger a_m \\
\hat{H}_C &= \frac{1}{2} \sum_{m,n,o,p} V_{mnop} a_m^\dagger a_n^\dagger a_o a_p
\end{aligned}$$

where N_s is the number of states in the system. Note that the factor 1/2 in front of the summation for the light-matter couplings is necessary to remove double counts since both summation indices run from 0 to $N_s - 1$. Using a modified implementation[1] of SymPy's fermion creation and annihilation operators the program starts with the general two-point coherence $\hat{O}_{ij} := a_i^\dagger a_j$, adds its general operator pattern $a^\dagger a$ to a list of known operator patterns and calculates the normal ordered form of the commutators

$$\left[\hat{O}_{ij}, \hat{H}_0\right], \left[\hat{O}_{ij}, \hat{H}_{lm}\right], \left[\hat{O}_{ij}, \hat{H}_C\right]$$

Whenever the normal ordered form of one of these commutators contains a currently unknown operator pattern[2] this pattern is added to a list of currently unknown operator patterns for which the equations of motion have to be determined as well while ensuring that the given pattern is valid and not already contained in the list of unknown patterns. In this context an operator pattern is considered valid if it's number of annihilation operators does not exceed the number of electrons in the system.

---

[1] The original implementation was not able to deal with indexed operators.

[2] Within the pure electron picture only the commutator with $\hat{H}_C$ can deliver unknown operator patterns.

After the first run for $\hat{O}_{ij}$ the program pops the first unknown operator pattern from the list of unknown patterns, adds it to the list of known operator patterns and calculates the normal ordered form of above commutators updating the list of unknown operator patterns. This procedure is repeated until there are no more elements in the list of unknown operator patterns.
The final form of the symbolic equations of motion for each operator pattern is then calculated as

$$\frac{d}{dt}\left\langle \hat{O}_{\bar{i}_N}\right\rangle = -\frac{i}{\hbar}\left(\left[\hat{O}_{\bar{i}_N}, \hat{H}_0\right] + \left[\hat{O}_{\bar{i}_N}, \hat{H}_{lm}\right] + \left[\hat{O}_{\bar{i}_N}, \hat{H}_C\right]\right)$$

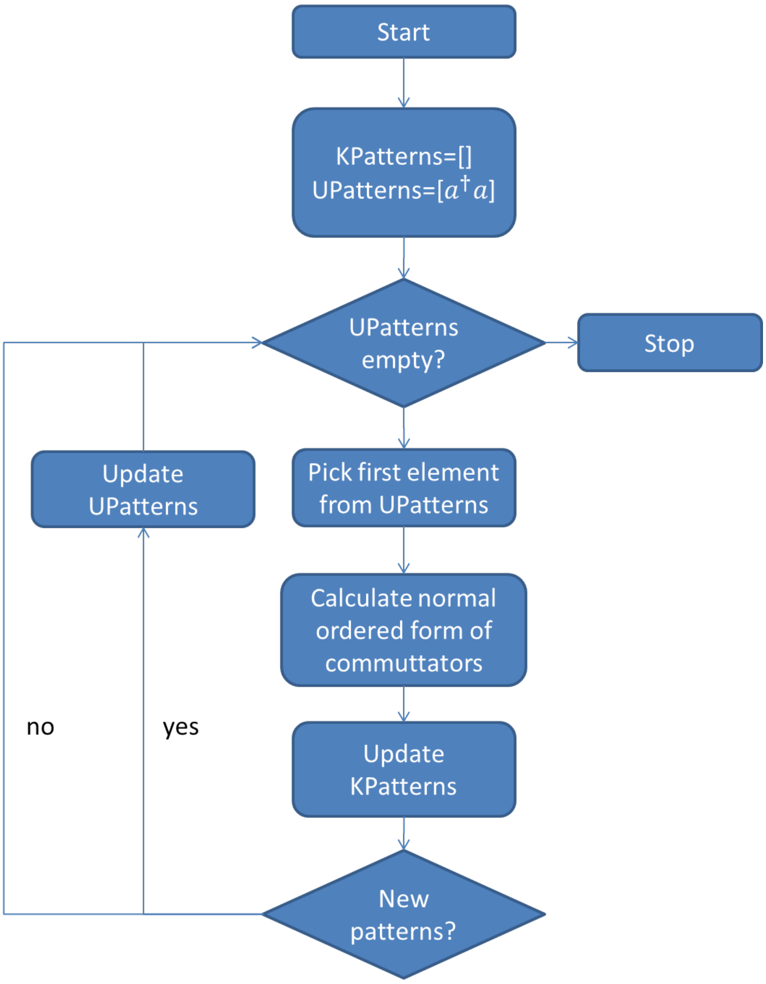

Figure C.1.: Flow chart of the algorithm to determine the symbolic equations of motion for the required N-point quantities.

Once the symbolic equations of motion for the relevant operator patterns are known the program starts generating auxiliary C++ code for setup of a FLS calculation. Here auxiliary means that only part of the simulation code is generated, namely the setup of the light-matter coupling terms and the Coulomb coupling terms since these are the only terms, at least within the pure electron picture, whose exact structure is hard to predict. Figure C.1 shows the flow chart of the implemented algorithm.

C.2. Implementation details for the code generator

Since, without further approximations, there is no analytical solution for the FLS equations of motion, they have to be solved numerically. For this purpose the backbone of a template class[3] has been implemented, providing fundamental functions to calculate the dynamics of a FLS under the influence of an external light field. The number of states in the FLS serves as the only template parameter, so this number has to be known at compile time.

Given the symbolic equations of motion generated by the EOM generator, most of the FLS setup code is autogenerated, namely top-level and low-level code to:

- set up and initialize the array for the reduced density matrix
- set up the light-matter coupling terms
- set up the Coulomb coupling terms

The procedure to set up and initialize the density matrix is pretty straight forward. The code generator extracts the valid operator patterns from the generated list of equations of motion. Then, for each appearing operator pattern, the program creates a map of valid operators of the form

$$\bar{i}_N \to n \qquad n \in \mathbb{N}$$

where $\bar{i}_N$ corresponds to a valid operator multi-index. As a reminder, a multi-index is considered valid if and only if the indices of all creation operators are pair-wise unequal and the indices of all annihilation operators are pair-wise unequal as well. Summing up the sizes of the individual maps one obtains the required size of the array for the reduced density matrix. Discarding the invalid operators one already drastically reduces the size of the reduced density matrix as well as the number of coupling terms which one would have had to examine for validity at run-time. For an additional performance gain the program exploits hermitian symmetries by discarding operators whose hermitian conjugate is already contained in the map of valid operators. Then, given the desired initial state of the system in number state representation, the program

---

[3] A template class was chosen since one still has the freedom to allow a variable number of single-particle eigenstates while allowing more aggressive compiler optimizations.

calculates the expectation values of the different operators as well as their expectation values with respect to the ground state of the system which is needed for the phenomenological damping terms. The expectation values with respect to the desired initial state of the system then serve as initial values for the reduced density matrix while the expectation values with respect to the ground state serve as equilibrium values.
Although, at least in principle, the procedure to set up the light-matter and Coulomb coupling terms is also quite straight forward, efficient implementation is a little bit more complicated since the SymPy library is not so good at collecting equivalent symbolic summations into a single symbolic summation, i.e. the symbolic light-matter interaction parts of the equations of motion contain different summations addressing the same operators, but with different summation indices. A naive one-to-one translation of the individual coupling terms would therefore result in a potentially large number of coupling terms addressing the same coupled operator. To overcome this problem, the light-matter and Coulomb coupling terms are set up in a two stage process for each valid operator.

1. Setup of coupling maps: Given a valid operator $\hat{O}_{\bar{\imath}_N}$ the program examines the symbolic coupling terms and converts the symbolic summations into explicit ones. Each of the coupling terms is then of the general form

$$a_{\bar{\jmath}_M} \left\langle \hat{O}_{\bar{\jmath}_M} \right\rangle$$

where $M = N$ for light-matter coupling terms and $M = N$ or $M = N + 2$ for Coulomb coupling terms and $a_{\bar{\jmath}_M}$ is a numeric prefactor depending on the respective coupling matrix element. The program now examines each of the explicit terms individually, keeping track of a coupling map of the form

$$\bar{\jmath}_M \to \alpha_{\bar{\jmath}_M}$$

If the current coupled operator is not contained within this map, the program adds the respective entry

$$\bar{\jmath}_M \to a_{\bar{\jmath}_M}.$$

If it is already contained in the map, the program just increments the mapped value by the value of $a_{\bar{\jmath}_M}$. In this way, at the end of stage one, for each operator one has the respective coupling map

$$\bar{\jmath}_M \to \alpha_{\bar{\jmath}_M} \qquad \alpha_{\bar{\jmath}_M} = \sum a_{\bar{\jmath}_M}.$$

2. Setup of coupling vectors: While, in principle, the coupling maps obtained in stage one, give the complete information for the individual operator couplings needed for numerical solution of the equations of motion, their actual use in numeric calculations has several drawbacks. The first and probably most severe one is memory consumption. Instead of addressing the coupled operators by their position in the reduced density matrix, they are addressed by their complete multi-index. The second drawback is a potential lack of performance. In the current implementation one has the guaranty of a unique mapping, i.e. every key, namely the multi-index, is contained once and only once in the mapping and has a single mapped value. However, the C++ standard does not put any restrictions on the internal memory layout of such maps. This means the map entries are not guaranteed to be placed at sequential addresses in memory which is a crucial requirement for efficient caching. As a consequence, depending on the implementation of the C++ core libraries, using maps might result in expensive memory look-ups during the time stepping[4]. The memory problem is however far more severe.

To solve this problem the program replaces the map structure by a respective coupling vector of the same size, containing key-value pairs of the form

$$(n, \alpha_n) \qquad n \in \mathbb{N}, \alpha_n \in \mathbb{C}$$

where the multi-index has been replaced by its offset in the array for the reduced density matrix which has been determined during setup of that array.

---

[4] Since maps are typically optimized for fast look-up of specific keys, the underlying data structure is most probably a binary search tree or a hash map.

C.3. False sharing problem in multi-threaded FLS-simulations

As already mentioned in the main part of the thesis, a naive parallelization of the Runge-Kutta integration for the FLS equations of motion yields worse performance than the single-threaded serial implementation. Part of the performance penalty may be attributed to the overhead introduced by spawning the individual threads at the beginning of the time integration and the need to synchronize these threads after each time step. A proper implementation of the OpenMP standard can, however, pretty much minimize this overhead by keeping the respective threads alive instead of deleting them after each time step.

A more subtle problem, called false sharing [92], is introduced by modern computer architectures. To be more precise, the problem stems from the need to maintain cache coherence among different CPUs in a multi-processor environment. Whenever a program reads the value from a specific address in memory, the hardware fetches not only the desired value, but a hole bunch of halo data which happens to fit on a so called cache line. When just reading values from an array with contiguous memory layout, this is quite desirable since caching reduces the number of accesses to main memory which is quite slow. Assuming that one wants to read from an array called A, the fetched cache line might schematically represented as in figure C.2.

Figure C.2.: Schematic representation of the prefetched cache line when reading from an array with contiguous memory layout. The exact number of elements fitting on a single cache line are determined by A's underlying data type and the hardware size of a cache line.

As long as the program instructions involve only read operations on the contents of A, the number of threads which can access A in parallel is only limited by the total number of threads supported by the system. On a multi-core platform one may face the situation when two processors hold a copy of the exact same cache line as depicted in figure C.3. This is usually the case, when two independent threads executing on different processors happen to read from or write to adjacent elements of the same array. While read operations are still unproblematic, the situation gets complicated, when both threads happen to perform write operations. In order to get deterministic results on multi-core platform, the hardware needs to maintain cache coherence, i.e. once one of the two threads performs a write operation on the contents of the cache line, the entire cache line is marked 'dirty' on all other CPU's forcing a reload of that line once it was written back to memory by the thread modifying it in the first place.

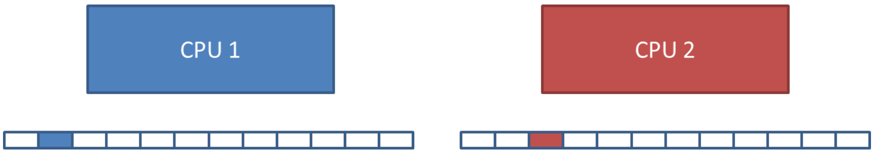

Figure C.3.: Schematic representation of the case when two threads executing on different CPUs each hold a copy of the exact same cache line and access adjacent, but otherwise independent elements of that cache line.

A straight forward implementation of the RK-4 algorithm uses temporary arrays to hold the derivatives. The number of temporary arrays is somewhat irrelevant for the current discussion. However, a construct frequently appearing when performing RK-4 integration on a system of equations may look as follows:

```
int i,j;
for(i=0;i<NumEqs;i++){
  dy[i]=std::complex<double>(0.,0.);
  for(j=0;j<NumRHSTerms;j++){
    dy[i]+=RHS_Term(i,j);
  }
}
```

with a straight forward OpenMP parallelized form given by

```
int i,j;
#pragma omp parallel for private(i,j)
for(i=0;i<NumEqs;i++){
  dy[i]=std::complex<double>(0.,0.);
  for(j=0;j<NumRHSTerms;j++){
    //Possibly false sharing
    dy[i]+=RHS_Term(i,j);
  }
}
```

where RHS_Term just serves as a place holder for an arbitrary term appearing on the right hand side of the respective equation of motion. As indicated by the comment in the code, the update of dy[i] might cause false sharing problems in case dy happens to exhibit contiguous memory layout.

There are several ways to circumvent the false sharing problem. First one could scatter the contents of dy in memory such that no adjacent elements of dy happen to reside on the same cache line. This would then lead to new performance issues due to lots of cache misses in other parts of the Runge-Kutta loop. As another possibility one could divide the temporary arrays into chunks ensuring that the respective chunks reside on different cache lines. Individual threads could then work on the independent chunks. This would, however, result in highly platform dependent code since memory layout and the size of a cache line may vary from platform to platform. The perhaps most promising solution to the false sharing problem is introducing a thread-local temporal variable which is used to accumulate the value of the derivative. Once the final value of a given derivative is known, the respective element of dy is updated.

```
int i,j;
std::complex<double> tmp;
#pragma omp parallel for private(i,j,tmp)
for(i=0;i<NumEqs;i++){
  tmp=std::complex<double>(0.,0.);
  for(j=0;j<NumRHSTerms;j++){
    //No more false sharing since every thread
    //has its own tmp variable
    tmp+=RHS_Term(i,j);
  }
  dy[i]=tmp;
}
```

As the number of write operations to dy is now greatly reduced, the needed number of reloads to maintain cache coherence is reduced accordingly, resulting in a more performant program.

Bibliography

[1] D. Loss and D. P. DiVincenzo. Quantum computation with quantum dots. *Phys. Rev. A*, 57:120–126, Jan 1998.

[2] S.-S. Li, J.-B. Xia, J.-L. Liu, F.-H. Yang, Z.-C. Niu, S.-L. Feng, and H.-Z. Zheng. Inas/gaas single-electron quantum dot qubit. *Journal of Applied Physics*, 90(12):6151–6155, 2001.

[3] R. M. Stevenson, R. M. Thompson, A. J. Shields, I. Farrer, B. E. Kardynal, D. A. Ritchie, and M. Pepper. Quantum dots as a photon source for passive quantum key encoding. *Phys. Rev. B*, 66:081302, Aug 2002.

[4] D. Fattal, E. Diamanti, K. Inoue, and Y. Yamamoto. Quantum teleportation with a quantum dot single photon source. *Phys. Rev. Lett.*, 92:037904, Jan 2004.

[5] Z. Shi, C. B. Simmons, J. R. Prance, J. K. Gamble, T. S. Koh, Y.-P. Shim, X. Hu, D. E. Savage, M. G. Lagally, M. A. Eriksson, M. Friesen, and S. N. Coppersmith. Fast hybrid silicon double-quantum-dot qubit. *Phys. Rev. Lett.*, 108:140503, Apr 2012.

[6] M. Veldhorst, J. C. C. Hwang, C. H. Yang, A. W. Leenstra, B. de Ronde, J. P. Dehollain, J. T. Muhonen, F. E. Hudson, K. M. Itoh, A. Morello, and A. S. Dzurak. An addressable quantum dot qubit with fault-tolerant control-fidelity. *Nature Nanotechnology*, 9:981 EP –, 10 2014.

[7] E. Moreau, I. Robert, J. M. Grard, I. Abram, L. Manin, and V. Thierry-Mieg. Single-mode solid-state single photon source based on isolated quantum dots in pillar microcavities. *Applied Physics Letters*, 79(18):2865–2867, 2001.

[8] C. Santori, M. Pelton, G. Solomon, Y. Dale, and Y. Yamamoto. Triggered single photons from a quantum dot. *Phys. Rev. Lett.*, 86:1502–1505, Feb 2001.

[9] Z. Yuan, B. E. Kardynal, R. M. Stevenson, A. J. Shields, C. J. Lobo, K. Cooper, N. S. Beattie, D. A. Ritchie, and M. Pepper. Electrically driven single-photon source. *Science*, 295(5552):102–105, 2002.

[10] M. Pelton, C. Santori, J. Vučković, B. Zhang, G. S. Solomon, J. Plant, and Y. Yamamoto. Efficient source of single photons: A single quantum dot in a micropost microcavity. *Phys. Rev. Lett.*, 89:233602, Nov 2002.

[11] S. Buckley, K. Rivoire, and J. Vukovi. Engineered quantum dot single-photon sources. *Reports on Progress in Physics*, 75(12):126503, 2012.

[12] D. Heinze, D. Breddermann, A. Zrenner, and S. Schumacher. A quantum dot single-photon source with on-the-fly all-optical polarization control and timed emission. *Nature Communications*, 6:8473 EP –, 10 2015.

[13] T. M. Stace, G. J. Milburn, and C. H. W. Barnes. Entangled two-photon source using biexciton emission of an asymmetric quantum dot in a cavity. *Phys. Rev. B*, 67:085317, Feb 2003.

[14] R Mark Stevenson, Robert J Young, Paola Atkinson, Ken Cooper, David A Ritchie, and Andrew J Shields. A semiconductor source of triggered entangled photon pairs. *Nature*, 439(7073):179, 2006.

[15] N. Akopian, N. H. Lindner, E. Poem, Y. Berlatzky, J. Avron, D. Gershoni, B. D. Gerardot, and P. M. Petroff. Entangled photon pairs from semiconductor quantum dots. *Phys. Rev. Lett.*, 96:130501, Apr 2006.

[16] R Hafenbrak, S M Ulrich, P Michler, L Wang, A Rastelli, and O G Schmidt. Triggered polarization-entangled photon pairs from a single quantum dot up to 30k. *New Journal of Physics*, 9(9):315, 2007.

[17] S. Schumacher, J. Förstner, A. Zrenner, M. Florian, C. Gies, P. Gartner, and F. Jahnke. Cavity-assisted emission of polarization-entangled photons from biexcitons in quantum dots with fine-structure splitting. *Opt. Express*, 20(5):5335–5342, Feb 2012.

[18] E. del Valle. Distilling one, two and entangled pairs of photons from a quantum dot with cavity qed effects and spectral filtering. *New Journal of Physics*, 15(2):025019, 2013.

[19] Naoto Kumagai, Shunsuke Ohkouchi, Masayuki Shirane, Yuichi Igarashi, Masahiro Nomura, Yasutomo Ota, Shinichi Yorozu, Satoshi Iwamoto, and Yasuhiko Arakawa. Effects of growth temperature of partial gaas cap on inas quantum dots in in-flush process for single dot spectroscopy. *physica status solidi c*, 8(2):248–250, 2011.

[20] J. G. Keizer, M. Bozkurt, J. Bocquel, T. Mano, T. Noda, K. Sakoda, E. C. Clark, M. Bichler, G. Abstreiter, J. J. Finley, W. Lu, T. Rohel, H. Folliot, N. Bertru, and P. M. Koenraad. Shape control of quantum dots studied by cross-sectional scanning tunneling microscopy. *Journal of Applied Physics*, 109(10):102413, 2011.

[21] A. Schramm, T. Kipp, F. Wilde, J. Schaefer, Ch. Heyn, and W. Hansen. Shape transformation of self-assembled inas quantum dots during overgrowth with alas. *Journal of Crystal Growth*, 289(1):81 – 88, 2006.

[22] T.-P. Hsieh, H.-S. Chang, W.-Y. Chen, W.-H. Chang, T. M. Hsu, N.-T. Yeh, W.-J. Ho, P.-C. Chiu, and J.-I. Chyi. Growth of low density ingaas quantum dots for single photon sources by metalorganic chemical vapour deposition. *Nanotechnology*, 17(2):512, 2006.

[23] W.-H. Chang, W.-Y. Chen, H.-S. Chang, T.-P. Hsieh, J.-I. Chyi, and T.-M. Hsu. Efficient single-photon sources based on low-density quantum dots in photonic-crystal nanocavities. *Phys. Rev. Lett.*, 96:117401, Mar 2006.

[24] B. L. Liang, Zh. M. Wang, J. H. Lee, K. Sablon, Yu. I. Mazur, and G. J. Salamo. Low density inas quantum dots grown on gaas nanoholes. *Applied Physics Letters*, 89(4):043113, 2006.

[25] N. Sharma and D. Reuter. A modified gradient approach for the growth of low-density inas quantum dot molecules by molecular beam epitaxy. *Journal of Crystal Growth*, 477(Supplement C):225 – 229, 2017. Proceeding of the 19th International Conference on Molecular Beam Epitaxy.

[26] M. Scheibner, M. Yakes, A. S. Bracker, I. V. Ponomarev, M. F. Doty, C. S. Hellberg, L. J. Whitman, T. L. Reinecke, and D. Gammon. Optically mapping the electronic structure of coupled quantum dots. *Nature Physics*, 4:291 EP –, 02 2008.

[27] Norman F. Ramsey. A molecular beam resonance method with separated oscillating fields. *Phys. Rev.*, 78:695–699, Jun 1950.

[28] A. Widhalm, A. Mukherjee, S. Krehs, N. Sharma, P. Kölling, A. Thiede, D. Reuter, J. Förstner, and Artur Zrenner. Ultrafast electric phase control of a single exciton qubit. *Applied Physics Letters*, 112(11):111105, 2018.

[29] Volker Heine. The pseudopotential concept. In Henry Ehrenreich, Frederick Seitz, and David Turnbull, editors, *Solid State Physics*, volume 24 of *Solid State Physics*, pages 1 – 36. Academic Press, 1970.

[30] J Ihm. Total energy calculations in solid state physics. *Reports on Progress in Physics*, 51(1):105, 1988.

[31] Warren E. Pickett. Pseudopotential methods in condensed matter applications. *Computer Physics Reports*, 9(3):115 – 197, 1989.

[32] R. Peierls. Zur theorie des diamagnetismus von leitungselektronen. *Zeitschrift für Physik*, 80(11):763–791, Nov 1933.

[33] next**nano** GmbH. nextnano – software for semiconductor nanodevices. `http://www.nextnano.com/`.

[34] S. Hackenbuchner. *Elektronische Struktur von Halbleiter-Nanobauelementen im thermodynamischen Nichtgleichgewicht*. PhD thesis, Technische Universität München, 2002.

[35] T. Andlauer. *Optoelectronic and spin-related properties of semiconductor nanostructures in magnetic fields*. PhD thesis, Technische Universität München, 2009.

[36] S. Birner. *Modeling of semiconductor nanostructures and semiconductor-electrolyte interfaces*. PhD thesis, Technische Universität München, 2011.

[37] T. Eißfeller. *Theory of the Electronic Structure of Quantum Dots in External Fields*. PhD thesis, Technische Universität München, 2012.

[38] P. Y. Yu and M. Cardona. *Fundamentals of Semiconductors - Physics and Materials Properties*. Springer, 4th edition, 2010.

[39] J. M. Luttinger and W. Kohn. Motion of electrons and holes in perturbed periodic fields. *Phys. Rev.*, 97:869–883, Feb 1955.

[40] PerOlov Löwdin. A note on the quantummechanical perturbation theory. *The Journal of Chemical Physics*, 19(11):1396–1401, 1951.

[41] I. Vurgaftman, J. R. Meyer, and L. R. Ram-Mohan. Band parameters for iiiv compound semiconductors and their alloys. *Journal of Applied Physics*, 89(11):5815–5875, 2001.

[42] M G Burt. The justification for applying the effective-mass approximation to microstructures. *Journal of Physics: Condensed Matter*, 4(32):6651, 1992.

[43] G. Dresselhaus, A. F. Kip, and C. Kittel. Cyclotron resonance of electrons and holes in silicon and germanium crystals. *Phys. Rev.*, 98:368–384, Apr 1955.

[44] Evan O. Kane. Band structure of indium antimonide. *Journal of Physics and Chemistry of Solids*, 1(4):249 – 261, 1957.

[45] Chris G. Van de Walle. Band lineups and deformation potentials in the model-solid theory. *Phys. Rev. B*, 39:1871–1883, Jan 1989.

[46] Thomas B. Bahder. Eight-band k·p model of strained zinc-blende crystals. *Phys. Rev. B*, 41:11992–12001, Jun 1990.

[47] H. Haug and S. W. Koch. *Quantum Theory of the Optical and Electronic Properties of Seimiconductors*. World Scientific, 5th edition, 2005fixme.

[48] S. Glutsch. Excitons in low-dimensional semiconductors. In *Springer Series in Solid-State Sciences*, number 141 in Solid-State Sciences. Springer, 2004.

[49] T. Eißfeller. Linear optical response of semiconductor nanodevices. Diploma thesis, Technische Universität München, 2008.

[50] J. Z. Garcia. Analytic coulomb matrix elements in a three-dimensional geometry. *Journal of Mathematical Physics*, 46(12):122104, 2005.

[51] A. Zimmermann, S. Kuhn, and M. Richter. Poisson green's function method for increased computational efficiency in numerical calculations of coulomb coupling elements. *Phys. Rev. B*, 93:035308, Jan 2016.

[52] D. Demidov. Amgcl - c++ library for solving sparse linear systems with algebraic multigrid method. `https://github.com/ddemidov/amgcl`.

[53] Y. Saito, K. Takahashi, and S. Hayano. Finite element solution of open boundary magnetic field problems. *IEEE Transactions on Magnetics*, 23(5):3569–3571, Sep 1987.

[54] B. M. A. Rahman and J. B. Davies. Finite-element analysis of optical and microwave waveguide problems. *IEEE Transactions on Microwave Theory and Techniques*, 32(1):20–28, Jan 1984.

[55] G. Beer and J. L. Meek. infinite domain elements. *International Journal for Numerical Methods in Engineering*, 17(1):43–52, 1981.

[56] A. Bayliss, M. Gunzburger, and E. Turkel. Boundary conditions for the numerical solution of elliptic equations in exterior regions. *SIAM Journal on Applied Mathematics*, 42(2):430–451, 1982.

[57] O. Goni. A new approach to implement absorbing boundary condition in biomolecular electrostatics. *IEEE/ACM Transactions on Computational Biology and Bioinformatics*, 10(3):799–804, May 2013.

[58] D. C. Meeker. Improvised asymptotic boundary conditions for electrostatic finite elements. *IEEE Transactions on Magnetics*, 50(6):1–9, June 2014.

[59] Q. Chen and A. Konrad. A review of finite element open boundary techniques for static and quasi-static electromagnetic field problems. *IEEE Transactions on Magnetics*, 33(1):663–676, Jan 1997.

[60] K. K. Mei, R. Pous, Zhaoqing Chen, Yao-Wu Liu, and M. D. Prouty. Measured equation of invariance: a new concept in field computations. *IEEE Transactions on Antennas and Propagation*, 42(3):320–328, Mar 1994.

[61] K. Stüben. *Algebraic Multigrid (AMG): An Introduction with Applications.* GMD-Report. GMD-Forschungszentrum Informationstechnik, 1999.

[62] A. Brandt. Multi-level adaptive solutions to boundary-value problems. *Mathematics of Computation*, 31, 1977.

[63] Tanabe Y. Onodera Y. Inui, T. *Group Theory and Its Applications in Physics*, volume 78 of *Solid-State Sciences.* Springer, 1996.

[64] J. P. Elliot and P. G. Dawber. *Symmetry in Physics*, volume 1. The Macmillan Press Ltd, 1979.

[65] G. Bester and A. Zunger. Cylindrically shaped zinc-blende semiconductor quantum dots do not have cylindrical symmetry: Atomistic symmetry, atomic relaxation, and piezoelectric effects. *Physical Review B*, 71:045318, 2005.

[66] N. Baer. *Optical and Electronic Properties of InGaAs and Nitride Quantum Dots.* PhD thesis, Universität Bremen, 2006.

[67] R. Heitz, F. Guffarth, I. Mukhametzhanov, M. Grundmann, A. Madhukar, and D. Bimberg. Many-body effects on the optical spectra of inas/gaas quantum dots. *Physical Review B*, 62(24), 2000.

[68] N. Liu, J. Tersoff, O. Baklenov, A. L. Holmes, and C. K. Shih. Nonuniform composition profile in $\mathrm{in}_{0.5}\mathrm{ga}_{0.5}\mathrm{As}$ alloy quantum dots. *Phys. Rev. Lett.*, 84:334–337, Jan 2000.

[69] T. Walther, A. G. Cullis, D. J. Norris, and M. Hopkinson. Nature of the stranski-krastanow transition during epitaxy of ingaas on gaas. *Phys. Rev. Lett.*, 86:2381–2384, Mar 2001.

[70] I. Kegel, T. H. Metzger, A. Lorke, J. Peisl, J. Stangl, G. Bauer, J. M. García, and P. M. Petroff. Nanometer-scale resolution of strain and interdiffusion in self-assembled InAs/GaAs quantum dots. *Phys. Rev. Lett.*, 85:1694–1697, Aug 2000.

[71] J. Zou, X. Z. Liao, D. J. H. Cockayne, and R. Leon. Transmission electron microscopy study of $\mathrm{in}_x\mathrm{ga}_{1-x}\mathrm{As}$ quantum dots on a gaas(001) substrate. *Phys. Rev. B*, 59:12279–12282, May 1999.

[72] J. D. Mar, X. L. Xu, J. J. Baumberg, F. S. F. Brossard, A. C. Irvine, C. Stanley, and D. A. Williams. Bias-controlled single-electron charging of a self-assembled

quantum dot in a two-dimensional-electron-gas-based $n-i$-schottky diode. *Phys. Rev. B*, 83:075306, Feb 2011.

[73] M. Scheibner, I. V. Ponomarev, E. A. Stinaff, M. F. Doty, A. S. Bracker, C. S. Hellberg, T. L. Reinecke, and D. Gammon. Photoluminescence spectroscopy of the molecular biexciton in vertically stacked inas-gaas quantum dot pairs. *Phys. Rev. Lett.*, 99:197402, Nov 2007.

[74] Michael Scheibner, Allan S. Bracker, Danny Kim, and Daniel Gammon. Essential concepts in the optical properties of quantum dot molecules. *Solid State Communications*, 149(35):1427 – 1435, 2009. Fundamental Phenomena and Applications of Quantum Dots.

[75] F. Findeis, M. Baier, E. Beham, A. Zrenner, and G. Abstreiter. Photocurrent and photoluminescence of a single self-assembled quantum dot in electric fields. *Applied Physics Letters*, 78(19):2958–2960, 2001.

[76] S. C. Rand. *Lectures on Light.* Oxford University Press, 2nd edition, 2016.

[77] T. Meier, P. Thomas, and S. W. Koch. *Coherent Semiconductor Optics.* Springer, 2007.

[78] J. Fricke. Transport equations including many-particle correlations for an arbitrary quantum system: A general formalism. *Annals of Physics*, 252(2):479 – 498, 1996.

[79] V. M. Axt and A. Stahl. A dynamics-controlled truncation scheme for the hierarchy of density matrices in semiconductor optics. *Zeitschrift für Physik B Condensed Matter*, 93(2):195–204, 1994.

[80] Aaron Meurer, Christopher P. Smith, Mateusz Paprocki, Ondřej Čertík, Sergey B. Kirpichev, Matthew Rocklin, AMiT Kumar, Sergiu Ivanov, Jason K. Moore, Sartaj Singh, Thilina Rathnayake, Sean Vig, Brian E. Granger, Richard P. Muller, Francesco Bonazzi, Harsh Gupta, Shivam Vats, Fredrik Johansson, Fabian Pedregosa, Matthew J. Curry, Andy R. Terrel, Štěpán Roučka, Ashutosh Saboo, Isuru Fernando, Sumith Kulal, Robert Cimrman, and Anthony Scopatz. Sympy: symbolic computing in python. *PeerJ Computer Science*, 3:e103, January 2017.

[81] G. Lindblad. On the generators of quantum dynamical semigroups. *Communications in Mathematical Physics*, 43:119–130, 1976.

[82] G. Schaller. *Open Quantum Systems Far from Equilibrium.* Number 881 in Lecture Notes in Physics. Springer, year.

[83] J. Förstner, C. Weber, J. Danckwerts, and A. Knorr. Phonon-assisted damping of rabi oscillations in semiconductor quantum dots. *Phys. Rev. Lett.*, 91:127401, Sep 2003.

[84] J. Förstner. *Light Propagation and Many-Particle Effects in Semiconductor Nanostructures.* PhD thesis, Technische Universität Berlin, 2005.

[85] J. L. Skinner and D. Hsu. Pure dephasing of a two-level system. *The Journal of Physical Chemistry*, 90(21):4931–4938, 1986.

[86] T Meier, P Thomas, and S. W. Koch. *Coherent Semiconductor Optics.* Springer, 2007.

[87] S. Michaelis de Vasconcellos. *Coherent Optoelectronic Control of Single Excitons.* PhD thesis, Paderborn University, 2009.

[88] N. V. Vitanov, T. Halfmann, B. W. Shore, and Klaas Bergmann. Laser-induced population transfer by adiabatic passage techniques. *Annual Review of Physical Chemistry*, 52(1):763–809, 2001. PMID: 11326080.

[89] A. D. Greentree, J. H. Cole, A. R. Hamilton, and L. C. L. Hollenberg. Coherent electronic transfer in quantum dot systems using adiabatic passage. *Phys. Rev. B*, 70:235317, Dec 2004.

[90] M. Oberst, H. Münch, and T. Halfmann. Efficient coherent population transfer among three states in no molecules by stark-chirped rapid adiabatic passage. *Phys. Rev. Lett.*, 99:173001, Oct 2007.

[91] J. Osman, Y. Ishibashi, and D. R. Tilley. Calculation of nonlinear susceptibility tensor components in ferroelectrics. *Japanese Journal of Applied Physics*, 37(9R):4887, 1998.

[92] Intel Corporation. Avoiding and identifying false sharing among threads. `https://software.intel.com/en-us/articles/avoiding-and-identifying-false-sharing-among-threads`.

Symbols

$\boldsymbol{x}$	Vector
$\psi(\boldsymbol{x})$	Scalar field
$\boldsymbol{A}(\boldsymbol{x})$	Vector field
$\hat{A}$	Scalar operator
$\hat{A}^\dagger$	Hermitian conjugate operator
$\hat{\boldsymbol{A}}$	Vector operator
FFT	Fast Fourier transform
EFA	Envelope Function Approximation
PGF	Poisson Green's function
FLS	few level system
TLS	two level system
RAP	rapid adiabatic passage
RWA	rotating wave approximation
FWHI	full width at half intensity
FWHM	full width at half maximum